



2015-09

# Characterization of micron-scale nanotubular super dielectric materials

Gandy, Jonathan Wayne

Monterey, California: Naval Postgraduate School

---

<http://hdl.handle.net/10945/47260>



Calhoun is a project of the Dudley Knox Library at NPS, furthering the precepts and goals of open government and government transparency. All information contained herein has been approved for release by the NPS Public Affairs Officer.

**Dudley Knox Library / Naval Postgraduate School**  
**411 Dyer Road / 1 University Circle**  
**Monterey, California USA 93943**

<http://www.nps.edu/library>



# **NAVAL POSTGRADUATE SCHOOL**

**MONTEREY, CALIFORNIA**

## **THESIS**

**CHARACTERIZATION OF MICRON-SCALE  
NANOTUBULAR SUPER DIELECTRIC MATERIALS**

by

Jonathan Wayne Gandy

September 2015

Thesis Advisor:  
Co-Advisor:

Jonathan Phillips  
Sarith Menon

**Approved for public release; distribution is unlimited**

THIS PAGE INTENTIONALLY LEFT BLANK

<b>REPORT DOCUMENTATION PAGE</b>			<i>Form Approved OMB No. 0704-0188</i>	
Public reporting burden for this collection of information is estimated to average 1 hour per response, including the time for reviewing instruction, searching existing data sources, gathering and maintaining the data needed, and completing and reviewing the collection of information. Send comments regarding this burden estimate or any other aspect of this collection of information, including suggestions for reducing this burden, to Washington headquarters Services, Directorate for Information Operations and Reports, 1215 Jefferson Davis Highway, Suite 1204, Arlington, VA 22202-4302, and to the Office of Management and Budget, Paperwork Reduction Project (0704-0188) Washington DC 20503.				
<b>1. AGENCY USE ONLY (Leave blank)</b>		<b>2. REPORT DATE</b> September 2015	<b>3. REPORT TYPE AND DATES COVERED</b> Master's Thesis	
<b>4. TITLE AND SUBTITLE</b> CHARACTERIZATION OF MICRON-SCALE NANOTUBULAR SUPER DIELECTRIC MATERIALS			<b>5. FUNDING NUMBERS</b> RPJY3 W4P06	
<b>6. AUTHOR(S)</b> Gandy, Jonathan Wayne			<b>8. PERFORMING ORGANIZATION REPORT NUMBER</b>	
<b>7. PERFORMING ORGANIZATION NAME(S) AND ADDRESS(ES)</b> Naval Postgraduate School Monterey, CA 93943-5000				
<b>9. SPONSORING /MONITORING AGENCY NAME(S) AND ADDRESS(ES)</b> N/A			<b>10. SPONSORING/MONITORING AGENCY REPORT NUMBER</b>	
<b>11. SUPPLEMENTARY NOTES</b> The views expressed in this thesis are those of the author and do not reflect the official policy or position of the Department of Defense or the U.S. Government. IRB Protocol number ____N/A____.				
<b>12a. DISTRIBUTION / AVAILABILITY STATEMENT</b> Approved for public release; distribution is unlimited			<b>12b. DISTRIBUTION CODE</b>	
<b>13. ABSTRACT (maximum 200 words)</b>  <p>This research is part of an ongoing program of study focused on dielectric materials based on a novel hypothesis: that porous electrically insulating solids in which the pores are filled with liquids containing an ionic species (such as water with dissolved salt) will have very high dielectric values by virtue of the separation of ions in the liquid phase and concurrent formation of large dipoles. Earlier work focused on the creation of super dielectric materials by saturating porous electrically insulating powders, such as alumina, with salt solutions.</p> <p>The focus of the present work is the characterization and evaluation of capacitors based on a novel dielectric: titanium dioxide nanotube arrays created by anodization and filled with a concentrated aqueous salt solution. Capacitors made up of this so-called nanotubular super dielectric material were found to have extreme dielectric constants, greater than one billion. The same capacitors also registered unprecedented energy densities, consistently greater than 400 joules per cubic centimeter, which is more than ten times the best commercial supercapacitors. Sufficient data was collected to propose a correlation relating dielectric thickness, salt concentration, and electrode surface area to overall energy density.</p>				
<b>14. SUBJECT TERMS</b> capacitor, supercapacitor, super dielectric material, titanium dioxide, nanotubes			<b>15. NUMBER OF PAGES</b> 193	
			<b>16. PRICE CODE</b>	
<b>17. SECURITY CLASSIFICATION OF REPORT</b> Unclassified	<b>18. SECURITY CLASSIFICATION OF THIS PAGE</b> Unclassified	<b>19. SECURITY CLASSIFICATION OF ABSTRACT</b> Unclassified	<b>20. LIMITATION OF ABSTRACT</b> UU	



THIS PAGE INTENTIONALLY LEFT BLANK

**Approved for public release; distribution is unlimited**

**CHARACTERIZATION OF MICRON-SCALE NANOTUBULAR SUPER  
DIELECTRIC MATERIALS**

Jonathan Wayne Gandy  
Lieutenant Commander, United States Navy  
B.S., United States Naval Academy, 2002

Submitted in partial fulfillment of the  
requirements for the degree of

**MECHANICAL ENGINEER  
AND  
MASTER OF SCIENCE IN MECHANICAL ENGINEERING**

from the

**NAVAL POSTGRADUATE SCHOOL  
September 2015**

Approved by: Jonathan Phillips, PhD  
Thesis Advisor

Sarath Menon, PhD  
Co-Advisor

Garth Hobson, PhD  
Chair, Department of Mechanical and Aerospace Engineering

THIS PAGE INTENTIONALLY LEFT BLANK

## **ABSTRACT**

This research is part of an ongoing program of study focused on dielectric materials based on a novel hypothesis: that porous electrically insulating solids in which the pores are filled with liquids containing an ionic species (such as water with dissolved salt) will have very high dielectric values by virtue of the separation of ions in the liquid phase and concurrent formation of large dipoles. Earlier work focused on the creation of super dielectric materials by saturating porous electrically insulating powders, such as alumina, with salt solutions.

The focus of the present work is the characterization and evaluation of capacitors based on a novel dielectric: titanium dioxide nanotube arrays created by anodization and filled with a concentrated aqueous salt solution. Capacitors made up of this so-called nanotubular super dielectric material were found to have extreme dielectric constants, greater than one billion. The same capacitors also registered unprecedented energy densities, consistently greater than 400 joules per cubic centimeter, which is more than ten times the best commercial supercapacitors. Sufficient data was collected to propose a correlation relating dielectric thickness, salt concentration, and electrode surface area to overall energy density.

THIS PAGE INTENTIONALLY LEFT BLANK

# TABLE OF CONTENTS

<b>I.</b>	<b>INTRODUCTION.....</b>	<b>1</b>
<b>A.</b>	<b>SUMMARY OF FINDINGS .....</b>	<b>1</b>
<b>B.</b>	<b>MOTIVATION .....</b>	<b>2</b>
<b>C.</b>	<b>BACKGROUND THEORY .....</b>	<b>9</b>
<b>D.</b>	<b>CAPACITOR TECHNOLOGIES.....</b>	<b>11</b>
1.	Electrostatic and Electrolytic Capacitors .....	12
2.	Double Layer Capacitors .....	14
3.	Pseudocapacitance .....	16
<b>E.</b>	<b>FOCUS OF PRESENT STUDY .....</b>	<b>18</b>
<b>II.</b>	<b>ANODIZATION OF TUNGSTEN.....</b>	<b>21</b>
<b>A.</b>	<b>INTRODUCTION.....</b>	<b>21</b>
<b>B.</b>	<b>BACKGROUND ON TECHNIQUE.....</b>	<b>22</b>
<b>C.</b>	<b>EXPERIMENTAL SETUP AND METHODS.....</b>	<b>24</b>
1.	Anodization Materials and Equipment.....	24
2.	Experimental Method.....	25
<b>D.</b>	<b>ANALYSIS .....</b>	<b>26</b>
1.	Anodizing Voltage and Duration .....	27
2.	Characterization .....	29
3.	Anodization at 40 Volts .....	31
4.	Anodization at 20 Volts .....	32
a.	<i>Duration 5 Minutes.....</i>	<i>34</i>
b.	<i>Duration 10 Minutes.....</i>	<i>34</i>
c.	<i>Duration 15 Minutes.....</i>	<i>35</i>
d.	<i>Duration 30 Minutes.....</i>	<i>35</i>
e.	<i>Duration 45 Minutes.....</i>	<i>36</i>
<b>E.</b>	<b>CONCLUSION .....</b>	<b>38</b>
<b>III.</b>	<b>ANODIZATION OF TITANIUM.....</b>	<b>39</b>
<b>A.</b>	<b>INTRODUCTION.....</b>	<b>39</b>
<b>B.</b>	<b>BACKGROUND ON THE TECHNIQUE .....</b>	<b>40</b>
<b>C.</b>	<b>EXPERIMENTAL SETUP .....</b>	<b>44</b>
1.	Materials and Equipment .....	44
2.	Characterization Techniques.....	45
a.	<i>Scanning Electron Microscopy (SEM) Analysis .....</i>	<i>45</i>
b.	<i>Transmission Electron Microscopy (TEM) Analysis .....</i>	<i>46</i>
c.	<i>X-ray Diffraction (XRD) Analysis.....</i>	<i>46</i>
d.	<i>Anodic Current Density .....</i>	<i>47</i>
<b>D.</b>	<b>EXPERIMENTAL METHOD AND ANALYSIS.....</b>	<b>48</b>
1.	Thin Films (thickness $\leq 6\mu\text{m}$ ) .....	51
a.	<i>Protocol: 40 Volt, 2 Hours, Low Fluoride .....</i>	<i>51</i>
b.	<i>Protocol: 40 Volt, 1 Hour, Low Fluoride.....</i>	<i>54</i>
2.	Medium Films ( $6\mu\text{m} < \text{thickness} < 17\mu\text{m}$ ) .....	57

a.	<i>Protocol: 40 Volt, 4 Hour, Low Fluoride, Electrode Polishing.....</i>	<i>58</i>
b.	<i>Protocol: 40 Volt, 4 Hour, Low Fluoride, Electrolyte Reuse.....</i>	<i>60</i>
3.	<b>Thick Films (thickness <math>\geq 17\mu\text{m}</math>).....</b>	<b>64</b>
a.	<i>Protocol: 60 Volt, 4 Hour, High Fluoride.....</i>	<i>64</i>
b.	<i>Protocol: 50 Volt, 4 Hour, High Fluoride, Electrolyte Reused.....</i>	<i>67</i>
c.	<i>Protocol: 50 Volt, 4 Hour, High Fluoride, New Electrolyte.....</i>	<i>69</i>
d.	<i>Protocol: 40 Volt and 45 Volt, 4 Hours, High Fluoride.....</i>	<i>76</i>
e.	<i>Protocol: 50 Volt, High Fluorides, Dried Horizontally.....</i>	<i>78</i>
f.	<i>Protocol: 50 Volt, High Fluorides, Dried Vertically.....</i>	<i>81</i>
E.	<b>DELAMINATED FILM ANALYSES .....</b>	<b>86</b>
1.	<b>Compositional Analyses .....</b>	<b>87</b>
F.	<b>SUMMARY .....</b>	<b>88</b>
IV.	<b>NTSDM CAPACITOR EXPERIMENTAL METHODS.....</b>	<b>93</b>
A.	<b>INTRODUCTION.....</b>	<b>93</b>
B.	<b>CIRCUIT SETUP AND MEASUREMENT METHODS .....</b>	<b>94</b>
1.	<b>Capacitance Measurement.....</b>	<b>96</b>
2.	<b>Dielectric Constant Calculation.....</b>	<b>98</b>
3.	<b>Energy Density Calculation .....</b>	<b>99</b>
4.	<b>Leakage Resistance Measurement.....</b>	<b>100</b>
C.	<b>MATERIALS AND NTSDM ASSEMBLY .....</b>	<b>102</b>
D.	<b>VERIFICATION OF CAPACITOR CIRCUIT .....</b>	<b>107</b>
V.	<b>NTSDM RESULTS AND ANALYSIS.....</b>	<b>111</b>
A.	<b>ASSUMPTIONS AND INITIAL CONDITIONS .....</b>	<b>111</b>
1.	<b>Maximum Operating Voltage vs. Applied Voltage.....</b>	<b>111</b>
2.	<b>Energy Density vs. Applied Voltage.....</b>	<b>116</b>
B.	<b>DISCUSSION OF NTSDM CAPACITOR BEHAVIOR.....</b>	<b>120</b>
1.	<b>Three Region Capacitance .....</b>	<b>121</b>
2.	<b>Pseudocapacitance Behavior.....</b>	<b>123</b>
3.	<b>Noisy Charge or Discharge .....</b>	<b>127</b>
C.	<b>NTSDM CAPACITOR ANALYSIS.....</b>	<b>130</b>
1.	<b>Capacitance and Dielectric Constant Analysis.....</b>	<b>130</b>
2.	<b>Energy and Energy Density Analysis.....</b>	<b>132</b>
3.	<b>Leakage Resistance Analysis.....</b>	<b>136</b>
D.	<b>OTHER NTSDM DESIGNS CONSIDERED .....</b>	<b>138</b>
1.	<b>Electrolyte Selection.....</b>	<b>138</b>
2.	<b>Positive Electrode Selection .....</b>	<b>139</b>
E.	<b>SUMMARY .....</b>	<b>141</b>
1.	<b>Capacitance and Energy Density.....</b>	<b>141</b>
2.	<b>Operating Voltage Limitations .....</b>	<b>143</b>
VI.	<b>SUMMARY OF FINDINGS .....</b>	<b>145</b>

A.	TUNGSTEN ANODIZATION RESULTS .....	145
B.	TITANIUM ANODIZATION RESULTS .....	146
C.	NTSDM CAPACITOR RESULTS.....	146
VII.	RECOMMENDED FUTURE WORK.....	149
APPENDIX A	.....	153
APPENDIX B	.....	155
APPENDIX C	.....	157
LIST OF REFERENCES	.....	159
INITIAL DISTRIBUTION LIST	.....	169



THIS PAGE INTENTIONALLY LEFT BLANK

## LIST OF FIGURES

Figure 1.	Specific power versus specific energy for different electrical energy storage technologies.....	6
Figure 2.	Basic schematic of a parallel plate capacitor. ....	10
Figure 3.	Schematic presentation of electrostatic (a), electrolytic (b), and electric double layer capacitors (c). ....	12
Figure 4.	Depiction of dipole alignment within a polarizable media. ....	13
Figure 5.	Equivalent circuit for a capacitor electrode interface demonstrating Faradaic and non-Faradaic capacitances.....	18
Figure 6.	Schematic of NTSDM capacitor with Grafoil positive electrode (1), aqueous electrolyte (2), tubular oxide structure (3), and metal substrate as negative electrode (4).....	19
Figure 7.	Schematic of the electrochemical circuit used to anodize tungsten substrates.....	25
Figure 8.	Anodization current densities over 1 hour. ....	27
Figure 9.	Anodization current densities in the first 2.5 minutes. ....	28
Figure 10.	Naked eye comparisons of WO <sub>3</sub> film for 20 volt 15-minute anodization (a) and for 40 volt 90-minute anodization (b). ....	30
Figure 11.	Optical micrographs of the 20 volt 15-minute WO <sub>3</sub> film (a) and the 40 volt 90-minute WO <sub>3</sub> film (b) at low magnification.....	31
Figure 12.	SEM images of the 40 volt 60-minute sample (a) and of the 40 volt 90-minute sample (b) at high magnification. ....	32
Figure 13.	SEM Images of 20-volt anodized WO <sub>3</sub> films at 5 minutes (a), 10 minutes (b), 15 minutes (c), 30 minutes (d), and 45 minutes (e) at high magnification. ....	33
Figure 14.	SEM images of 20 volt, 10-minute anodic WO <sub>3</sub> damage due to film rupture (a) but useful for measuring thickness (b).....	35
Figure 15.	Secondary electron images showing a comparison of 20 volt (top) and 40 volt (bottom) anodic films after 1 hour at low (left), medium (middle), and high (right) magnification. ....	36
Figure 16.	Pore size distribution for 1 hour anodized specimens at 20 and 40 volts. ....	37
Figure 17.	Typical anodic current trend over time (a); drawing of field-aided ionic transport without fluorides (b); and drawing of field-aided ionic transport with fluorides (c).....	43
Figure 18.	(a) Anodization workstation with DC voltage power supplies, digital voltmeter, digital ammeter with computer interface, and electrochemical cell; (b) one of three power supplies used as a DC voltage source to anodize titanium; and (c) Keithley 2400 Source Meter used to monitor applied anodization potential. ....	44
Figure 19.	ZEISS Scanning Electron Microscope.....	45
Figure 20.	FEI Transmission Electron Microscope.....	46
Figure 21.	Rigaku MiniFlex 600 benchtop X-ray diffractometer. ....	47

Figure 22.	UNIT-T UT71B True RMS Multimeter with computer interface was used to monitor and record anodizing current.....	47
Figure 23.	Side view (a) and top view (b) of the electrochemical anodization cell with anode and cathode immersed in prepared electrolyte. ....	50
Figure 24.	SEM image capturing a cross-sectional view of the nanotube matrix with closed bottom ends apparent on the left.....	52
Figure 25.	SEM images of the well-formed, self-organized 6 $\mu\text{m}$ nanotubes produced using 40 volts for 2 hours.....	52
Figure 26.	SEM images of the open tops of the nanotubes at the film surface (a) and the closed nanotube bottoms at the film and substrate interface. ....	53
Figure 27.	SEM images that capture variation in the nanotube inner diameter from just below the open top (a) down to the closed base (b).....	54
Figure 28.	Comparison of anodic current densities for 40 volt, 1-hour protocols during electrolyte initial use (1 <sup>st</sup> anodization) and reuse (2 <sup>nd</sup> anodization). ...	55
Figure 29.	SEM images of 40 volt, 1-hour anodic film comprised of self-organized 3 $\mu\text{m}$ nanotubes (a), well-formed tube tops (b), closed bottom ends (c), and general film morphology at a lower magnification (d).....	56
Figure 30.	SEM images of 40 volt, 1-hour (electrolyte reused) anodic film comprised of 3.8 $\mu\text{m}$ nanotubes (a–c) and closed tube bottoms and open tube tops at the surface (d). ....	57
Figure 31.	Comparison of anodic current densities for 40 volt, 4-hour protocols polished and unpolished.....	58
Figure 32.	SEM images of the 40 volt, 4-hour anodic films comparing the 8 $\mu\text{m}$ nanotubes of the polished sample (a) alongside the 11 $\mu\text{m}$ nanotubes of the unpolished sample (b). ....	59
Figure 33.	SEM images of anodic film produced at 40 volts, 4 hours on a polished substrate that capture nanotube openings at the surface (a), tube wall thickness below the surface (b), and wall thickness closer to the closed bottom ends (c, d). ....	60
Figure 34.	SEM images of anodic film produced at 40 volts, 4 hours on an unpolished substrate that capture nanotube wall thickness below the surface (a), same image at higher magnification (b), intermediate tube wall thickness (c), and general surface morphology (d). ....	60
Figure 35.	Comparison of anodic current densities between new electrolyte and reused electrolyte for the same 40 volt, 4-hour protocol. ....	61
Figure 36.	SEM images of anodic film produced at 40 volts, 4 hours (first use) with 8 $\mu\text{m}$ nanotubes (a, b), closed bottom ends (c), and familiar surface morphology (d). ....	62
Figure 37.	SEM images of anodic film produced at 40 volts, 4 hours (second use) with 8 $\mu\text{m}$ nanotubes (a), open nanotube tops (b), characteristic tube wall thickness at mid-length (c), and closed bottom ends (d). ....	62
Figure 38.	SEM images of anodic film produced at 40 volts, 4 hours (second use) from the disengaged side of the anode depicting open nanotube tops (a–c) and mid-length wall thickness (d).....	63

Figure 39.	Recorded anodic current density for first thick film anodization technique using 60-volt protocol (60 volts for 15 minutes, 40 volts for another 3.75 hours). ....	65
Figure 40.	Anodized titanium after 60 volt, 4-hour protocol with arrows distinguishing SEM sample cuts from the substrate dissolution (right edge).....	66
Figure 41.	SEM images of 60-volt anodic film depicting familiar nanotube morphology with 13 $\mu\text{m}$ to 18 $\mu\text{m}$ long nanotubes (a–c), a carpet-like surface morphology identified as “grassing” (d) and closed nanotube bottom ends (e, f). ....	67
Figure 42.	Recorded anodic current density for 50 volt, 4-hour technique reusing high fluoride electrolyte from previous 60-volt anodization. ....	68
Figure 43.	SEM images of 50 volt, 4-hour anodic film depicting familiar nanotube morphology with existence of 18 $\mu\text{m}$ tubes.....	69
Figure 44.	Anodic current density recorded during the 50 volts, 4 hour, high fluoride anodization procedure; while in progress, the actual protocol was adjusted to 50 volts for 2 hours followed by 40 volts for 2 hours.....	70
Figure 45.	Complete anodization of a titanium substrate at 50 volts, 4 hours looks like a hole in the center of the anode, but is rather two back-to-back nanotube arrays visible from the engaged side (a) and disengaged side (b)....	71
Figure 46.	SEM images of 50 volt, 4-hour anodic film depicting familiar morphology with nanotubes measuring from 39 $\mu\text{m}$ down to 26 $\mu\text{m}$ (a,b), grassing (c), and closed bottom ends (d). ....	72
Figure 47.	TEM image capturing a midsection of a nanotube from a 29 $\mu\text{m}$ matrix with outer diameter varying between 147 nm and 158 nm.....	74
Figure 48.	TEM images capturing the varying tube wall thicknesses: 16 nm near the top (a), 20 nm at mid length (b), and 33 nm near the bottom (c).....	74
Figure 49.	TEM images capturing a nanotube bottom end section from a 27 $\mu\text{m}$ anodic film (a) and the closed bottom end (b); end cap measured at 75 nm thick with 55 nm tube walls at the bottom. ....	75
Figure 50.	TEM images capturing a nanotube pair (a) and a cluster of at least 5 nanotubes stacked side-by-side and atop one another (b).....	75
Figure 51.	Anodic current densities recorded during the 40 volt 4-hour, and 45 volt 4-hour high fluoride anodization procedures. ....	76
Figure 52.	SEM images of 40 volt, 4-hour anodic film capturing 6 $\mu\text{m}$ nanotubes (a,b), grassing (c) and closed bottom ends (d). ....	77
Figure 53.	SEM images of 45 volt, 4 hour anodic film capturing 7 $\mu\text{m}$ nanotubes. ....	77
Figure 54.	Anodic current densities recorded during the 50 volt, 4-hour (new electrolyte) and second anodization using the same electrolyte. ....	78
Figure 55.	SEM images of 50 volt, 4-hour anodic film capturing 27 $\mu\text{m}$ (a), familiar tubular morphology at tube bases (b), clean tube structure just below grassing (c), and grassing at the surface (d).....	79
Figure 56.	SEM images of 50 volt, 4-hour (reused electrolyte) anodic film capturing 18 $\mu\text{m}$ nanotubes (a) and grassing at low magnification (b).....	80

Figure 57.	Delamination of anodic film observed with the 27 $\mu\text{m}$ film after drying for approximately 1 hour; the arrow (b) denotes the height of the rigidly suspended anodic film.....	80
Figure 58.	Delamination of anodic film observed with the 18 $\mu\text{m}$ film after drying overnight in an enclosed container. ....	81
Figure 59.	Anodic current densities recorded during another 50 volt, 4-hour (new electrolyte) and second anodization using the same electrolyte. ....	82
Figure 60.	SEM images of 50 volt, 4-hour (reused electrolyte) anodic film capturing 26 $\mu\text{m}$ nanotubes (a), tube bottoms with non-anodized substrate remnants (b), remnant of titanium substrate (c) and grassing (d).....	83
Figure 61.	SEM images of 50 volt, 4-hour (reused electrolyte) anodic film capturing 17 $\mu\text{m}$ nanotubes. ....	84
Figure 62.	SEM images of 50 volt, 4-hour (reused electrolyte) anodic film with grassing (a) and apparent remnant of compact oxide layer (b).....	84
Figure 63.	Titanium substrate completely anodized at 50 volts, 4 hours (a); subsequent 26 $\mu\text{m}$ film delamination while suspended vertically to dry (b). ....	85
Figure 64.	A portion of the 17 $\mu\text{m}$ oxide film remained attached (a) and therefore viable for subsequent capacitor analysis (b). ....	85
Figure 65.	Thick anodic film (27 $\mu\text{m}$ ) delaminated during drying procedure from both sides of substrate (a) with visible remnants of non-anodized titanium (b). ....	86
Figure 66.	Mostly amorphous XRD patter for the anodic $\text{TiO}_2$ film. ....	88
Figure 67.	XRD diffraction pattern (after subtraction of the amorphous pattern corresponding to orthorhombic $\text{TiO}_2$ (PDF Card No. 01-080-5176 in Appendix A). ....	88
Figure 68.	Depiction of thinning tube tops and formation of grassing (1), over well-formed nanotubes (2), and titanium foil substrate (3).....	90
Figure 69.	National Instruments ELVIS II workstation with ceramic bedplate knife switch for charging and discharging. ....	95
Figure 70.	NTSDM test circuit schematic with switch in charge position.....	96
Figure 71.	NTSDM test circuit schematic with switch in discharge position. ....	96
Figure 72.	Example of an NTSDM charge/discharge plot with 6 volts applied during charge; this particular plot contains 4 charge/discharge cycles. ....	97
Figure 73.	Example of an NTSDM discharge log plot over time with three distinct regions of linear behavior. ....	98
Figure 74.	Schematic of the equivalent discharging circuit with theoretical NTSDM capacitor components; switch is depicted in the open circuit position. ....	101
Figure 75.	Voltage spike recorded at instant of open circuit on a charged NTSDM capacitor. ....	102
Figure 76.	Capacitor assembly components. ....	104
Figure 77.	Fully assembled NTSDM capacitor ready for testing.....	104
Figure 78.	NTSDM capacitor containment chamber. ....	105
Figure 79.	NTSDM capacitor test assembly with humidity control cover.....	106

Figure 80.	A single charge/discharge cycle using a 220 mF supercapacitor with 5.0 volts applied to verify circuit and switching operation.....	107
Figure 81.	Discharge log plot versus time demonstrating RC time constant by linear interpolation; inlay plot has shortened time scale demonstrating Region I discharge still exists in supercapacitors. ....	108
Figure 82.	Supercapacitor used for circuit verification and benchmark energy density comparison.....	109
Figure 83.	NTSDM capacitor with 96 mm <sup>2</sup> Grafoil electrode and 8 μm thick anodic film with 199 mF capacitance.....	110
Figure 84.	Low salt NTSDM charge/discharge cycles for various applied voltages. ....	112
Figure 85.	Two discharges from 2.5-volt charge protocol overlaid onto the same graph. ....	113
Figure 86.	NTSDM capacitors with 16.7 wt% NaCl electrolyte reach a high voltage limit of approximately 2.3 volts with 6 volts applied. ....	114
Figure 87.	High salt NTSDM charge/discharge cycles for various applied voltages ....	115
Figure 88.	NTSDM capacitors with 33.3 wt% NaCl electrolyte reach a high voltage limit of approximately 2.01 volts with 6 volts applied. ....	116
Figure 89.	Energy density and maximum achieved voltage trends in a low salt NTSDM capacitor up to 6 volts. ....	118
Figure 90.	Energy density and maximum achieved voltage trends in a high salt NTSDM capacitor up to 10 volts. ....	119
Figure 91.	Comparison of energy density and capacitance for both low salt (left) and high salt (right) capacitors as a function of the applied voltage on charge...	120
Figure 92.	NTSDM capacitor discharge cycles with distinct behavior proposed to be a relic of pseudocapacitance. ....	123
Figure 93.	Typical pseudocapacitance voltage profile consistent with high frequency, constant current cycling. ....	124
Figure 94.	NTSDM capacitor discharge cycles with subtle behavior proposed to be a relic of pseudocapacitance. ....	125
Figure 95.	Same four discharges from Figure 94 overlaid on the same plot. ....	125
Figure 96.	Depiction of the color change within the electrolyte observed during charge cycles.....	127
Figure 97.	Depiction of the excessive accumulation of moisture and the presence of corrosion products (alligator clip has been removed).....	128
Figure 98.	NTSDM capacitor with Grafoil “buffer” and no excess moisture prior to experiment (left) and after an overnight discharge (right).....	129
Figure 99.	Last four charge/discharge cycles with noise (denoted by arrows) after accumulation of moisture within the capacitor and the appearance of rust on the Grafoil “buffer.”.....	129
Figure 100.	Dielectric constant and capacitance vs. film thickness for varying salt concentrations and electrode surface areas. ....	131
Figure 101.	Box and whisker plot of capacitance vs. electrode size.....	132
Figure 102.	NTSDM capacitor energy and energy density vs. film thickness for varying salt concentrations and electrode surface areas. ....	133
Figure 103.	Box and whisker plot of energy vs. electrode size.....	134

Figure 104.	Comparison of recorded and theoretical energy density vs. dielectric thickness.....	136
Figure 105.	NTSDM capacitor leakage resistances (internal and output) vs. film thickness for varying salt concentrations and electrode surface areas.....	137
Figure 106.	Boric acid NTSDM capacitor charge/discharge cycles. ....	139
Figure 107.	Nickel electrode NTSDM capacitor prototype. ....	140
Figure 108.	Charge/discharge cycles for NTSDM with nickel electrode. ....	141
Figure 109.	Best recorded NTSDM specific energy and theoretical specific power overlaid on a Ragone plot of various capacitor and LIB technologies.....	143
Figure 110.	XRD powder diffraction pattern card (page 1 of 2).....	153
Figure 111.	XRD powder diffraction pattern card (page 2 of 2).....	154

## LIST OF TABLES

Table 1.	Comparison of lithium-ion battery and supercapacitor characteristics.....	8
Table 2.	Comparison of various ceramic capacitor energy densities.....	14
Table 3.	Comparison of various EDLC capacitor specific energies and capacitances as well as energy densities.....	16
Table 4.	Variation of tungsten anodization parameters. ....	26
Table 5.	Design of experiments for Titanium Anodization .....	49
Table 6.	Measurements used to calculate effective NTSDM density and weight. ....	87
Table 7.	Summary of titanium anodization results. ....	89
Table 8.	List of various salts and accompanying concentrations used during NTSDM capacitor analysis. ....	103
Table 9.	Control parameters used in NTSDM capacitor method of experiments.....	106
Table 10.	Supercapacitor energy analysis using calculated value for capacitance.....	109
Table 11.	Super capacitor energy analysis based on numerical integration. ....	109
Table 12.	Low and high salt NTSDM capacitances and voltages for varying applied voltages. ....	117
Table 13.	Ascending percent energy stored in Region II according to film thickness, electrode size and salt concentration; cell highlighting denotes affinity to higher salt, larger Grafoil, and magnitude of capacitance. ....	122
Table 14.	Comparison of energy densities and specific energies between “best” ceramic capacitor technologies and NTSDM results.....	142
Table 15.	Table of results for all anodization experiments.....	155
Table 16.	Table of results from NTSDM capacitor experiments (page 1 of 2). ....	157
Table 17.	Table of results from NTSDM capacitor experiments (page 2 of 2). ....	158



THIS PAGE INTENTIONALLY LEFT BLANK

## LIST OF ACRONYMS AND ABBREVIATIONS

A	electrode surface area
BaTiO <sub>3</sub>	barium titanate
C	capacitance
cm	centimeter
COTS	commercial-off-the-shelf
CVD	chemical vapor deposition
d	distance between electrodes
DIW	deionized water
ED	energy density
EDLC	electric double layer capacitor
EMALS	Electromagnetic Aircraft Launch System
F	farads (unit of electrical capacitance)
HESM	hybrid energy storage module
J/cm <sup>3</sup>	joule per cubic centimeter (energy density)
LaWS	Laser Weapon System
LIB	lithium ion battery
mA/cm <sup>2</sup>	milliamps per square centimeter (current density)
MJ	megajoule
mL	milliliter
MLCC	multilayer ceramic capacitor
NaCl	sodium chloride (or salt)
NH <sub>4</sub> F	ammonium fluoride
nm	nanometer

NPS	Naval Postgraduate School
NTSDM	nanotubular super dielectric material
pH	measure of acidity
Q	electrical charge
RC	resistor-capacitor time constant
$R_{\text{int}}$	internal resistance
$R_{\text{load}}$	load resistance
$R_{\text{out}}$	output resistance
SDM	super dielectric material
SEM	scanning electron microscope
TEM	transmission electron microscope
TiO <sub>2</sub>	titanium dioxide (or titania)
$V_{\text{app}}$	applied voltage
$V_{\text{load}}$	voltage recorded at time of open circuit
$V_{\text{peak}}$	peak voltage after open circuit
Wh	watt hour (unit of energy)
WO <sub>3</sub>	tungsten trioxide
wt%	percent by weight
XRD	X-ray diffraction
$\Omega$	ohm (unit of electrical resistance)
$\epsilon_r$	relative permittivity of a dielectric material
$\epsilon_0$	permittivity of free space (or vacuum)
$\mu\text{m}$	micron (or micrometer)

## ACKNOWLEDGMENTS

I would like to thank Professor Jonathan Phillips for his guidance, insight, and support during this process. I greatly appreciate his confidence and trust, as well as the interesting conversations we shared throughout my time at NPS.

Next, this thesis would not be possible without the countless hours of help and direction from Professor Sarath Menon. During the course of this research, Professor Menon unflinchingly responded to short-notice requests for help and demonstrated limitless patience throughout my courses of study at NPS. His dedication and support to the materials science curriculum are invaluable to the students as they learn to use the expensive characterization tools and equipment.

I would also like to thank Professor Claudia Luhrs. Her dedication to all Mechanical Engineering students is apparent in her classroom and in her approachability after hours. Her leadership and enthusiasm for research have time and time again proven vital to the success of students graduating and completing theses in the materials science track.

Finally, and most importantly, I would like to thank my wife, Jenna, for her unconditional love and support during our time at NPS. Proverbs 31 states, “She is worth far more than rubies. Her husband has full confidence in her and lacks nothing of value. She brings him good, not harm, all the days of her life.” Truer words cannot be spoken of my wonderful wife. I must also thank my children, Samuel, Gracie, and Eli, for their boundless love and encouragement even after the many hours I spent away from home. There were many dinnertimes and bedtimes carried out without Daddy’s help, and I am immeasurably grateful for my strong supportive wife and loving children.

THIS PAGE INTENTIONALLY LEFT BLANK

# **I. INTRODUCTION**

## **A. SUMMARY OF FINDINGS**

This research is a continuation of a program to evaluate the performance of capacitors based on super dielectric materials [1]. The hypothesis is that dielectric materials made up of porous electrically insulating solids in which the pores are filled with liquids containing ionic species (e.g., water with dissolved salt) will have very high dielectric values by virtue of the separation of ions in the liquid phase and the concomitant formation of large dipoles [2]. The purpose of this study was to thoroughly characterize a new type of dielectric based on the super dielectric material (SDM) hypothesis: SDM constructed with transition metal oxide nanotube arrays created by anodization on the surface of a metal foil substrate and filled with aqueous sodium chloride.

These dielectrics are called nanotube SDM (NTSDM) because the anodization creates hollow nanotubes, orthogonal to, and bonded to, the original metal surface less than 100 nm across and up to 27  $\mu\text{m}$  in length. This required two related foci. First, the creation of complex nanostructured oxide matrices and the incorporation of said material into a capacitor. For this component of the work, procedures from existing processes [2] were modified to create a simple and repeatable anodization technique suitable for use in a NTSDM capacitor. The second focus is to identify and manipulate controllable variables to optimize the performance of an NTSDM capacitor. Another objective was to test the postulate that NTSDM based capacitors can achieve energy densities up to 20 times greater than those previously reported for electrostatic capacitors and commercially available supercapacitors [3].

The following conclusions were reached. First, a successful recipe for creating structures appropriate for NTSDM applications was developed. Second, the created NTSDMs are excellent dielectrics with dielectric constants greater than  $10^{10}$  in some cases as compared to  $10^5$  for the best widely accepted ferroelectric material, barium titanate [4]. Third, NTSDMs can be employed to create capacitors of unprecedented

energy density. Indeed, NTSDM based on aqueous solutions of sodium chloride consistently were employed to create capacitors with energy densities of order 400 J/cm<sup>3</sup>, which is more than ten times better than the energy density of the best commercial supercapacitors [3]. Fourth, parameters such as nanotube length and concentration of salt in the aqueous solution have a profound, but predictable impact on NTSDM performance. Even more remarkable, it suggests these capacitors with improvement could rival the best lithium ion batteries that have an energy density of approximately 3,000 J/cm<sup>3</sup> [5]. It should be noted this technology is at the “ankle” of the s-shaped development curve, which suggests dramatic improvements may come quickly.

It is important to note that the present work is a successful extension of earlier work performed by a group at the Naval Postgraduate School (NPS) on SDM materials [1],[6]. In the earlier work capacitors were fabricated with refractory oxide powders filled with aqueous solutions containing dissolved salt. High surface area oxide powders, for example alumina of the type used as supports in catalysis, were soaked to incipient wetness with liquids containing high concentrations of ions. These powder based SDM materials were used to create electrostatic capacitors, which had dielectric constants as high as  $10^{10}$ . For example, several alumina powders mixed and filled with salt (NaCl) were found to have dielectric constants as much as seven orders of magnitude higher than that of the best dielectric, barium titanate. The SDM hypothesis, which in essence is an extension of the classical model of polarizable (or ponderable) materials, appears consistent with all data obtained with both the powder based SDMs [7] and the NTSDM introduced in this thesis. Finally, it is notable that the present work indicates that NTSDM may be a faster and easier route to very high energy density capacitors than powder based SDM.

## **B. MOTIVATION**

Modern-day advances in warfighting and peacetime naval operations call for highly capable weapon systems and reliable platforms to carry them. Moreover, the military is moving toward a battlefield bounded by technological advances that

increasingly rely on large quantities of electrical power. The need for inexpensive, compact and reliable power is an obstacle that must be overcome for warfighters to utilize technological capacities without size, weight and cost limitations [8].

Perhaps this dynamic relationship between energy need and practical limitation is no more profound than onboard ships in the U. S. Navy. Significant advances in weapons technology over the last decade will culminate in the deployment of highly capable shipboard systems and precision weapons with high energy demand. The U.S. Navy deployed its first operational directed energy weapon onboard *USS Ponce* (LPD-15) and looks to outfit the DDG 1000 with its electromagnetic rail gun, currently being tested, by the mid-2020s [9], [10]. Additionally, the *USS Gerald R. Ford*-class aircraft carrier is presently testing the Electromagnetic Aircraft Launch System (EMALS) that looks to replace the conventional steam piston actuated flight deck catapult with a linear drive motor [11]. According to the Naval Air Warfare Center (NAWC) [12], the EMALS must accelerate and launch a 27,000 kg (60,000 lb) aircraft in less than 60 m (200 ft) in 2–3 seconds. Such a system will demand 122 MJ of launch energy with a 45-second cycle time. Similarly, the long range goal in the development of a naval railgun is to outfit a ship with long range strike weapon capable of reaching over 300 km with a launch velocity of 2.5 km/s and 64 MJ muzzle energy [13].

As military technological advancements become more prevalent, so does the energy demand to support that technology. This is especially true in the U.S. military as a whole and in the U.S. Navy in particular. With the development and deployment of advanced weapons systems onboard ships, aircraft, and satellites, the Navy is generating a high demand for compact, affordable energy generation, storage, and delivery systems.

The need for such advancements is a strategic decision by the Navy to reduce energy consumption. In opposition to the projected higher shipboard energy demands are the Navy's operational energy initiatives, which aim to reduce the fleet's reliance on fossil fuels and overall energy consumption [14]. The Navy set an energy goal to improve energy efficiency and reduce afloat fuel consumption by 15% by 2020 [14]. Except for in the case of nuclear power warships, peak energy demands onboard ships have dictated the minimum requirements for gas turbine or diesel generators and engines.



Traditionally, ships have been designed to keep additional engines online ready to meet transient demands, a so-called “rolling reserve” that continuously burns fuel at a minimum load waiting for planned or unexpected needs [15]. In an effort to reduce weight and avoid unnecessary fuel consumption, the Navy is looking for shipboard power systems that incorporate batteries and/or capacitors to fill the gap for compact, reliable electric power. Ideally, this design trend calls for single generator operation with high capacity energy storage. Modern designs on such energy storage concepts rely heavily upon proven battery technologies but are increasingly looking for more light-weight alternatives such as capacitors [16].

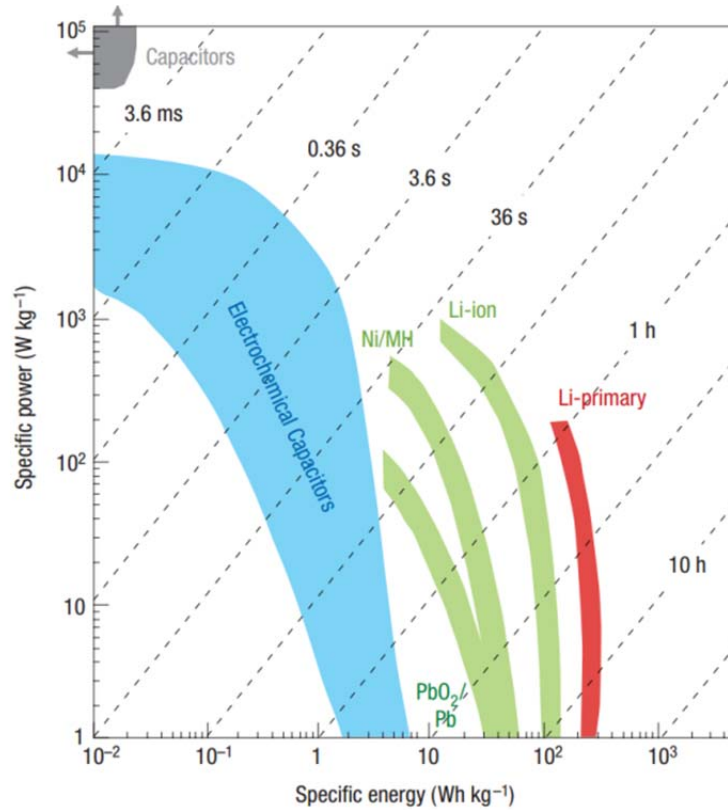
However, the need for capacitors in conjunction with a battery system is not readily apparent. Sudden bursts of demand for battery power, as would be required by any of the above-mentioned weapon systems, tend to significantly degrade battery life. Such degradation in battery performance is even experienced in handheld radios [17]. The peak power required every time a radio is keyed to transmit dramatically reduces the life of its battery. Integrating capacitors in systems that require dramatic pulsed loads can improve battery life [17]. Standard practice uses batteries to slowly charge capacitor banks which are then discharged independent of the battery supply to provide the necessary bursts of high power. This principle can be scaled up to the size and capacity required for shipboard use; thus, smaller and lighter battery/capacitor systems are required to meet shipboard space and weight requirements. The Navy’s demands for high power transient loads aboard an increasingly all-electric fleet are forcing the service to pay considerable attention to alternative energy storage devices which include rechargeable electrochemical batteries and capacitors [18].

The most recent notable developments in electrochemical energy storage revolve around lithium-ion battery (LIB) technology. The promise of a LIB is in the amount of power it can deliver in such a small volume. However, while LIBs offer high power density, it is well known that high charge and discharge rates can be detrimental to their operational life as well as to pose a severe safety hazard [19]. In order to be considered as a viable alternative, LIB rates of operation must be limited by combination with high energy dense electric double layer capacitors (EDLC). Thus, a system incorporating

power dense batteries with energy dense capacitors offers the best of both worlds and is commonly called a hybrid energy storage module (HESM). In the case of shipboard employment, the HESM can source high power loads for extended periods at high rates while generators are down or at the very least long enough to complete a generator startup. Similarly, while the generator is online, the HESM will act as a reservoir and, in fact, improve fuel efficiency by leveling the generator demand at optimum operating speed.

A practical HESM design recently assembled utilizing commercial-off-the-shelf (COTS) components and evaluated in the laboratory environment, was found to be a promising design for shipboard power distribution [20]. As the study points out, LIBs promise energy densities in the range of 100–200 Wh/kg while commercially available supercapacitors promise approximately 10 Wh/kg. Conversely, COTS LIBs are characterized by lower power densities (0.1–0.5 kW/kg) and lower life cycles at higher power applications while supercapacitors offer power densities as high as 5 kW/kg with long life cycles (up to  $10^6$ ) even when operated at extreme power levels. A graphical comparison of LIBs and supercapacitors is presented in Figure 1. Coupling these technologies into a hybrid design allows optimization of weight, volume, power density, energy density and life cycle.

Figure 1. Specific power versus specific energy for different electrical energy storage technologies.



From P. Simon and Y. Gogotsi, "Materials for electrochemical capacitors," *Nature Materials*, vol. 7, pp. 845–854, 2008.

Referring back to the conflict between emerging technologies and the Navy's long-term goals, one additional constraint must be emphasized. Not only will Navy platforms be more fuel efficient, but the platforms themselves will be shrinking. Excluding aircraft carriers, the Navy has plans to deploy smaller surface combatants as the bulk of the fleet in the coming decades [21]. While the envisioned weapons technologies must operate on more fuel-efficient platforms, the platforms themselves must be smaller and thereby be lighter. Again, this trend in ship design coupled with weapons development mandates solutions that may only be delivered through technological innovation, invention, and engineering. This consideration is perhaps most evident in the development of directed energy weapons. Size, weight, and cooling

requirements govern the suitability for high-energy laser weapons on future hulls of the Littoral Combat Ship (LCS) or its Small Surface Combatant (SSC) variants [22].

Over the last two decades, high-profile directed energy programs were canceled after over promising and under delivering [23]. The real-world military applications of such programs were limited by their large volumetric footprint, weight, and energy demands. As evidenced by the Navy's successful deployment of the Laser Weapon System (LaWS) onboard *USS Ponce*, some of these specific hurdles have been overcome. However, in order to outfit a fleet of ships that are a sixth of the displacement of *USS Ponce*, further advances must be achieved in compactness.

In the case of the LCS and its future variants especially, any benefits of electrically hungry weapons are limited by the availability of space to store a main power supply on the ship. In fact, the desired firing rate of a directed energy weapon or rail gun may become the most limiting design parameter for a given ship size. McNab and Beach point out that there are three main options for the interaction between the onboard electric plant and the electric gun [13]:

1. Gun may only use excess power that is available after all other needs have been met such as propulsion in the case of an electrically driven ship.
2. Gun support system includes sufficient storage to fire every round in the magazine.
3. Gun support system includes sufficient storage for a limited number of rounds until a more robust supply has been brought online.

From a military perspective, the second option is certainly the most desirable, but the amount of stored energy necessary would have an immense physical footprint. In the case of the 64 MJ rail gun with an assumed 40% operating efficiency, 160 MJ of energy would be required per shot [13]. This type of demand now becomes comparable to the energy required to launch an aircraft using the EMALS from the much larger aircraft carrier. A single bank of COTS supercapacitors capable of delivering the energy for one shot would alone contribute 4.5 metric tons to ship's displacement. Hence, 100 rounds would require an energy storage weight approximately equivalent to 12.5% of the displacement of the *USS Freedom* variant and 15% of that of the *USS Independence* variant [24].

Hence, the greatest problem faced by even the industry best supercapacitors is their size. The volumetric footprint of a capacitor bank that is required to rapidly fire the newest weapon systems will not easily fit within the space constraints of our modern warships without sacrificing other mission objectives or critical design requirements. As pointed out in the HESM discussion, supercapacitors are today's most viable energy storage capacitor with approximately 30 J/cm<sup>3</sup> [3] as compared to the volumetric energy density of LIBs which is about 100 times greater. If capacitor technology can minimally improve by one order of magnitude, then practical deployment of HESM systems is more achievable and desirable. Table 1 is a comparison of various characteristics between LIBs and supercapacitors.

Table 1. Comparison of lithium-ion battery and supercapacitor characteristics

Characteristic	State of the Art Lithium Ion Battery	Electrochemical Capacitor
*Charge time	~3-5 minutes	~1 second
*Discharge Time	~3-5 minutes	~1 second
Cycle life	<5,000 @ 1C rate	>500,000
Specific Energy (Wh/kg)	70-100	5
Specific power (kW/kg)	**0.5 -1	5-10
Cycle efficiency (%)	<50% to >90%	<75 to >95%
Cost/Wh	\$1-2/Wh	\$10-20/Wh
Cost/kW	\$75-150/kW	\$25-50/kW
* Time for discharge and charge of the useable total energy stored in the devices. ** Power capability of the battery for short duration partial <u>discharge</u> at 90% efficiency.		

From J. R. Miller and A. F. Burke, "Electrochemical capacitors: Challenges and opportunities for real-world applications." *The Electrochemical Society Interface*, vol. 17, pp. 53–57, 2008.

If regular deployment and use of advanced weapon systems is to be achievable on U.S. Navy vessels, then advances in capacitor technology are required. Supercapacitors have been under development for decades, but those that are practically available are expensive and inadequate to meet energy goals and physical constraints outlined before. Given the amount of time and attention that has been invested in the development of EDLC technology, it is probable that the field has reached a critical limit beyond which

breakthroughs in energy density will no longer occur. Accordingly, a new type of capacitor not based on increasing electrode surface area without increasing volume and not based on the known best dielectric material, barium titanate, is needed. It is postulated herein that such a shift in capacitor technology may be achievable by considering the content of this research.

### C. BACKGROUND THEORY

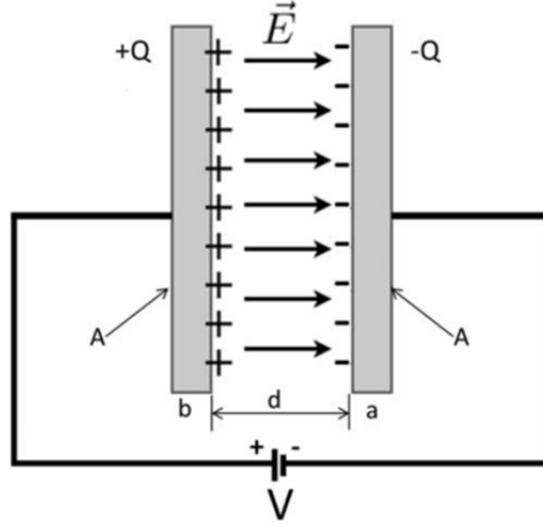
In the electrical sense, capacitance is defined as the ability of an object to store electrical charge. The governing mathematical expression which relates the potential difference ( $V$ ) between objects of charge  $+Q$  and  $-Q$  defines capacitance ( $C$ ) as [25]

$$C = \frac{Q}{V} = \frac{\text{charge}}{\text{potential difference}}. \quad (1)$$

Electrical capacitors, like batteries, store electrical energy, though they work in completely different ways. Unlike a battery that produces electrons and thereby electrical current from a chemical reaction between two terminals, a capacitor simply stores electrons that are produced elsewhere [26]. Nonetheless, the foundational concept of such a device is the storage of charge via an electric field in the space between two conducting electrodes according to Equation (1). A capacitor is charged from a power source, effectively “filling” it with electrons. After disconnecting the source, the energy remains stored until a circuit is completed connecting the two electrodes and “releasing” the stored electrons to the circuit load.

The capacitance of a device is generally calculated as a function of its geometry and its constituent dielectric material properties. Inside a basic capacitor, two terminals are connected to two metal plates separated by a non-conductive substance known as a dielectric depicted in Figure 2.

Figure 2. Basic schematic of a parallel plate capacitor.



From A. P. O'Neal, "The effect of particle size and processing on the properties of a barium titanate polymer composite," Ph.D. dissertation, Dept. Mech. Eng., Univ. California, Los Angeles, CA, 2014.

In theory the dielectric material can be any non-conductive material, though practical application and scientific discovery have found certain materials that are best suited. Dielectrics have a characteristic proper that determines their capacity to store charge under the influence of an electric field. This material specific parameter is referred to as the relative permittivity (i.e., the permittivity of the material with respect to that of vacuum) or dielectric constant.

The most energy dense form of a capacitor, and hence, the geometric almost universally employed, is simply two conductive plates, or electrodes, with a non-electrically conducting material placed between the electrodes. The capacitance for this geometry has a simple relationship between electrode surface area ( $A$ ), the identity of the dielectric, and the distance between the electrodes ( $d$ ):

$$C = \epsilon_o \epsilon_r \frac{A}{d}, \quad (2)$$

where  $\epsilon_o$  is the permittivity of free space, a known constant, and  $\epsilon_r$  is the dielectric constant. One can surmise from Equation (2) that maximizing capacitance may be achieved by increasing plate surface area, minimizing the space between them, picking a

material with high dielectric constant, or a combination of all three. Various distinct capacitor designs have emerged which can be grouped according to the manner in which they manipulate the variables in Equation (2).

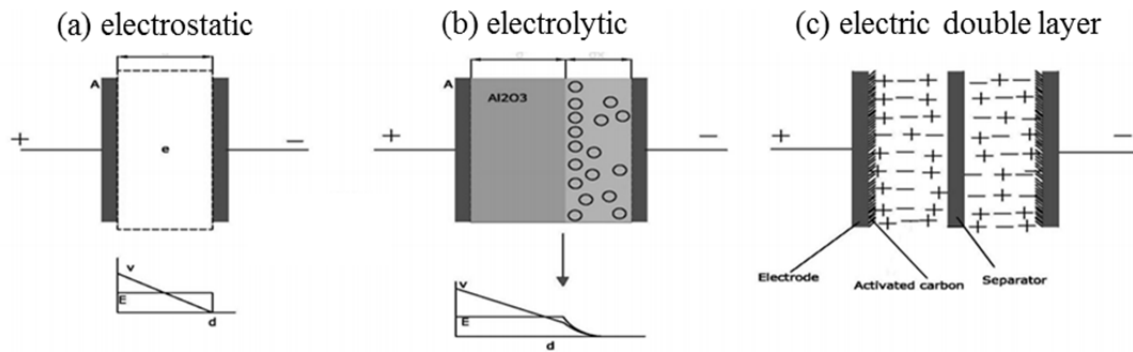
#### **D. CAPACITOR TECHNOLOGIES**

Previous discussion described capacitors with a simple parallel plate design with an incorporated dielectric, also known as an electrostatic capacitor. The next generation capacitor design is an improvement on the simplicity of the electrostatic capacitor. Capacitors in this category are known as electrolytic capacitors. They are similar to batteries in physical makeup except that both the cathode and the anode are of the same material. Commercialized electrolytic capacitor electrodes are usually made of aluminum or tantalum with a ceramic dielectric. A liquid electrolyte contained within actually serves as the negative electrode, though some designs incorporate a solid electrolytic material [27].

The significant increase in capacitance over the first generation design is due to the high surface area between the ceramic and electrolyte interface. Especially in the case of aluminum electrolytic designs, an electrochemical etching procedure is used which creates a high surface area alumina interface [28]. The third generation of capacitors is categorized by the manner in which charge is stored at a metal and electrolyte interface where the main component is activated carbon. These capacitors were previously identified and discussed as EDLCs. Figure 3 portrays three basic designs within which most capacitors can be categorized.



Figure 3. Schematic presentation of electrostatic (a), electrolytic (b), and electric double layer capacitors (c).

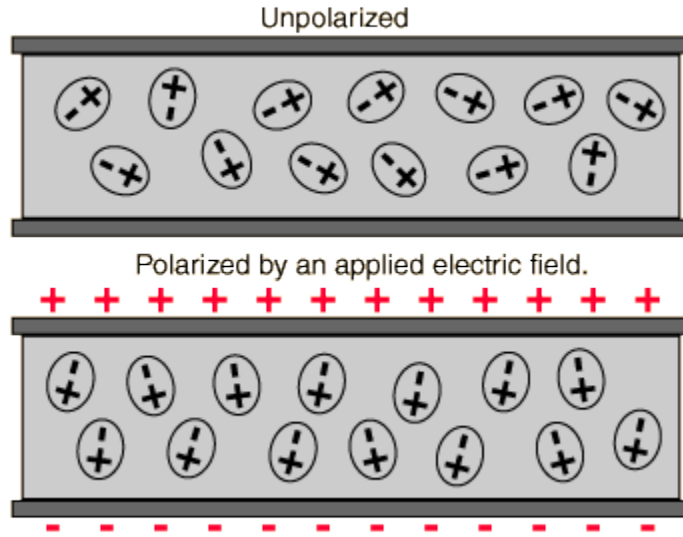


After M. Jayalakshmi and K. Balasubramanian, "Simple capacitors to supercapacitors-an overview," *Int.J.Electrochem.Sci*, vol. 3, pp. 1196–1217, 2008.

## 1. Electrostatic and Electrolytic Capacitors

As discussed earlier, the simplest electrostatic capacitor design achieved great improvement after the introduction of a dielectric. For decades, it has been well documented that barium titanate ( $\text{BaTiO}_3$ ) or other ceramics derived from  $\text{BaTiO}_3$  have proven to be the best dielectric material [4]. That is, barium titanate routinely exhibits capacitive behavior with some of the highest recorded dielectric constants at values up to 10,000 [29]. A dielectric material reacts to an electric field because it contains charge carriers that can be displaced. This polarization phenomenon within the material effectively creates dipole chains which align themselves parallel to the field developed between the electrodes [30]. Figure 4 is a portrayal of the dipole alignment within a dielectric material.

Figure 4. Depiction of dipole alignment within a polarizable media.



From (2014, September 8). *How do we conclude that polarized dielectric in electric field reduces overall field?* [Online]. Available: <http://physics.stackexchange.com/questions/134542/how-do-we-conclude-that-polarized-dielectric-in-electric-field-reduces-overall-field>.

An advanced type of ceramic capacitor is the multilayer ceramic capacitor (MLCC). This approach to increased capacitance consists of alternating layers of metal electrodes and dielectric ceramics with an end goal of reducing the distance between electrodes. MLCCs typically consist of approximately 100 of the alternating layers sandwiched between two ceramic covered layers. Most commonly, the electrode is made from silver-palladium while  $\text{BaTiO}_3$  is the dielectric material [27]. The success in reducing the size, and thereby improving energy density, of this type of capacitor relies on decreasing the thickness by reducing the distance between the metal plates.

Studies have shown that the ferroelectric properties of dielectric materials, such as  $\text{BaTiO}_3$ , will decrease as particle and grain sizes decrease [4]. One study estimates the critical particle size at which  $\text{BaTiO}_3$  dramatically loses its great dielectric performance to be around 10–20 nm [29]. Because MLCCs rely heavily on the compact nature of  $\text{BaTiO}_3$  ceramic material, there is an expected minimum thickness for the intermediate dielectric layers at approximately 0.5  $\mu\text{m}$ . Hence, MLCC technology appears to be approaching a theoretical maximum achievable energy density. Table 2 is a list of various types of

electrostatic capacitors with ceramic dielectrics found in the literature. Of note, the precursor to the NTSDM capacitor studied herein (titania nanotubes with sodium nitrate electrolyte) has proven one order of magnitude improvement over the best BaTiO<sub>3</sub> derived ceramic capacitors.

Table 2. Comparison of various ceramic capacitor energy densities.

<b>Dielectric Material</b>	<b>F/g</b>	<b>F/cm<sup>3</sup></b>	<b>J/g</b>	<b>J/cm<sup>3</sup></b>	<b>Ref.</b>
barium titanate nanocubes	--	--	--	5	[31]
barium strontium titanate nanowires	--	--	--	15	[32]
lead lanthanum zirconate titanate	--	--	--	22	[33]
polymer	--	--	--	27	[34]
titanium nanotubes with aqueous solution of sodium nitrate	34	114	70	230	[2]
Note: All energy densities are either taken from the original paper or calculated using the highest operational voltage shown therein; missing entries are from references containing inadequate data to calculate values.					

After F. Quintero and J. Phillips, "Tube-super dielectric materials: electrostatic capacitors with energy density greater than 200 Jcm<sup>-3</sup>," unpublished.

## 2. Double Layer Capacitors

The youngest design which accounts for the bulk of recent capacitor research is the double layer capacitor of which there are two types: electric double layer and electrochemical double layer [35], [36]. Both are collectively referred to as EDLCs, supercapacitors categorized in the latter. EDLC research focuses on increasing the electrode surface area in order to improve capacitance. This is achieved by capitalizing on the principle of double-layer capacitance at the interface between electrode and electrolyte. EDLC designs are unique from all those previously discussed, because ionic species contained within the electrolyte, rather than dipole alignment within a ceramic dielectric, facilitate the accumulation of charge on the electrodes. Mobile ionic charges within the electrolyte accumulate near the electrode surfaces (normally carbon), and charges of opposite polarity (electrons or "holes"), accumulate on the electrode. Slightly different, supercapacitors store energy by sustaining a Faradic reaction between the

electrode, usually a transition metal oxide or carbon/oxide mixture, and the electrolyte. This characteristic is sometimes referred to as pseudocapacitance [27].

So called supercapacitors are fundamentally the same as all other parallel plate capacitors as described by Equation (2). The only significant difference is the creation of a very high surface area electrode in a very small volume. All of the activated carbon on either the anode or cathode side is at the same potential. Essentially, the mechanism at work within the electrolytic solution can be described as “dipoles” forming within the “dielectric.” This is equivalent to the dipole formation in a solid dielectric upon application of an electrical potential difference across the two electrodes. In a supercapacitor, these dipoles are concentrated in the liquid layer within nanometers of the carbon electrode.

The nature of this double layer design is such that it is difficult to assign a dielectric value or even thickness. Instead, the dielectric constant and the thickness are generally lumped together and designers use a more convenient parameter: capacitance per unit surface area of the carbon electrode which is approximately  $10 \mu\text{F}/\text{m}^2$  for EDLC designs. Another unique element of a supercapacitor is the separator. Carbon from the capacitor anode cannot be allowed to touch carbon from the other electrode as this would short the capacitor.

This capacitor technology has the ability to store higher quantities of energy than conventional capacitors and can deliver much improved power density over batteries at least for a short period upon initial discharge [27]. The specific energies and energy densities for various EDLC designs are listed in Table 3.

Table 3. Comparison of various EDLC capacitor specific energies and capacitances as well as energy densities.

Electrodes	Electrolyte	F/g	F/cm <sup>3</sup>	J/g	J/cm <sup>3</sup>	Ref.
activated carbon	aqueous	238	119	86.4	43.2	[37]
graphene aerogel	aqueous	223	--	112	--	[38]
PbO <sub>2</sub> /activated carbon	aqueous	132	66	180	90	[39]
vanadium pentoxide	ionic liquid	--	--	190	--	[40]
graphene hydrogel and nickel foam	aqueous	1369	--	198	--	[41]
carbon foam	aqueous	--	--	227	114	[42]
TiC conductive clay		--	900	--	115	[43]
compressed activated microwave expanded graphite oxide	ionic liquid	147	110	227	173	[44]
activated carbon	deep eutectic solvent	140	70	260	130	[45]
vanadium oxide and polymer	gel	412	--	295	--	[46]
graphene	ionic liquid	--	--	306	153	[47]
carbon nanotubes on carbon nanofiber	ionic liquid	--	--	356	178	[48]
graphene	organic	298	212	457	324	[49]
Note: All energy densities are either taken from the original paper or calculated using the highest operational voltage shown therein; missing entries are from references containing inadequate data to calculate values.						

After F. Quintero and J. Phillips, "Tube-super dielectric materials: electrostatic capacitors with energy density greater than 200 Jcm<sup>-3</sup>," 2015.

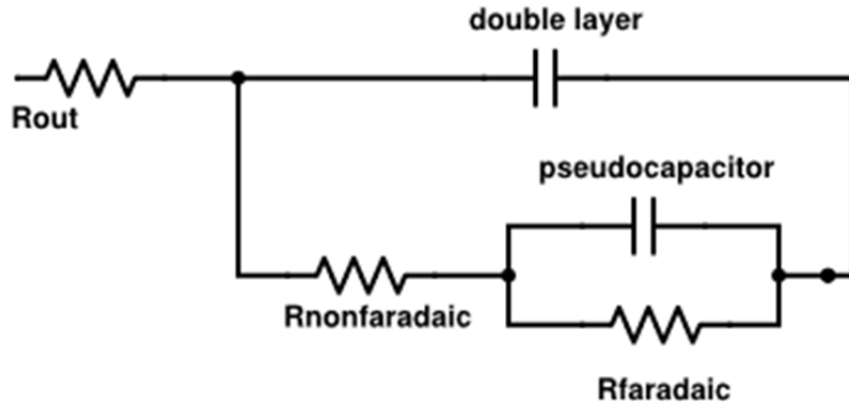
### 3. Pseudocapacitance

Additional discussion on the pseudocapacitance phenomenon is prudent due to its relevance to NTSDM capacitors. It is helpful to again refer to the classical distinction between capacitors and batteries. In the former, positive and negative charges collect and reside at a two-dimensional charge density on the electrode plates and are easily released when the charging source is replaced with a load. However, a charged electrochemical cell stores charge indirectly. In the case of supercapacitors, stored charge is released to a circuit load through an accompanying electrochemical Faradaic process facilitating charge transfer across the electrode and electrolyte interface. The Faradaic processes usually involve a change to the oxidation state of the materials in the cell [50]. Hence, classic capacitor charge/discharge is distinguishable as "non-Faradaic" and pseudocapacitance processes are distinguished, at least in part, as "Faradaic."

Earliest proposed and developed EDLC designs [51], [52] relied on high-area carbon powder electrodes and some form of salt electrolyte. The expected high energy storage was based on the large accessible surface area per gram in carbon powder materials as well as its theoretical double layer capacitance. The theoretical specific capacitance for such double layer capacitors was calculated to be as high as 250 F/g, however practically attained values were an order of magnitude smaller due to the limited accessibility of electrolyte and high surface area contact [53]. Where double layer capacitors incorporate an aqueous electrolyte, the prospective energy density is further limited by a relatively low operating voltage at around 1.4 volts. This limit is largely determined by the breakdown of water at 1.23 volts as well as other kinetic factors [1]. Discussed later in this study, related behavior was observed in some cases when NTSDM capacitors were discharging between 1.3 volts and 1.0 volts. Double layer capacitors made up of non-aqueous electrolytes reach operating voltages as high as 4.0 volts, which is desirable since energy density increases proportional to voltage squared; however, the solid electrolyte usually has a lower conductivity so rated capacitances are usually lower.

Pseudocapacitance is known to appear in cases where Faradic charge transfer, for thermodynamic reasons, causes accumulation of charge. This is unlike the ideal Nerstian processes in batteries where constant electrode potential adjusts the thermodynamic equilibrium condition which forcing the electrochemical reactions. Conway and Gileadi [54] propose that pseudocapacitance charge/discharge processes lead to experimentally observable capacitances which are usually dependent on potential. Because supercapacitors also non-Faradaically store charge at the electrode/electrolyte interface, an additional double layer capacitance is believed to exist in some parallel coupling to the pseudocapacitive storage. Again, this behavior is observed in NTSDM capacitors and will be discussed in later analysis; however, the two separate capacitance values were not experimentally determined or analyzed. Figure 5 is an equivalent circuit representation of double layer (non-Faradaic) and pseudo (Faradaic) capacitances.

Figure 5. Equivalent circuit for a capacitor electrode interface demonstrating Faradaic and non-Faradaic capacitances.



After B. Conway, V. Birss, and J. Wojtowicz, "The role and utilization of pseudocapacitance for energy storage by supercapacitors," *J. Power Sources*, vol. 66, pp 1–14, 1997.

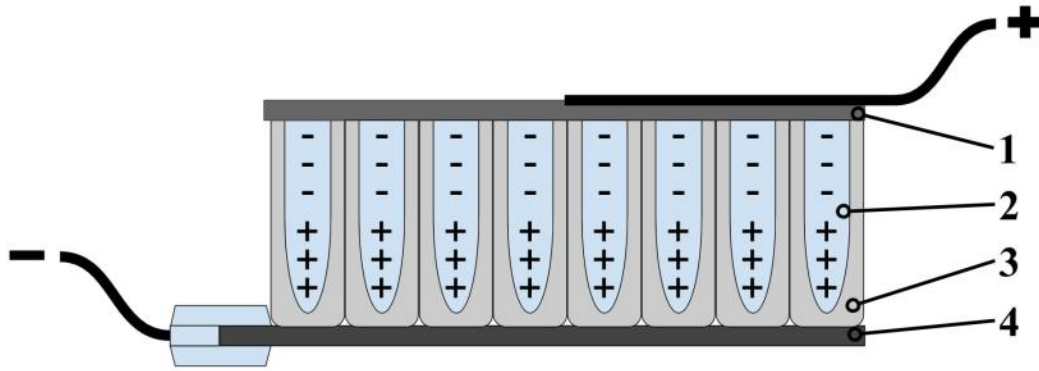
#### E. FOCUS OF PRESENT STUDY

The foundation for this study asserts that the principal characteristic of dielectric materials is that they should be polarizable under the influence of an electric field [55], [56]. More precisely, the material should permit a redistribution of charge when an external influence is applied across the surrounding electrodes. Dielectric material of all makes must adhere to the requirement that it acts as an insulator against shorting out the positive and negative electrodes. However, the best polarizable materials are generally electrical conductors. Therefore, a hypothesis is put forward that improves upon those tested in earlier work at NPS [1], [2]. The earlier studies put forward a simple theory to explain the existence and behavior of SDMs. A non-conductive porous solid in which pores are filled with an aqueous solution with sufficient concentration of dissolved ions will have a high dielectric constant. In effect, non-ferroelectric material can be created by the introduction of a polarizable electrolyte which remains completely insulated by the presence of the containing porous insulator. This study further demonstrates that highly structured oxide films may serve as the non-conductive material while simple salt (NaCl) water is introduced as the electrolyte contained within. This research is separated in two distinct efforts:

1. Fabrication and characterization of nano-structured oxide films by means of electrochemical anodization
2. Incorporation of those films in the fabrication and evaluation of those films in an energy dense capacitor.

The resulting NTDSM capacitor is considered a second generation, energy dense improvement upon the SDM capacitor design. Figure 6 is a schematic of the proposed makeup of each NTDSM capacitor in which the scale of the oxide nanotubes has been grossly exaggerated relative to the titanium and Grafoil electrodes as depicted.

Figure 6. Schematic of NTDSM capacitor with Grafoil positive electrode (1), aqueous electrolyte (2), tubular oxide structure (3), and metal substrate as negative electrode (4).



The NTDSM capacitor is fundamentally different from all other types of capacitors, though exhibits behavior and contains attributes individually unique to electrostatic, electrolytic, and double layer capacitors. For example, the basic design is that of an electrostatic capacitor, but the measured dielectric constants increase with increasing separation between the electrodes (and in this case the length of the nanotubes) contrary to the mathematical model in Equation (2). There is some evidence that capacitances increase with applied voltages on charge and discharge similar to EDLCs. The proposed model also predicts higher salt concentrations cause stronger dipoles and should therefore create higher capacitances and energy densities, though this relationship was not fully investigated or understood.



The first objective of this study is to select a suitable substrate, oxide film, and electrolyte to make up the NTSDM capacitor. Secondly, to evaluate the capacitor on its merits: measured capacitance, dielectric constant, energy delivered, and energy density. Finally, establish a correlation between various parameters in order to optimize NTSDM capacitor design.

## II. ANODIZATION OF TUNGSTEN

### A. INTRODUCTION

As stated earlier, the first focus of this research is to achieve the creation of a complex nanostructured oxide matrix in order to incorporate that material into an NTSDM capacitor. In particular, a major goal is to find an alternative to titanium in order to potentially increase energy density and to solve scientific “puzzles” associated with the NTSDM model. This chapter describes an effort to create an alternative to titania anodic films. Specifically, an extensive effort was made to create nanotube arrays on tungsten foils.

A scientific basis for the work with tungsten is to provide a test of the generality of the NTSDM hypothesis. That is, all present NTSDM based capacitors, described in greater detail in subsequent chapters, are based on a single material, titanium dioxide anodic films. Although, the NTSDM hypothesis indicates the remarkable behavior observed should be independent of the metal, data to support the generalized hypothesis is lacking. Another scientific issue regarding the availability of a metal, other than titanium, having tightly packed hollow metal oxide nanotube geometry, may help resolve the basis for the maximum operating voltage of the NTSDM capacitor. Indeed, it is not clear why the titanium NTSDM capacitors function as energy storage devices up to slightly more than 2 volts. This is significantly above the breakdown of water to create ions, and thus, may not be the source of the ultimate operating voltage. Certainly, with powder-based SDM capacitors discussed in detail in earlier NPS publications [1], [7], the operating voltage is near 1 volt, which is consistent with the limit imposed by the breakdown of water into a conductive ion solution. A theory presented herein is that the breakdown occurs across the oxide/metal interface. If this is truly the case, the identity of the original metal may significantly impact the ultimate operating voltage of an NTSDM capacitor.

There is a strong basis in NTSDM based capacitor technology for this work. The factors that determine the ultimate energy density of a nanotube array are not clear. For

example, if the maximum voltage is dependent on the metal identity, as discussed above, then the metal identity can greatly impact net energy density as capacitive energy density is proportional to voltage squared. Also, the shape of the nanotube array, the chemistry of the interaction between salt and nanotube walls, and other unknown factors dependent on metal and metal oxide identity, can also impact the net dielectric constant of the system, and hence the net energy density. A recent NPS study [1] demonstrated that the identity of the refractory oxide power in power-based SDM capacitors can impact the dielectric constant by two orders of magnitude. A similar result may be obtained with NTSDM capacitors as a function of the original metal identity. Given the lack of a precise theory, it is necessary to employ an “Edisonian” approach to the optimization of energy density.

This chapter outlines the testing and evaluation of an electrochemical anodization technique specifically for tungsten trioxide ( $\text{WO}_3$ ). The techniques and results presented herein were found to be ill-suited for NTSDM capacitor analysis. However, this research identified a simple and inexpensive means to create nanoscale porous tungsten trioxide ( $\text{WO}_3$ ) film on tungsten substrates via electrochemical anodization. Further refinement of the procedure contained herein may result in a suitable oxide film for further NTSDM analysis.

## **B. BACKGROUND ON TECHNIQUE**

Tungsten trioxide nanofeatured films have highly advantageous benefits when used in the creation of semiconductors. This is due to the small band gap energies of tungsten, deep valence band and stable physicochemical properties [57]. Devices that utilize  $\text{WO}_3$  often exhibit low power consumption, good memory effects and have high contrast ratios [58]. However, this research aimed to evaluate anodized tungsten as a viable NTSDM capacitor.

Anodizing methods for creating nanofeatured films in aluminum and titanium have been extensively studied under a variety of different conditions [59], [60], [61]. From these studies, the observed results from differing voltage and dwell times have established that there is a direct correlation between voltage and barrier layer thicknesses [59]. These anodizing methods used a variety of different acidic electrolytes at varying

concentrations to include sulfuric acid, oxalic acid and phosphoric acid [60]. In the case of anodized aluminum, much of the research was driven from a need to create strong, lightweight, corrosion resistant aircraft components [59].

As stated in the literature, there is insufficient research in the study of  $\text{WO}_3$  thin films [57], [62]. The current desire to create improved semiconductors is now generating a demand for this current research much in the same way that the aviation needs drove the Aluminum research. Studies thus far regarding the creation of tungsten trioxide nanofeatured films involve the use of acidic electrolytes in their nanofeature film production methods [59], [60], [62]. Previous studies varied concentrations of fluoride oxides in order to produce nanofeatured films. However, it is believed the morphology of anodic  $\text{WO}_3$  thin films is greatly dependent on the anodization times and applied voltages in addition to fluoride concentration. Methodically varying these parameters should change film thickness and pore size among other attributes. The novelty of this work is that it seeks to identify optimal conditions for porous thin film production for use in a NTSDM capacitor.

Using a controlled growth method to produce symmetrically aligned nanotube structures have proven difficult to fabricate [57]. This difficulty has led to an alternative approach to creating these films. Rather than growing thin nanofeatured films, we instead create them. In this method tungsten nanofeatured layers are fabricated through electrochemical anodization, where nanofeatures are created in layers. The anodization process used in this study created  $\text{WO}_3$  thin films with nanofeatures using  $\text{NH}_4\text{F}$  in an electrolyte with weak acidity and pure titanium cathodes. The Pourbaix diagram for tungsten has shown that  $\text{WO}_3$  is stable at low pH values [63]; however, the high potentials used during anodization tend to promote  $\text{WO}_3$  stability. The variables of this study included anodization potential and duration. The results of this study detail the optimal conditions of those considered for the creation of  $\text{WO}_3$  nanofeatured films. Although the film crystalline structure was not analyzed, the as-formed films are presumed to be amorphous for non-annealed films as has been found in the literature [64].

## C. EXPERIMENTAL SETUP AND METHODS

The following sections outline the materials, equipment, and procedures used to anodize tungsten substrates. In general, the method chosen to anodize tungsten borrowed heavily from earlier protocols used at NPS to anodize titanium [2]. As the experimental protocols were used, the specific procedures were adjusted according to the quality and dependability of the resulting anodic films. Ultimately, the procedures documented hereon closely resemble procedures outlined in existing literature [57], [65], but were altered in order to facilitate anodization in a simpler, less expensive laboratory environment.

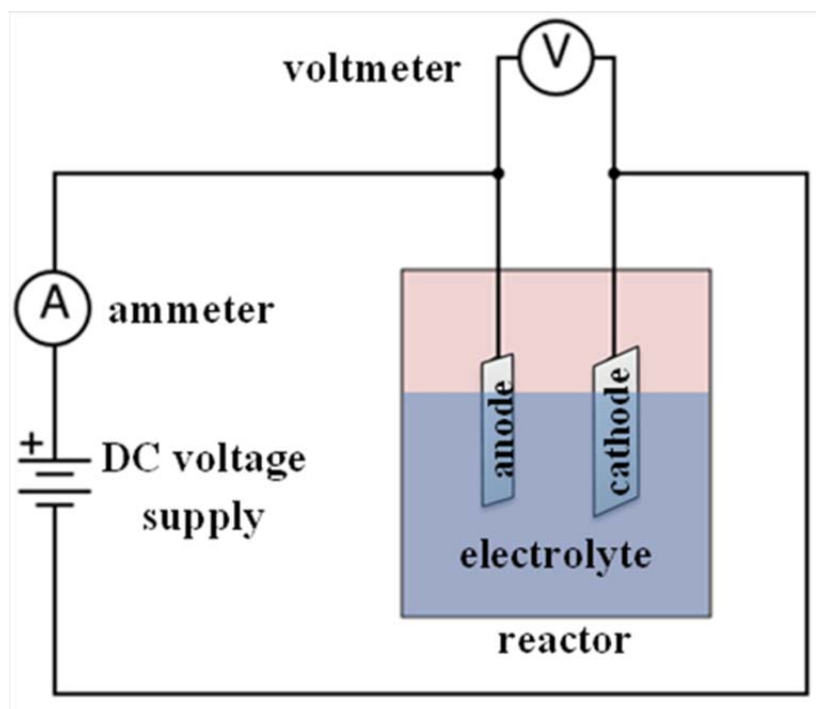
### 1. Anodization Materials and Equipment

All experimental procedures were carried out with commercially available chemicals and materials of the highest available purity. Deionized water (DIW) was used to prepare all aqueous solutions. Nanoporous  $\text{WO}_3$  films were created by anodizing 0.05 mm thick, 99.9% pure tungsten foil (Aldrich) substrates using a process similar to but unique from those described in the literature [57], [65].  $\text{WO}_3$  films were grown by anodization in a solution containing 0.25%wt  $\text{NH}_4\text{F}$  (Aldrich) and 2.75wt% DIW in 97 wt% ethylene glycol (Aldrich). The resulting electrolyte was a 3:97 mixture of 2.5M  $\text{NH}_4\text{F}$  in ethylene glycol. It is proposed that the fluoride ions within the electrolyte diffuse to the tungsten surface towards the  $\text{WO}_3$  interface and induce further growth of the oxide layer under applied potential. The electric field across the oxide layer of  $\text{WO}_3$  induces the polarization of W-O bonding, which is able to transfer the  $\text{W}^{6+}$  ions from the pores and leave behind random pits [57]. It is proposed that varying the combinations of anodization voltage and time will have the greatest influence on the  $\text{WO}_3$  film surface morphology and thickness.

The anodization was performed in a two-electrode electrochemical cell using a 0.05mm thick, 99.6% pure titanium cathode (GalliumSource, LLC) measuring 1.6 cm wide by 3.5 cm tall. Figure 7 is a circuit schematic which includes the electrochemical cell contained within a plastic cup as a reactor. The tungsten substrates were cut to 1cm wide by 2.5 cm tall, thoroughly rinsed with ethyl alcohol, dried in air, and suspended

within the electrolyte parallel to the cathode with 2 cm of separation. Many other procedures found in the literature entailed a more intensive pretreatment such as ultrasonication or electrochemical polishing, but a simple rinse and dry method was found to be sufficient for the purposes of this study [57], [59], [60], [62], [65]. Both cathode and anode were partially immersed in the electrolyte, leaving a 0.5 cm portion exposed ensuring an alligator clip had room to engage without touching the electrolyte. In the case of tungsten anodization, the effective anodic surface area used to calculate current density was 4 cm<sup>2</sup> which included both sides of the anode.

Figure 7. Schematic of the electrochemical circuit used to anodize tungsten substrates.



## 2. Experimental Method

To discover any correlation between nanoporous film synthesis and anodization parameters, anodizing potential and duration were varied as outlined in Table 4.

Table 4. Variation of tungsten anodization parameters.

<b>Voltage</b>	<b>Durations</b>		
40 V	60 min	90 min	
20 V	5 min	10 min	15 min
20 V	30 min	45 min	60 min

The DC power supply was set to supply a constant 20 V and 40 V for the two cases. Unlike some anodization methods from the literature, the desired anodization potential was immediately applied at start rather than a linear voltage sweep [9], [57]. For the duration of the anodizing treatment, the electrical current in milliamps (mA) was recorded using a UNI-T UT71B digital multimeter. The recorded current was converted to current density (mA/cm<sup>2</sup>) by dividing by the immersed surface area for each specimen (4 cm<sup>2</sup>). When treatment was complete, the anodized substrates were once again rinsed in ethanol and dried in air. No thermal treatment was performed to the anodized substrates.

Small portions of each sample were cut and mounted for subsequent scanning electron microscope (SEM) analysis (Zeiss Neon 40 Field Emission SEM, 2 keV). During SEM analysis, it was noted that significant activation of the oxide film was occurring even with a 2 keV electron beam. At large magnifications conducive to observing and characterizing nanofeatures, any traces of the nanoporosity disappeared before images could be captured. Consequently, the 5 min, 10 min, and 15 min samples anodized at 20 V were sputtered with 2.6 nm of platinum-palladium (Cressington Sputter Coater 208HR) in an effort to mitigate the oxide film activation. Those particular samples were re-analyzed in the SEM.

#### **D. ANALYSIS**

The following sections outline the results of tungsten anodization protocols. In general, the resulting oxide films were found to contain nanofeatures, but experienced significant substrate degradation. The effects of anodizing potential and duration are presented alongside the anodic current densities for each protocol used. The characteristics of each oxide film and tungsten substrate were assessed by analyzing SEM imagery, and in some cases, naked eye inspection after anodization. Ultimately, a

successful anodization technique that apparently creates a nanoporous oxide film is presented.

### 1. Anodizing Voltage and Duration

Some of the earliest research into the fabrication of nanoporous  $\text{WO}_3$  utilized a galvanostatic or constant current anodization process [66]. This study utilized a constant potential anodization where the potential across the electrochemical cell was energized to the desired voltage and held constant for the desired duration. Figure 8 plots the current density over time during the 60 minute 40 volt, and 20 volt anodization procedures. The dynamic response in the first 2.5 minutes of the treatment is shown in Figure 9.

Figure 8. Anodization current densities over 1 hour.

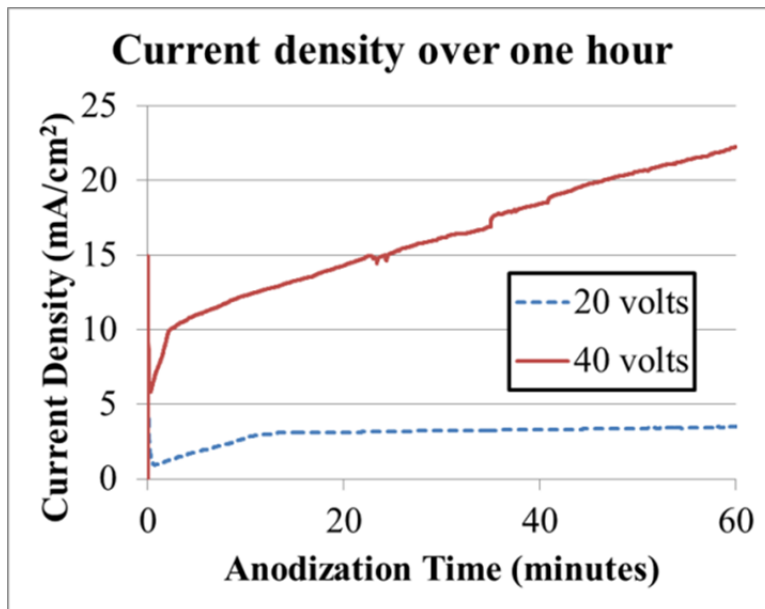
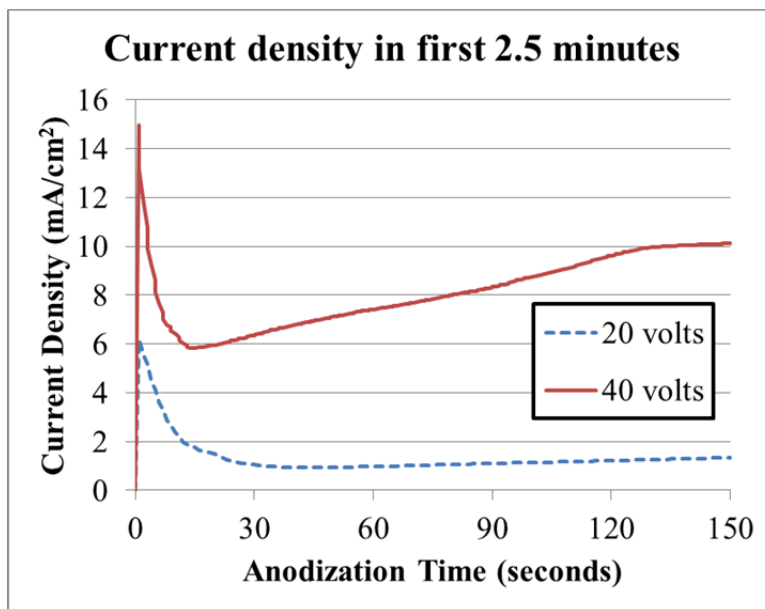




Figure 9. Anodization current densities in the first 2.5 minutes.



Both curves follow the characteristic trend of oxide formation in an electrolyte during anodization which will be discussed in greater detail in the following chapter. Current densities are directly proportional to the reaction rates occurring on the surface of the anode. Clearly, at all times the 40-volt anodization has much a higher reaction rate than that of the 20-volt anodization. This is due to a rapid dissolution of the newly formed oxide material, the thermodynamics of which are described in previous studies for various metals [67], [68].

The initial spike, more apparent in Figure 9, is the current transient immediately after the power supply is energized. This spike is immediately followed by a rapid decay in the initial stage of anodization down to a local minimum. Similar trends have been reported for various other studies regarding compact oxide film synthesis [59], [67], [69]. The current density drop is due to the formation of a barrier oxide layer. The layer is formed according to the local field influence in the vicinity of the anode. The current densities in the initial stage of anodization depend on the anodic potential. That is, higher current densities are expected for higher applied potentials [70]. The end of this first stage is marked by pore initiation and growth, due to the solubility of oxides in the  $\text{NH}_4\text{F}$

electrolyte. Thus, the current density increases until a balance between fluoride induced dissolution of the oxide film and potential induced oxide layer growth is achieved if at all.

The literature suggests that the current density (or reaction rate) reaches a constant value if an equilibrium or steady-state condition can be established [69]. Various studies regarding oxide film formation indicate that the resulting morphology is strongly affected by the applied potential [71], [72]. It is then apparent from Figure 2 that the 20-volt anodization reaches a steady-state value at approximately 13–15 minutes, at which point the rate of barrier layer formation is equal to the rate of porous layer formation (oxide dissolution). In contrast, the 40-volt anodization appears to have a runaway oxide dissolution rate. The rate slows at approximately 2 minutes, but the reaction rates are shown to increase over the entire time recorded. That is, the rate at which the barrier film is being produced cannot compensate for the rate at which it is being dissolved. Without any further analysis, it is apparent that the 40-volt anodization will likely not result in a highly structured porous film.

The higher current density in the 40-volt anodization also resulted in an elevated electrolyte temperature, as Joule heating of the anode created a convective current within the reactor. The electrolyte temperature after 1 hour of 40-volt anodization was recorded as 43°C by FLIR thermal imaging camera, while the 20-volt electrolyte remained at room temperature.

## **2. Characterization**

Upon completion of the anodization process, resulting  $\text{WO}_3$  film structure and morphologies were characterized by optical microscopy and SEM techniques. Figure 10(a) shows the appearance of the  $\text{WO}_3$  layer film to the naked eye immediately after the anodic treatment at 20 volts for 15 minutes. The surface of the W foil after undergoing anodization exhibits a distinct purple hue which is apparent to the naked eye and to some degree under the optical microscope. Figure 10(b) is a photograph of the badly disintegrated 40 volt, 90 minute tungsten substrate with apparent pitting and film

degradation noted throughout the surface of tungsten film. Note that the original specimen was a perfect 1cm by 2.5cm rectangle.

Figure 11(a) is a micrograph of the 20 volt, 15-minute film at low magnification. No visible corrosion, pitting, or film degradation was noted at this magnification. Figure 11(b) is a micrograph of the tungsten specimen after it was anodized at 40 volts for 90 minutes. From the black specks which are actually signs of severe pitting, it is apparent that the specimen experienced film degradation and substrate disintegration during anodization. After approximately 40 minutes, the edges of the tungsten specimen appeared to be turning blue. This was later recognized as the onset of substrate disintegration within the electrolyte. The rapid degradation became apparent after 60 minutes, at which point the edges and corners were dissolving and byproducts were observed to settle at the bottom of the reactor. At the 90-minute mark, the anodization process was stopped to prevent the complete dissolution of the substrate.

Figure 10. Naked eye comparisons of  $\text{WO}_3$  film for 20 volt 15-minute anodization (a) and for 40 volt 90-minute anodization (b).

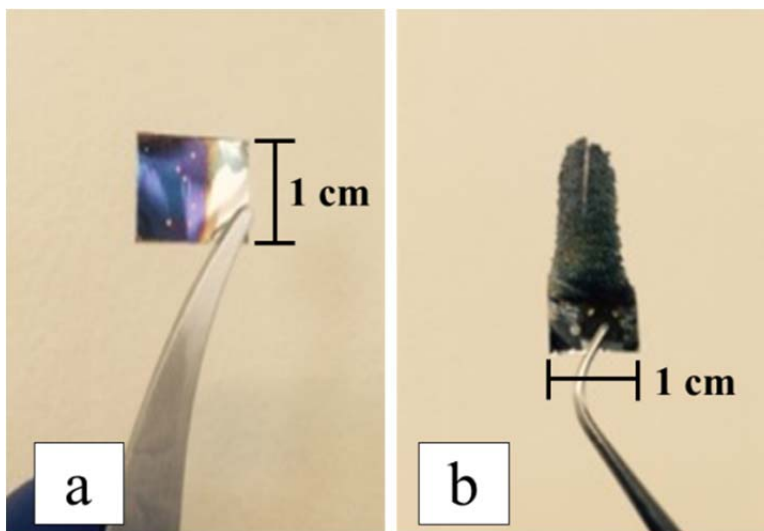
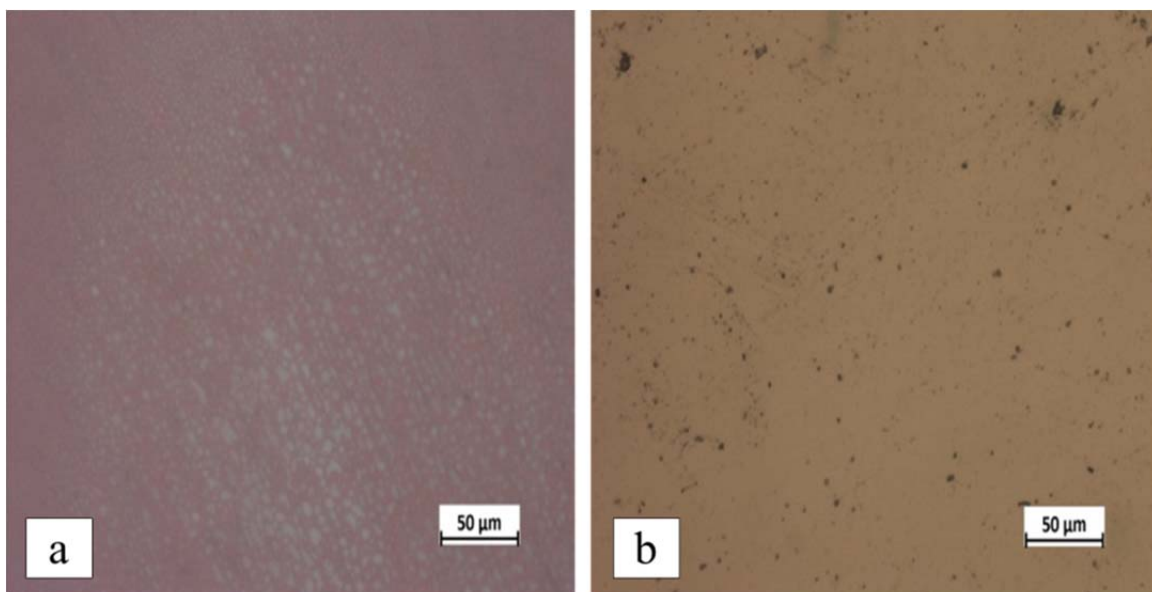


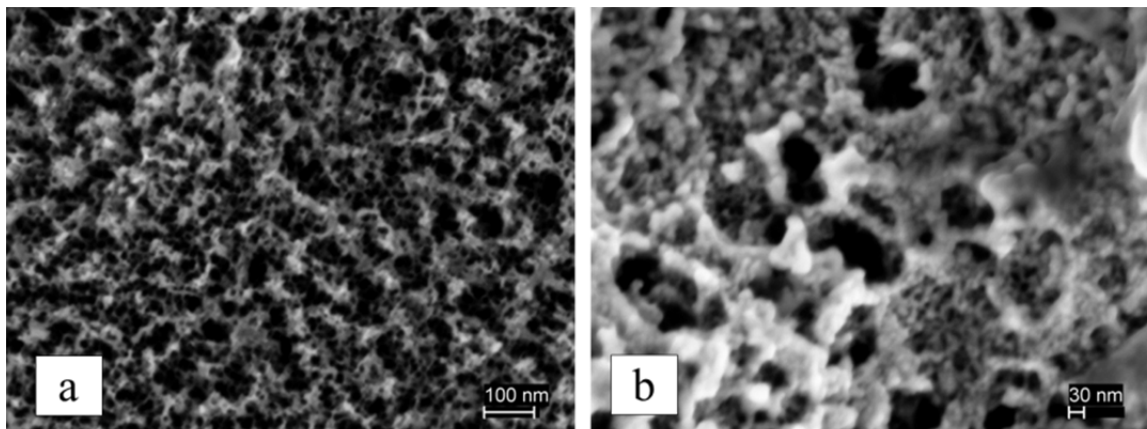
Figure 11. Optical micrographs of the 20 volt 15-minute  $\text{WO}_3$  film (a) and the 40 volt 90-minute  $\text{WO}_3$  film (b) at low magnification.



### 3. Anodization at 40 Volts

This section will discuss the results found after anodization under 40 volts. Specimens were anodized and characterized under the SEM according to the times listed in Table 1. Due to high corrosion observed during the experiment, the voltage was reduced to 20 volts and the experiment was conducted using solutions of the same electrolyte concentration for durations of 5, 10, 15, 30, 45, and 60 minutes. The nanoporous films created by 40-volt anodization potential are displayed in Figure 12.

Figure 12. SEM images of the 40 volt 60-minute sample (a) and of the 40 volt 90-minute sample (b) at high magnification.

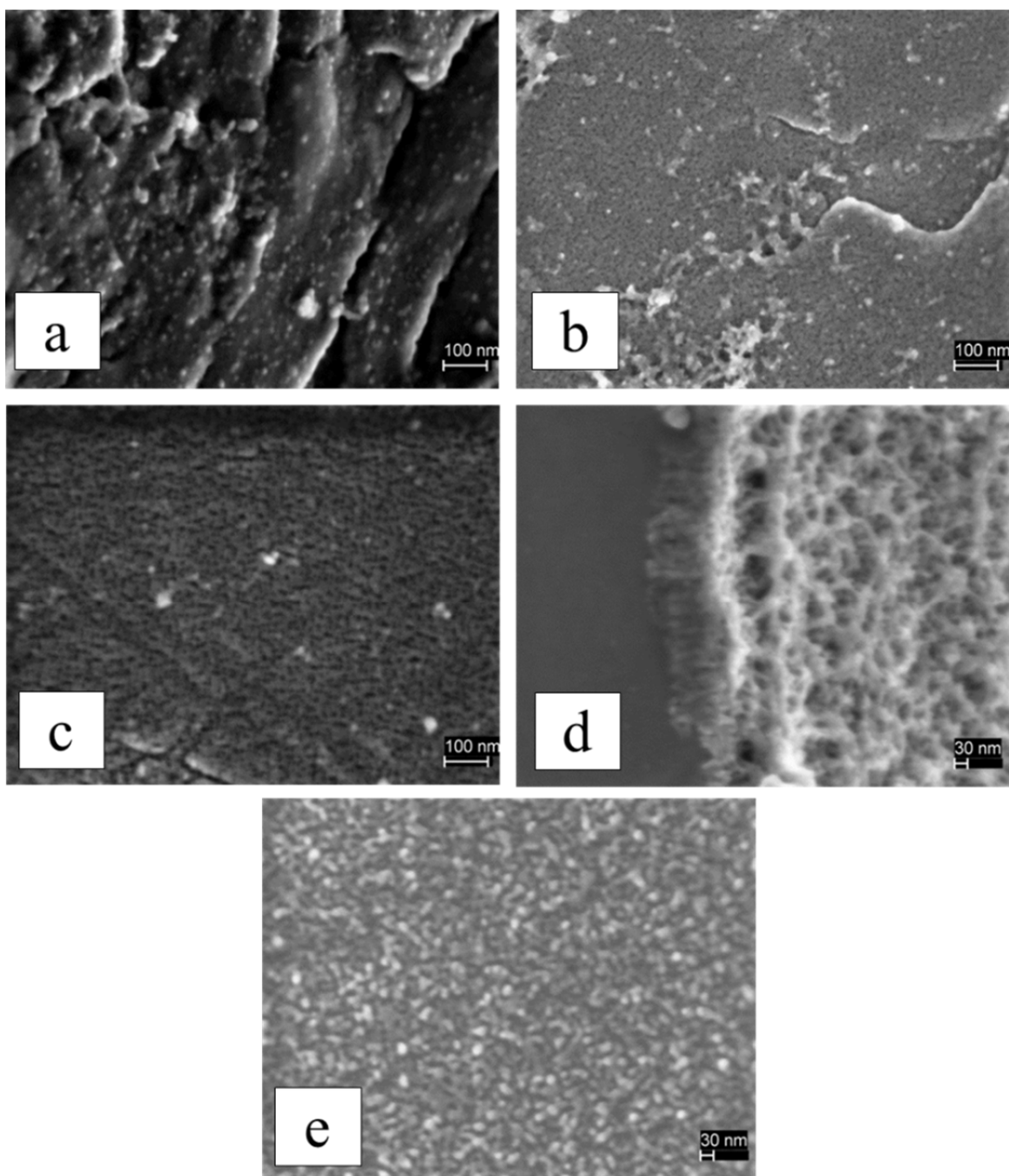


Although the 40-volt anodization potential yielded porous nanofilms for all considered treatment durations, rapid and catastrophic substrate degradation occurred. This was also evident to the naked eye in Figure 10(b). The overall results at 60 and 90 minutes force the conclusion that a 40-volt anodization technique renders a porous oxide film that is effectively useless for the desired applications. In Figure 12(a), the smallest pore diameter was measured at 15.63 nm. In Figure 12(b), the largest pore diameter measured was 113.9 nm. Due to the amount of disintegration observed on the tungsten substrate, the target anodization technique was changed by decreasing the voltage and time variables to improve the quality of the film.

#### **4. Anodization at 20 Volts**

This section will discuss the results found after 20-volt anodization. Anodized substrates were characterized with the SEM for anodizing durations of 5, 10, 15, 30, and 45 minutes. Figure 13 contains SEM images that were captured and used to characterize the morphology and nanofeatures (if any) of the  $\text{WO}_3$  film.

Figure 13. SEM Images of 20-volt anodized  $\text{WO}_3$  films at 5 minutes (a), 10 minutes (b), 15 minutes (c), 30 minutes (d), and 45 minutes (e) at high magnification.



**a.      *Duration 5 Minutes***

To the naked eye, the substrate changed to a yellowish color within the first minute of anodization. After 5 minutes, the anodized sample was removed and observed to have a purplish iridescent color after air drying. SEM images revealed no obvious nanofeatures on the oxide film.

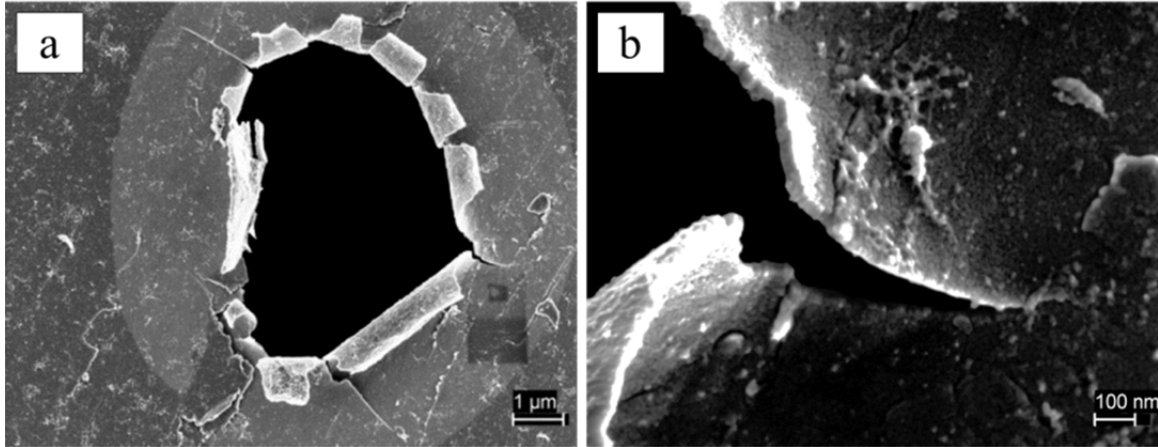
**b.      *Duration 10 Minutes***

Nanoscale porosity within the  $\text{WO}_3$  film became faintly apparent after 10 minutes of anodization. Small porous nanofeatures are visible and are generally found throughout the surface. Figure 14 was used to measure the apparent film thickness. Figure 14(a) depicts an anomolous feature that was occoasionally found in all regions of the anode. The authors propose this rupture was attributed to either a mechanism during anodization or due to preparation for SEM analysis. During anodization, trace amounts of a gaseous species formation was observed on the anode. Oxygen generated during the oxide dissolution may have adsorbed to the substrate, eventually forming  $\text{O}_2$  molecules beneath the oxide film causing a rupture during the evacuation of the SEM vacuum chamber. However, an alternate explanation points out that anodized substrates were rinsed with ethyl alcohol and then prepared for SEM analysis. The prepared samples were stored at 30”Hg vaccum overnight which may have caused trace amounts of ethyl alcohol trapped between the substrate and oxide film to vaporize and create the rupture. In either case, the anomaly proved to be a welcome occurrence as it provided a useful means to analyze the film thickness. In Figure 14(b) the porous film was measured to be 41 nm thick. The film cross-section is visible along the line of rupture and indicates a directional pore growth mechanism that occurs towards the substrate. The observed pores are not found uniformly in all regions of the oxide film, but preferentially at various locations scattered across the surface of the film.

As noted earlier, PVD sputtering was carried out for the 20-volt anodized specimens with the smallest apparent nanofeatures. The 10 min samples were sputtered to determine if a clearer image could be produced during SEM characterization. However,

the 2.6 nm sputter coating appeared to erase all evidence of nanoscale pores that were faintly apparent in the 10-minute sample.

Figure 14. SEM images of 20 volt, 10-minute anodic  $\text{WO}_3$  damage due to film rupture (a) but useful for measuring thickness (b).



**c. Duration 15 Minutes**

After 15 minutes of anodization, the existence of nanoscale pores was more prevalent and is obvious in Figure 13(c). Furthermore, they appear larger than those observed on the 10-minute specimen. However, just as in the 10-minute specimen, pores uniformly exist only within preferential regions of the oxide film rather than generally across the entire surface.

**d. Duration 30 Minutes**

In this specimen, there was an indication of separation between  $\text{WO}_3$  film and substrate in the regions with porosity, and the nanopores no longer appeared circular and symmetrical. While the nanoscale pores were found to have continued their growth, they appeared to be less structured as seen in Figure 13(d). The regions that were preferentially experiencing film dissolution (i.e., porous film formation) at shorter durations now seemed to indicate the onset of pitting. Figure 13(d) shows a highly porous unstructured film on the edge of one such pit. The cross-sectional structure of the film is



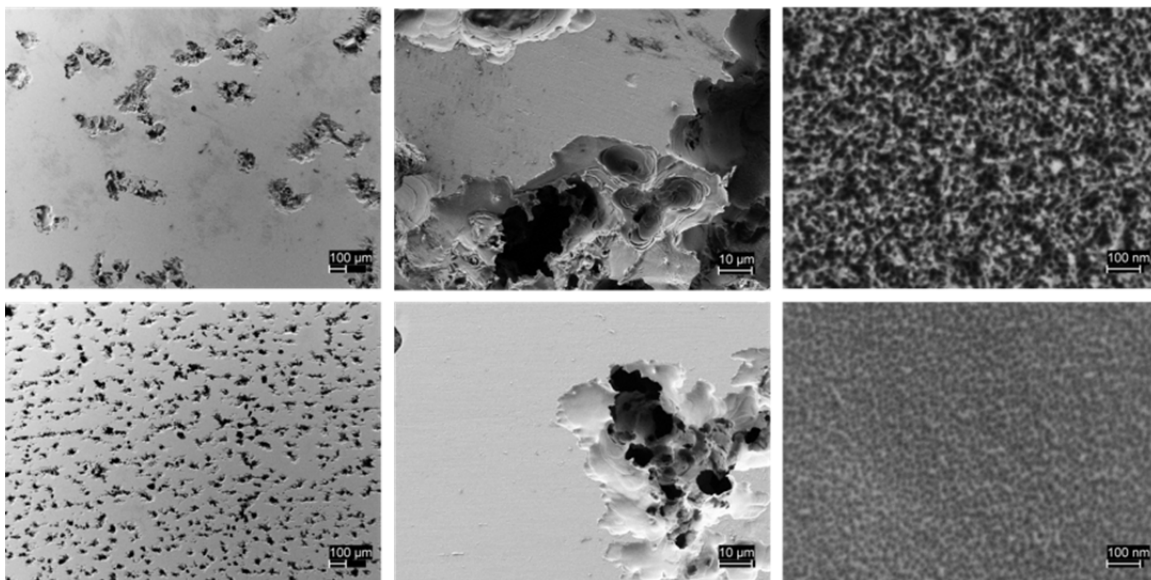
apparent and indicates a directional pore growth mechanism where pore size is increasing, perhaps caused by nanopores collapsing into one another.

*e. Duration 45 Minutes*

After 45 minutes of anodization, the oxide films have started to experience pitting with large areas of complete film dissolution. The edges of each pit continued to have a porous structure where separation between the  $\text{WO}_3$  film and substrate was observed. As the pitting progressed, an apparent advance of the oxide film dissolution seemed to grow out from each pit. Figure 13(e) shows the porosity that exists on the edge of the advancing dissolution front.

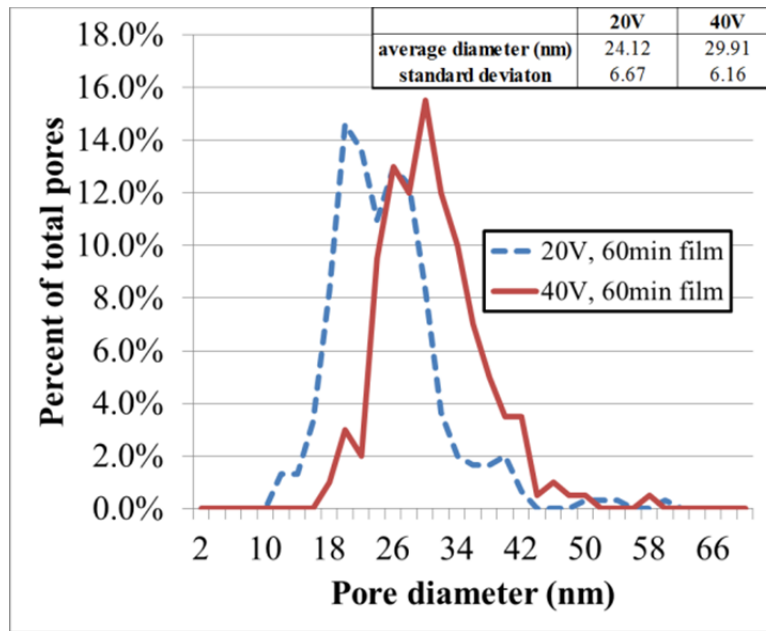
The SEM images captured in Figure 15 depict the 20 volt and 40 volt samples after 60 minutes of anodization. The lowest magnification images show the pitting that resulted from the preferential film dissolution that was noted in the 20 volt 15-minute specimen.

Figure 15. Secondary electron images showing a comparison of 20 volt (top) and 40 volt (bottom) anodic films after 1 hour at low (left), medium (middle), and high (right) magnification.



A pore size distribution was determined using the SEM images captured at 100,000 times magnification shown in Figure 15 and found that the 20 volt average pore diameter was 24.1 nm, while the 40 volt average pore diameter was 29.9 nm. The overall size distribution for the two different specimens is plotted in Figure 16. Again, it is worth mentioning the porous oxide films were not found uniformly across the entire surface but rather in areas directly adjacent to severe pitting or the onset of pitting.

Figure 16. Pore size distribution for 1 hour anodized specimens at 20 and 40 volts.



The trend in pore size and anodization potential is consistent with that expected from the literature, which found that higher anodic potential and subsequent current density results in a greater rate of dissolution of material [57], [58], [59]. This increase in voltage when combined with a greater amount of available fluoride ions in the electrolyte should increase the outward dissolution of pores. To be an ideal candidate for NTSDM capacitors, the desire is to establish conditions which create uniform pore growth upon the entire surface. By comparing the low magnification images in Figure 15, it is apparent that higher anodizing potential caused a larger number of preferential oxide dissolution and subsequent pitting locations. It also appears that subsequent porous film growth at

the lower anodizing potential propagated further from each pit than did the higher anodizing potential.

## **E. CONCLUSION**

The goal of this study was to examine the impact of anodization voltage and duration on the surface characteristics of tungsten foil using protocols similar to those used on aluminum and titanium. The intent was to develop a tungsten based structure useful as a dielectric material for NTSDM based capacitors. Specifically, the aim was to develop a simple anodization protocol for creating a densely packed hollow nanotube array on the tungsten foil similar to that generated on titanium (discussed in the next chapter). However, none of the protocols employed led to the formation of an array of hollow tungsten trioxide nanotubes. In all cases, the surface morphology consisted of a  $\text{WO}_3$  layer with observable nanoscale, irregularly oriented, and nonlinear pores where linear nanotubes normal to the foil surface was desired. The range of variables selected significantly impacted the uniformity and quality of this layer.

The resulting oxide films and degraded tungsten substrates were determined to be unsuitable for further capacitor experimentation. The success of the NTSDM model requires a uniform oxide film covering the entire metal substrate with no breaks in the oxide matrix integrity. As has been thoroughly discussed in the preceding sections, anodized tungsten is not an ideal candidate for NTSDM capacitors according to the assessed protocols of voltage, time, and electrolyte concentration. However, future research may find a viable candidate particularly by evaluating different electrolyte fluoride and water concentrations.

Ultimately, the course of electrochemical anodization and the associated results led to the conclusion that tungsten would not be a suitable substrate nor  $\text{WO}_3$  a suitable dielectric material. Although the study successfully tailored an anodization technique which apparently created a nanoporous oxide film, the integrity and uniformity of said film was determined to be insufficient for use in a NTSDM capacitor. Further research and experimentation was pursued using titanium.

### III. ANODIZATION OF TITANIUM

#### A. INTRODUCTION

Again, the first focus of this research is to achieve the creation of a nanostructured oxide matrix consisting of an ordered, tightly packed array of hollow, non-electrically conducting nanotubes normal to the substrate surface. It is believed this type of structure is the most appropriate foundational structure of dielectric material for high energy density NTSDM capacitors. This chapter outlines the modifications to and results from an existing electrochemical anodization technique specifically for titanium dioxide ( $\text{TiO}_2$ ). The techniques and results presented herein were found to be well-suited for NTSDM capacitor analysis and complimentary to earlier results achieved at NPS. A simple and inexpensive procedure is presented for the fabrication of nanostructured tubular  $\text{TiO}_2$  films.

It is generally understood that the growth of nanotubes on a metal surface during anodization requires a balance between the rate of oxide film dissolution at the metal/oxide interface and the rate of subsequent oxide growth. In this work, a relationship between these two processes presents itself by analyzing the trend in anodic current density. Though, not evaluated within the scope of this research, it is proposed that an empirical relationship may be mathematically derived by quantitative trend analysis of the anodic current densities for various anodization protocols.

The simple “rules of thumb” developed over the course of this research allowed anodization processes to be engineered to create the longest nanotubes in the shortest period of time. In general, the formula requires higher anodizing potentials ( $\geq 50$  volts) and higher fluoride concentrations ( $\geq 3.5$  wt%  $\text{NH}_4\text{F}$ ) but does not necessarily require longer anodizing durations (up to 4 hours). Protocols using shorter anodic potentials, lower fluoride concentrations, and lower potentials were initially used as benchmarks for targeted improvement.

## B. BACKGROUND ON THE TECHNIQUE

Sumio Iijima first published his discovery of carbon nanotubes over two decades ago [73]. Since that time, the continual discovery and development of nanoscale geometry stimulated the field of nanotechnology and produced breakthroughs in physics, chemistry, and materials science. The study of one-dimensional nanostructures found unique electronic properties like high electron mobility, very high specific surface areas, and great mechanical strength. Research in the fabrication and application of inorganic nanotubes is usually aimed at the enhancement of material-specific properties for environmental, biomedical, photochemical, or electrical applications [74–83].

Arguably,  $\text{TiO}_2$  is one of the most comprehensively studied transition metal oxides in the field of materials science. Some of the most unique functional features of bulk  $\text{TiO}_2$  are its ionic and electronic properties. Titania, in all of its crystal forms, is a wide bandgap semiconductor with suitable band edges that have warranted its use in solar cells and photocatalytic applications [84]. Accordingly, modern applications include not only photovoltaic cells, but also electrochromic systems and advanced coatings with highly desirable properties (e.g., anti-fogging, self-cleaning, or sensing). Most of the technologically advanced applications require high specific surface areas to achieve optimum performance. Hence, nanostructured forms  $\text{TiO}_2$  have been widely studied with particular attention on nanotubes due to better control of its physical and chemical behavior [85]. By shrinking dimensions to the nanoscale, unique electronic properties of  $\text{TiO}_2$  have emerged and are expected to drastically improve its interaction with the surrounding media [86]. This research, of course, aims to evaluate and optimize the suitability of  $\text{TiO}_2$  nanotubes as part of a viable, energy dense dielectric material.

Depending on the intended application, the process to fabricate reliable films of  $\text{TiO}_2$  nanotubes can be intensive and costly. While several methods have been studied, perhaps the most suitable and affordable method relies on the electrochemical oxidation reaction of titanium under select environmental conditions. Electrochemical anodization, as it is known, tends to reliably grow self-organized, highly structured layers of  $\text{TiO}_2$  nanotubes. Therefore, this technique was solely considered, given the intent of this

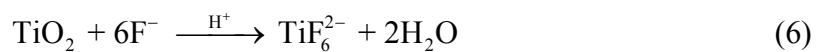
research is to develop and test a simplistic, repeatable procedure for creating effective dielectric films.

Anodizing methods for creating nanofeatured films on titanium substrates have been extensively studied under a variety of similar conditions [61], [87–94]. The varying methods differ in substrate thickness, surface preparation, electrolyte composition, electrolyte concentration, anodizing potential, and anodizing duration. Roy et al. [84] point out that degree of self-organization, tube length, diameter, crystal structure, and nanoscale morphology are together influenced by the parameters of anodization. Within the bounds of this study, anodized films of a self-organized, nanotubular morphology with varying tube lengths are primarily evaluated. Thus, a general anodization method was selected within which parameters were varied to ultimately document and record control over tube length.

Anodization is usually carried out by applying a constant voltage across an electrochemical cell. In all cases, the presence of fluoride ions in the anodizing electrolyte makes the difference between creating a compact oxide layer and growing a porous or tubular  $\text{TiO}_2$  film. The growth of the oxide can be monitored by recording the anodizing current over time. The absence of fluoride ions during anodization would create a compact oxide layer according to Equations (3) and (4).



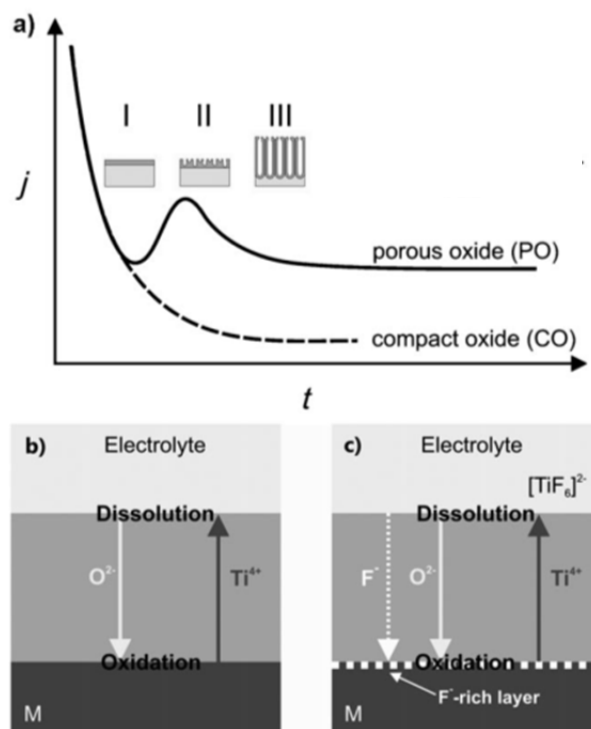
However, the oxide layer dissolves locally in the presence of fluoride ions, and a pore is created from small defects or depressions in the oxide layer [89]. These pits are created according to Equations (5) and (6) from the reactions between  $\text{TiO}_2$  and the disassociated anions of  $\text{NH}_4\text{F}$  (in the case that  $\text{NH}_4\text{F}$  is the electrolytic salt) [84].



Upon initiation of the anodizing procedure, the growth of the anodic layer is decided by ion transport of ions through the oxide and is driven by the field generated in the electrochemical cell. Depending on the rate of migration, the growth of newly formed  $\text{TiO}_2$  either occurs at the interface between titanium substrate and compact oxide or between the oxide and electrolyte. Under constant anodic voltage, the field strength decreases with increasing oxide film thickness. Thus, a drop in anodic current will occur until the film effectively stops growing except in the case where fluorides are present. If fluorides exist in concentrations suitable for nanotubular growth, then anodic current will start to increase. This trend indicates the creation of nanopores in the compact oxide layer that penetrate through to the titanium substrate and is due to the increase in the newly uncovered reactive areas on the substrate. Finally, the current will start to decrease and approach a lower steady-state current, though higher than steady-state current for fluoride-free anodization. The difference in the two steady-state currents implies that a higher field must exist across the tube bottom oxide layer, because that layer inhibits the migration of fluorides to facilitate continuing dissolution and tube growth.

The trend in anodic current directly represents the competition between oxide formation and oxide dissolution, or porous oxide formation, at the metal/oxide interface. Figure 17(a) is a comparison of the typical anodic current profiles with and without fluorides. The shape of the porous oxide curve is an empirical indication of the growth of an array of nearly identical nanotubes in an organized symmetry. Figure 17(b) is an estimation of the ionic transport without fluorides, while Figure 17(c) is that with fluorides.

Figure 17. Typical anodic current trend over time (a); drawing of field-aided ionic transport without fluorides (b); and drawing of field-aided ionic transport with fluorides (c).



From P. Roy, S. Berger and P. Schmuki. TiO<sub>2</sub> nanotubes: Synthesis and applications. *Angewandte Chemie International Edition* 50(13), pp. 2904–2939. 2011.

For extended anodization techniques (those with longer durations), nanotube growth and resulting morphologies can be determined by other kinetic effects within the electrolyte such as agitation, gravity, joule heating, and viscosity. The presence of fluorides throughout the anodizing solution will dissolve the tops of the nanotubes, though not as fast as at the tube bottoms where fluorides are expected to exist in higher concentrations due to field-aided migration. This effect is obvious in subsequent SEM imagery where shorter duration anodization techniques left remnants of the initially formed compact oxide layer, while longer techniques resulted in outer tube collapse resembling carpet or “grassing” as it has been described in one study [95].



## C. EXPERIMENTAL SETUP

### 1. Materials and Equipment

The experimental equipment used to anodize titanium was assembled together on a workstation and is pictured in Figure 18(a). Three transistorized power supplies (Power Designs, Inc. Model 4005), one of which is pictured in Figure 18(b), were wired in series in order to achieve higher anodization potentials. In order to continually monitor the potential across the electrochemical anodization cell, a digital voltmeter (Keithley 2400 Sourcemeter) was connected to the anode and cathode leads and is pictured in in Figure 18(c).

Figure 18. (a) Anodization workstation with DC voltage power supplies, digital voltmeter, digital ammeter with computer interface, and electrochemical cell; (b) one of three power supplies used as a DC voltage source to anodize titanium; and (c) Keithley 2400 Source Meter used to monitor applied anodization potential.



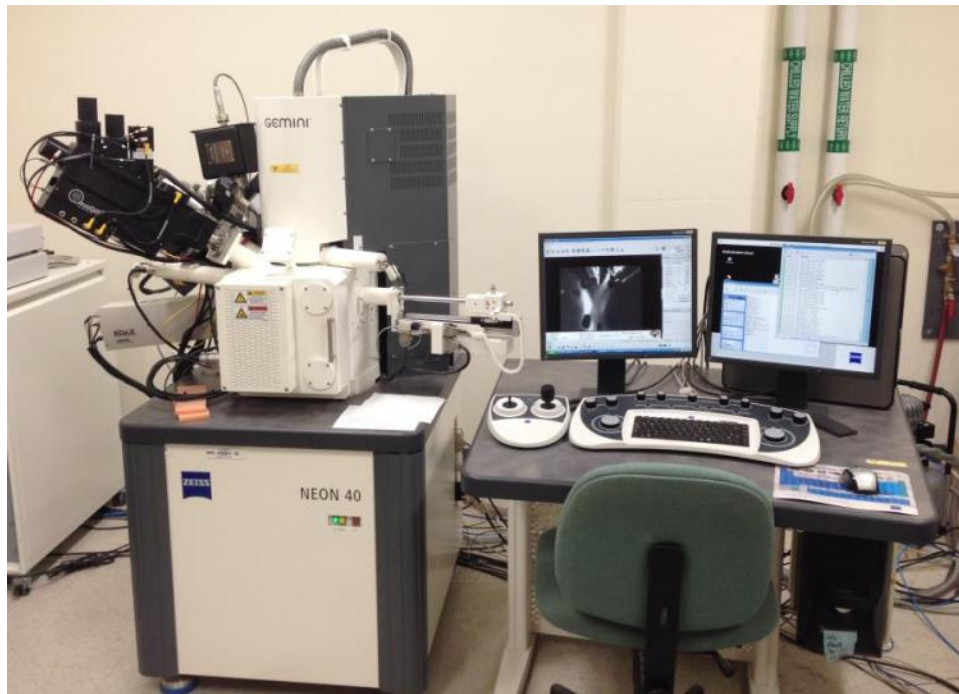
## 2. Characterization Techniques

Results of the titanium anodization procedures reviewed in the following sections utilized a number of characterization techniques. Because the resulting anodic films had a greater integrity and structure than those created during tungsten anodization, the titanium anodic films were better suited for additional characterization methods not discussed earlier.

### *a. Scanning Electron Microscopy (SEM) Analysis*

The dimensional measurement of each anodic film was conducted using the Zeiss SEM Neon 40 with 2 keV electron beam pictured in Figure 19. Activation of the  $\text{TiO}_2$  films was not a problem as was the case with  $\text{WO}_3$ . CVD sputtering was not necessary to achieve excellent quality SEM images as long as the films and/or titanium substrates were well attached to the SEM sample holders with carbon adhesive.

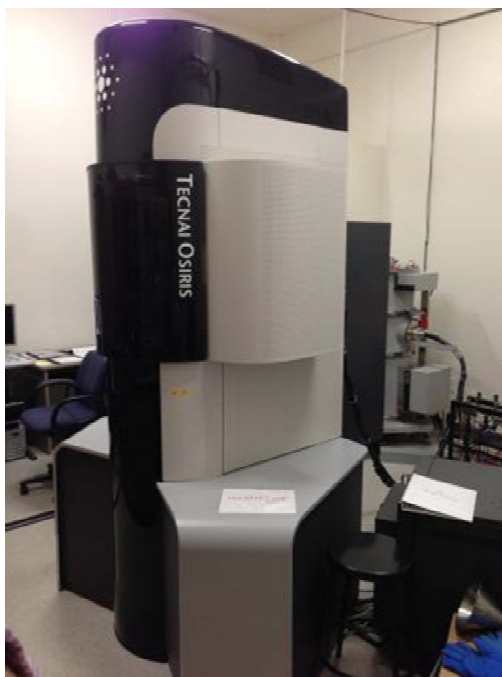
Figure 19. ZEISS Scanning Electron Microscope.



***b. Transmission Electron Microscopy (TEM) Analysis***

For select anodic films, the inner morphology of the nanotube matrices were analyzed dimensionally and compositionally using the FEI Tecnai Osiris TEM beam pictured in Figure 19. TEM analysis was particularly useful in capturing the morphology within the TiO<sub>2</sub> nanotubes as well as determining phase and composition of the anodic films.

Figure 20. FEI Transmission Electron Microscope



***c. X-ray Diffraction (XRD) Analysis***

Qualitative and quantitative crystallographic analysis of a single TiO<sub>2</sub> film was conducted using the Rigaku MiniFlex 600 X-ray diffractometer seen in Figure 21.

Figure 21. Rigaku MiniFlex 600 benchtop X-ray diffractometer.



*d. Anodic Current Density*

For medium and thick film anodization techniques, anodic current density was recorded and analyzed as a supplementary characterization technique to the anodization results. Pictured in Figure 22, a digital multimeter (UNIT-T UT71B True RMS Multimeter) with computer interface was used to monitor and record anodizing current during anodization to verify each experiment was proceeding as desired.

Figure 22. UNIT-T UT71B True RMS Multimeter with computer interface was used to monitor and record anodizing current.



The recorded data was normalized by dividing the current by the immersed anode surface areas and are reported herein as current densities with units of mA/cm<sup>2</sup>. Two advantages were gained by monitoring *in-situ* currents. First, the real-time current densities provided early indications of abnormalities during anodization protocols. In one case, for example, abnormally high and rapidly increasing current was observed prior to the onset of rapid and excessive anode and oxide film dissolution. This association was noted, and in the future, can be an early indication that an immediate change in protocol is required to prevent film damage. Second, a general correlation can be derived for each combination of anodic potential and duration according to the recorded magnitudes and overall trend in current density. Such information can be used as an indicator of resulting film thickness without reliance on the expensive and time consuming SEM characterization.

#### **D. EXPERIMENTAL METHOD AND ANALYSIS**

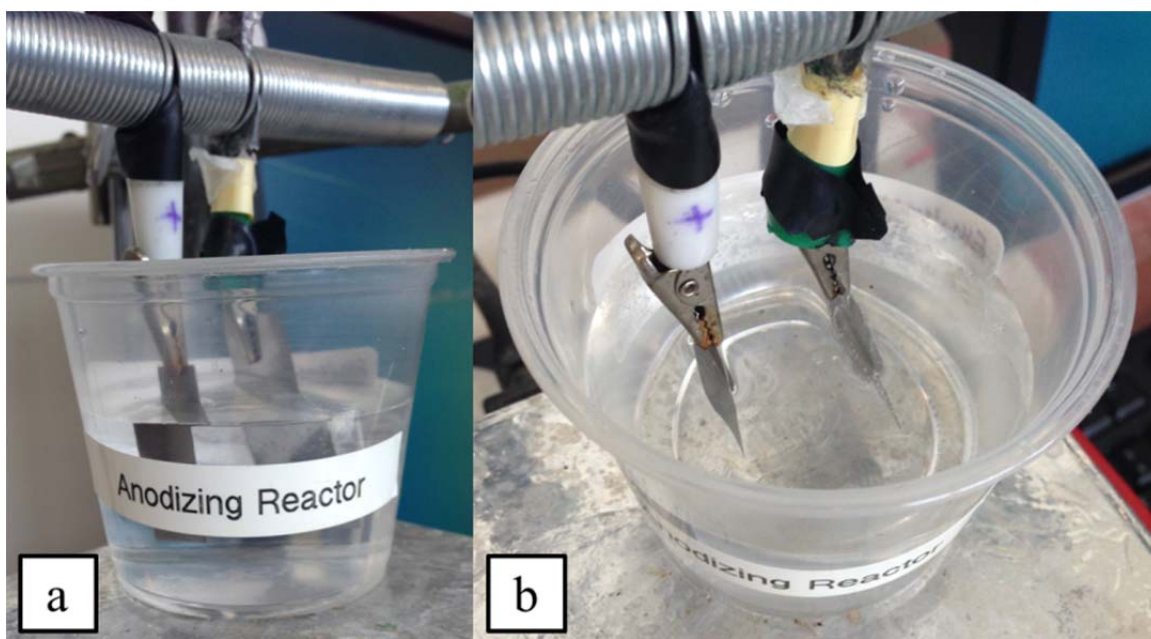
All experimental procedures were carried out with commercially available chemicals and materials of the highest available purity. Deionized water (DIW) was used to prepare all electrolyte solutions. Nanostructured TiO<sub>2</sub> films were created by anodizing 0.05 mm thick, 99.6% pure titanium foils (Gallium Source). TiO<sub>2</sub> films were grown by anodization in an electrolyte solution containing 0.25 wt% to 0.6 wt% NH<sub>4</sub>F (Aldrich) and 2.75 wt% to 3.5 wt% DIW in 80 mL of ethylene glycol (Aldrich). The resulting electrolyte concentrations were varied and controlled according to the desired nanotube length. In one particular study [93], it was determined that longer films required higher NH<sub>4</sub>F and DIW concentrations along with higher anodic potentials. Therefore, the design of experiments was organized according to anodic potential and fluoride concentration where a wider range of voltages was evaluated at higher fluoride levels and is outlined in Table 5.

Table 5. Design of experiments for Titanium Anodization

Anodic Potential (volts)	LOW FLUORIDE 0.25 wt% NH <sub>4</sub> F 2.75 wt% DIW			HIGH FLUORIDE 0.6 wt% NH <sub>4</sub> F 3.50 wt% DIW		
	Time (hours)	Surface Preparation	Electrolyte Reused	Time (hours)	Surface Preparation	Electrolyte Reused
40	1	metal polish, alcohol rinse	yes	----	----	----
40	2	ethyl alcohol rinse	no	----	----	----
40	4	metal polish, alcohol rinse	yes	----	----	----
40	4	ethyl alcohol rinse	no	----	----	----
40	----	----	----	4	ethyl alcohol rinse	no
45	----	----	----	4	ethyl alcohol rinse	yes
50	----	----	----	4	ethyl alcohol rinse	yes
60	----	----	----	4	ethyl alcohol rinse	yes

The combination of applied voltage, anodization time, and electrolyte concentrations dictated the morphology of the TiO<sub>2</sub> anodic film. However, the object of the design of experiments was to predictably control anodic film thicknesses and the associated nanotube lengths. The anodization was performed in a two-electrode electrochemical cell using a 0.05mm thick, 99.6% pure titanium cathode (Gallium Source) measuring 1.6 cm wide and 3.5 cm tall. This setup is a departure from most procedures from the literature which require a platinum cathode. Figure 23 is a picture of the electrochemical cell and is the same setup used in tungsten anodization with one exception. The titanium substrates were cut to 1.0 cm wide by 3.0 cm tall, thoroughly rinsed with ethyl alcohol, dried in air, and suspended within the electrolyte parallel to the cathode with 2 cm of separation.

Figure 23. Side view (a) and top view (b) of the electrochemical anodization cell with anode and cathode immersed in prepared electrolyte.



In some cases, the surface preparation was augmented by the use of a fine grit alumina electrode polish (SuperPol) in order to determine effects on the resulting film, if any. Just as in the case of tungsten anodization, varied procedures exist in the literature, many of which require more intensive pretreatments or surface preparation techniques such as ultrasonication or electrochemical polishing. However, as stated earlier in the motivation for this study, the object of this research is a simplified, easily repeatable procedure with reliable results.

The height of the bed plate was adjusted to ensure only 2 cm of the anode was immersed within the electrolyte. The effective anodic surface area used to calculate current density was  $5 \text{ cm}^2$  which included both sides of the anode. Upon completion, a thorough but gentle DIW rinse and air-dry method was found to be sufficient for the

anodize foils with thin and medium thicknesses. The thicker films required a more controlled drying method to prevent film damage and separation or exfoliation from the titanium foil substrate. Complications associated with drying the thick films will be discussed later in this chapter.

### **1. Thin Films (thickness $\leq 6\mu\text{m}$ )**

The first attempt at anodizing titanium started by attempting to grow short films based on a protocol developed during earlier work at NPS [2]. The first protocol evaluated the effect of anodization time at a low fluoride concentration (0.25 wt%  $\text{NH}_4\text{F}$ , 2.75 wt% DIW) on tube length and final morphology. Two specimens were anodized at 40 volts: one for 2 hours and another for 1 hour. The 1-hour anodized sample was further evaluated using secondary protocol to determine the effect of reusing the anodization electrolyte. The anodes for each experiment were metal polished and rinsed with ethyl alcohol.

#### ***a. Protocol: 40 Volt, 2 Hours, Low Fluoride***

SEM analysis confirmed the formation of an oxide film with the morphology of a highly structured nanotube matrix. Using SEM imagery analysis, the resulting film was measured between 5.5  $\mu\text{m}$  and 6.5  $\mu\text{m}$  thick and is thus characterized by 6 $\mu\text{m}$  long nanotubes. Figure 24 and Figure 25 clearly capture the tube-like makeup of the oxide matrix. Also apparent on the left side of Figure 24 is the closed morphology of the nanotube bottoms which normally remain adhered to the titanium substrate but were detached specifically for SEM analysis.



Figure 24. SEM image capturing a cross-sectional view of the nanotube matrix with closed bottom ends apparent on the left.

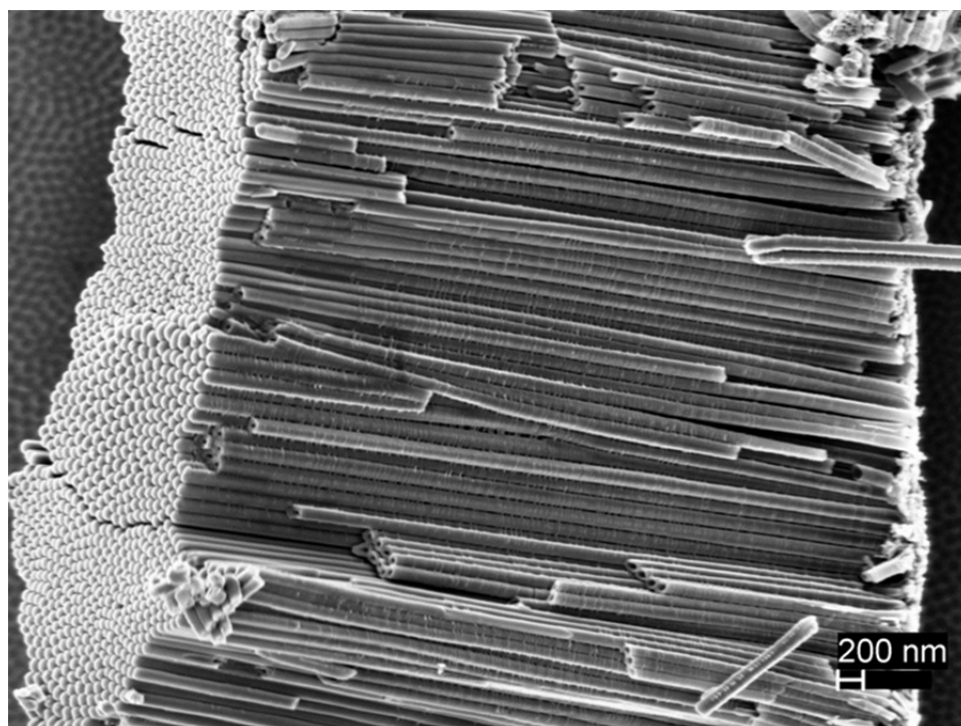
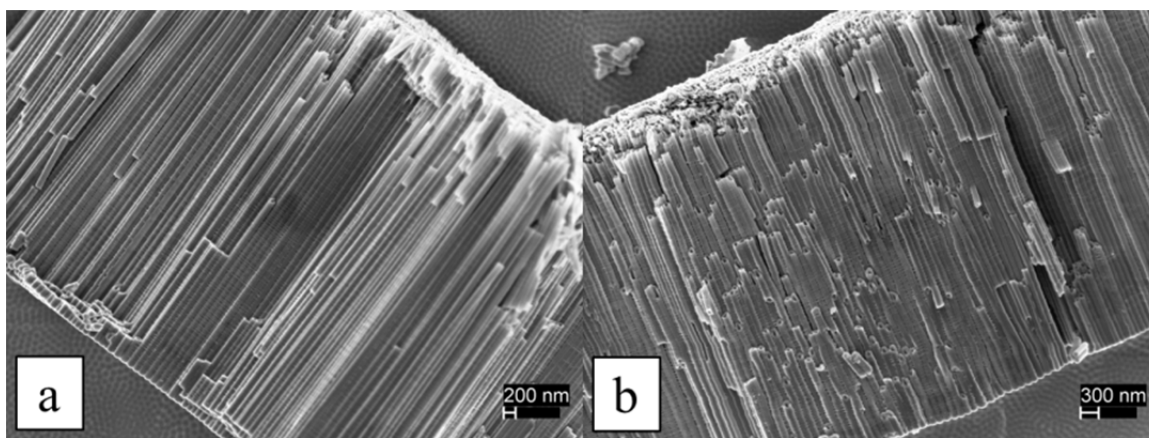
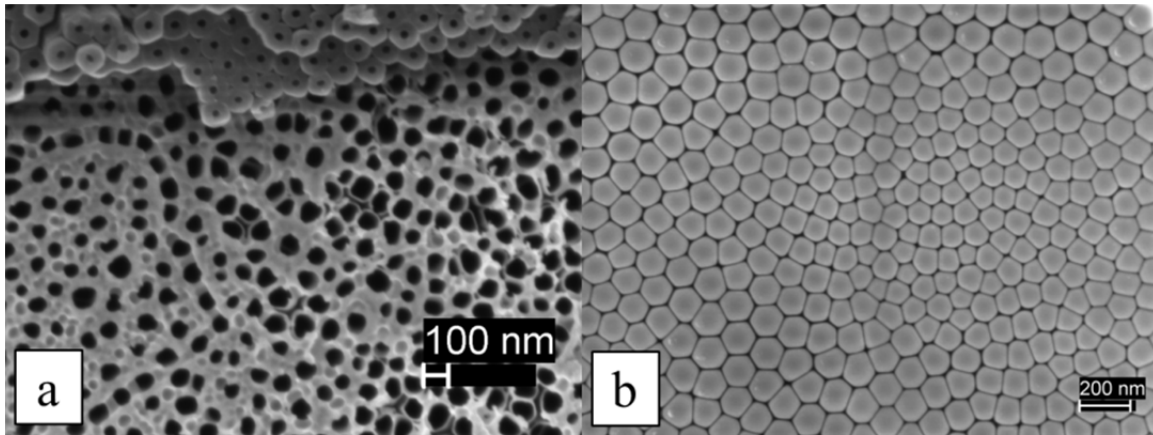


Figure 25. SEM images of the well-formed, self-organized 6  $\mu\text{m}$  nanotubes produced using 40 volts for 2 hours.



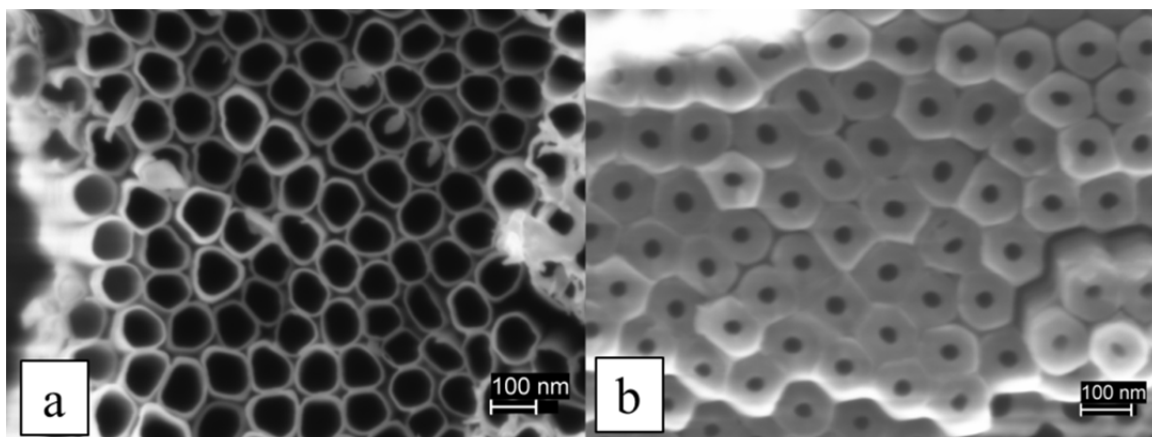
SEM imagery also helped to characterize the morphology of the film and the individual tubes within. As is apparent in Figure 26(a), the outer surface of each film appears to be the remnant of the initially formed compact oxide layer from which pore initiation and subsequent tube formation began. The visible openings in this layer are the mouths of each  $\text{TiO}_2$  nanotube within the matrix. Figure 26(b) captures the morphology of the base of each tube. Without the mechanical disturbance required for SEM sample preparation and analysis, the oxide films remain attached to the titanium foil substrate via the interface oxide layer.

Figure 26. SEM images of the open tops of the nanotubes at the film surface (a) and the closed nanotube bottoms at the film and substrate interface.



As is pointed out in the literature [84], the tube profile does not have a uniform inner diameter from the top of the tube all the way to the bottom. Nearer the base, the inner diameter decreases. Pictured in Figure 27, the average outer diameter was measured at 94 nm, while the average wall thickness was measured at 4 nm nearest the top and 42 nm nearest the bottom. TEM imagery was used to further investigate this unique morphology in a specimen discussed later.

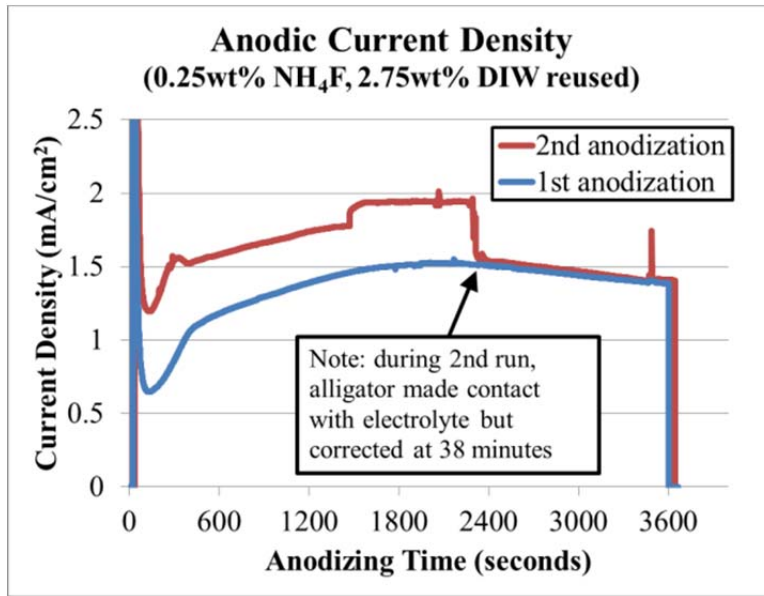
Figure 27. SEM images that capture variation in the nanotube inner diameter from just below the open top (a) down to the closed base (b)



***b. Protocol: 40 Volt, 1 Hour, Low Fluoride***

Anodizing currents were monitored for this experimental regimen (and all others discussed hereon). In-situ monitoring allowed early identification of unexpected problems and provided indication that anodization was proceeding as expected according to the current trends reported by Roy et al. [84]. One such case occurred during this procedure and is apparent in Figure 28. During the second anodization attempt, at approximately 38 minutes, the alligator clip suspending the anode in the electrochemical cell was discovered to be in contact with the electrolyte at which point the height was corrected. Immediately, current dropped to a level expected from the first anodization. After analyzing the plotted current density, it is believed that the alligator clip likely made contact with the electrolyte at 25 minutes (1500 seconds) where a sharp step up in current occurred.

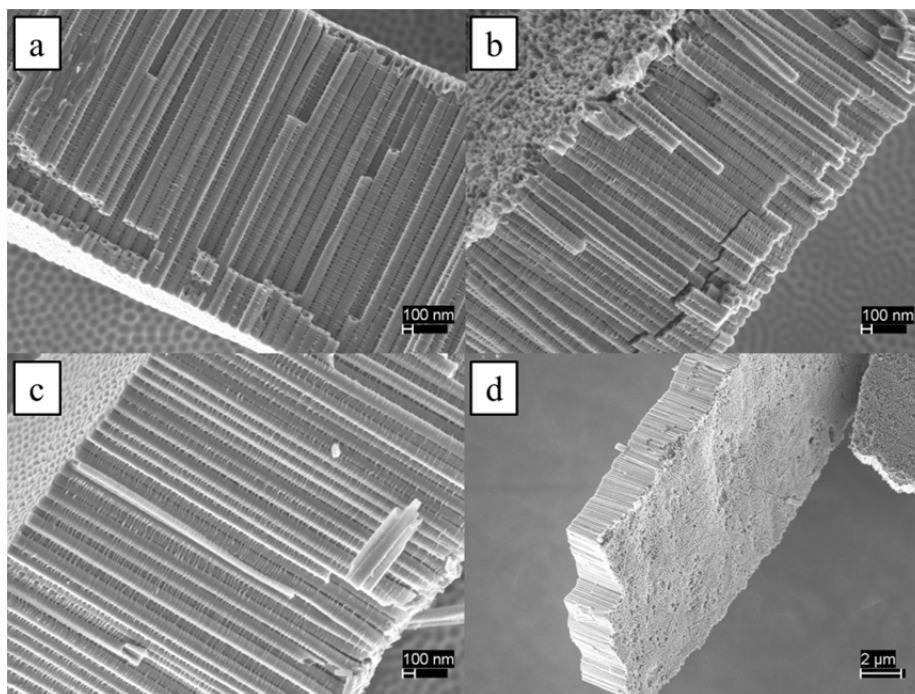
Figure 28. Comparison of anodic current densities for 40 volt, 1-hour protocols during electrolyte initial use (1<sup>st</sup> anodization) and reuse (2<sup>nd</sup> anodization).



The first anodization current density followed the general trend expected with a local maximum value (approximately 1.5 mA/cm<sup>2</sup>) occurring after approximately 30 minutes. As slope of the current changed from positive to negative, this was perceived as the point at which oxide dissolution (rate of tube growth) was at a maximum. Also, because the protocol lasted only 1 hour, it was expected that remnants of the compact oxide layer would be obvious with little or no thinning of the mouths of the tubes prevalent. Subsequent SEM analysis proved as such.

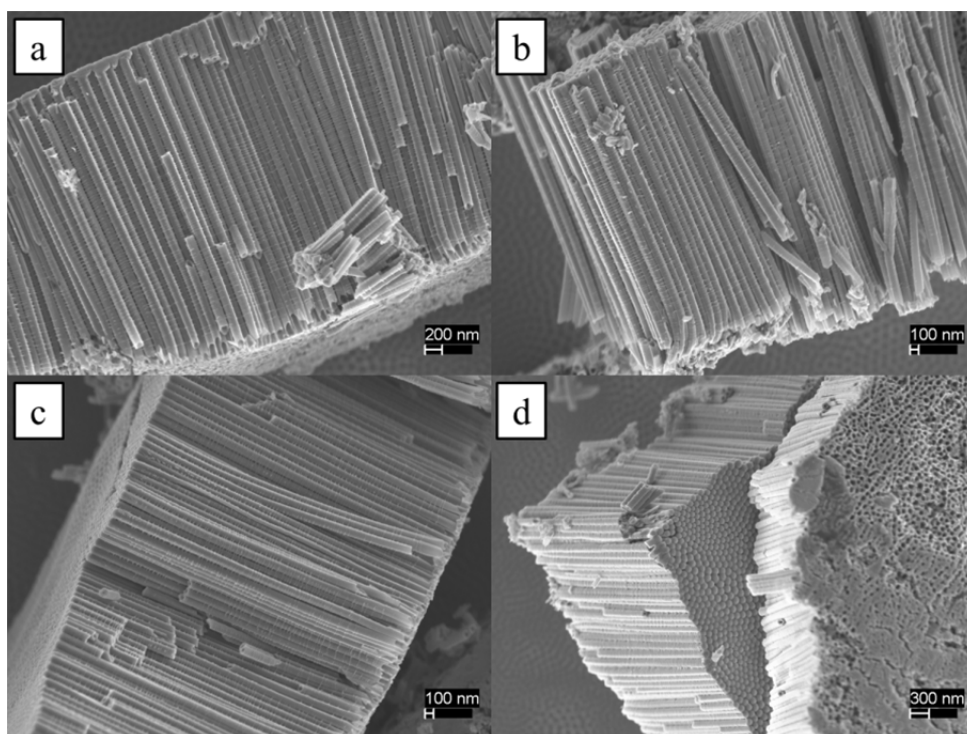
Figure 29 shows a nanotubular oxide film with 3.0  $\mu\text{m}$  average thickness. Tube diameter and structure is nearly identical to that of the 2-hour anodization. The resulting lengths also indicated that, at least for these shorter duration anodization techniques, there is a linear relationship between time and tube length. The 2-hour anodization produced a 6  $\mu\text{m}$  film while the 1-hour technique produced a 3  $\mu\text{m}$  film. Though, given the analysis and explanation provided by Roy et al. [84], this relationship is not expected for longer anodization protocols where tube growth slows as a function of increasing film thickness.

Figure 29. SEM images of 40 volt, 1-hour anodic film comprised of self-organized 3  $\mu\text{m}$  nanotubes (a), well-formed tube tops (b), closed bottom ends (c), and general film morphology at a lower magnification (d).



A secondary experimental protocol was developed in-situ to determine how, if at all, reusing the same electrolyte for a second anodization would influence the subsequent film thickness. As discussed earlier, an anomaly occurred after the alligator clip made contact with the electrolyte. However, the current leading up to that point was nearly 30% higher than that recorded during initial anodization. This result suggested that a thicker film (longer nanotubes) may have been grown. In fact, subsequent SEM analysis indicated a 3.8  $\mu\text{m}$  anodic film was formed with much of the same characteristics as the film produced during the first anodization. SEM images for the second anodization at 40 volts and 1 hour are presented in Figure 30.

Figure 30. SEM images of 40 volt, 1-hour (electrolyte reused) anodic film comprised of 3.8  $\mu\text{m}$  nanotubes (a–c) and closed tube bottoms and open tube tops at the surface (d).



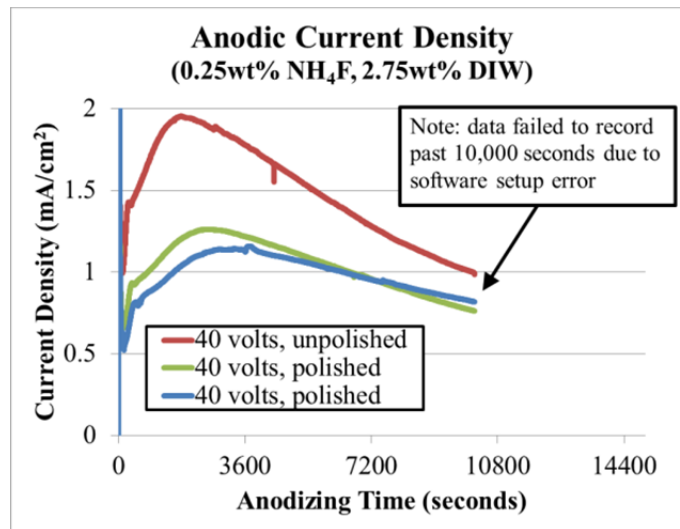
## 2. Medium Films ( $6\ \mu\text{m} < \text{thickness} < 17\ \mu\text{m}$ )

A second general protocol was developed to evaluate the effect of longer anodization times at a low fluoride concentration (0.25 wt%  $\text{NH}_4\text{F}$ , 2.75 wt% DIW). Based on the plotted anodization currents from the 1-hour anodization technique, currents were expected to peak at approximately 30 minutes with values around  $1.5\ \text{mA}/\text{cm}^2$ . Also, the 2-hour anodization technique produced  $6.0\ \mu\text{m}$  films presumably well past the point of maximum growth rate at 30 minutes. Therefore, a 4-hour anodization time was selected in order to determine how much longer the tubes would grow past  $6\ \mu\text{m}$ . Modifications of the second general protocol were employed to determine the effects on resulting film thicknesses: the effect of metal polishing the substrates rather than just rinsing with ethyl alcohol prior to anodization, and the effect of reusing the electrolyte after such long anodization durations.

**a. Protocol: 40 Volt, 4 Hour, Low Fluoride, Electrode Polishing**

In theory, metal polishing prior to anodization likely removed a portion or most of the nanometer scale oxide layer that is assumed to exist on the as-received foil specimens, though, the existence of such a film was not verified during the course of this study. It is proposed that the removal of this film, which is the precursor to the interface layer, causes an inhibition of tube growth from the onset of anodization, and ultimately produces a thinner film. That is, the initial seconds or minutes of anodization do not immediately result in the formation of pores that eventually become tubes. Rather, the initial period of anodization on a polished film is spent “re-growing” the compact oxide layer. Such a mechanism may be apparent in sharper, lower initial drops in current density, but was not validated by halting the anodization technique in the early stages for SEM analysis. However, as is apparent in Figure 31, the unpolished protocol resulted in higher anodic current density overall which was an early indication of a thicker film.

Figure 31. Comparison of anodic current densities for 40 volt, 4-hour protocols polished and unpolished.

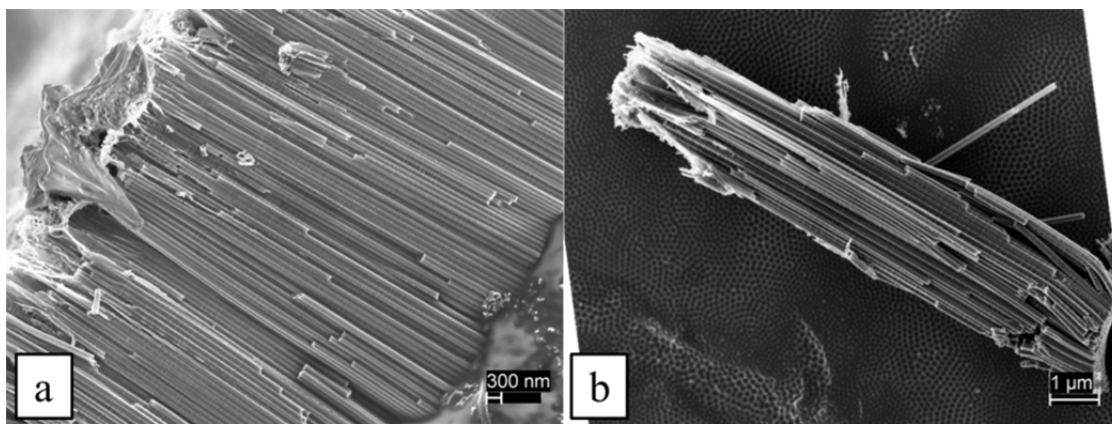


SEM analysis confirmed metal polishing the titanium foil substrate prior to anodization reduced the overall film thickness by up to  $3\text{ }\mu\text{m}$  when anodizing at the 40 volt, low fluoride protocol for 4 hours. The resulting film thickness for the specimen polished before anodization (green line from Figure 31) was approximately  $8\text{ }\mu\text{m}$  by

SEM analysis and is pictured in Figure 32(a). The resulting film thickness for the specimen anodized without polishing (red line from Figure 31) was approximately 11  $\mu\text{m}$  by SEM analysis and is pictured in Figure 32(b).

Of note, there were no differences in protocol between the two polished specimens (green and blue lines in Figure 31), but a slight difference in current density was recorded. The samples with the lower currents were verified by SEM analysis to both have 8  $\mu\text{m}$  films while the sample with higher current was measured at 11  $\mu\text{m}$ . If the object is to grow thicker films more reliably, then metal polishing should be abandoned from the outset. This correlation was not immediately identified and therefore metal polishing was used in the later anodization protocols even as the study attempted to grow thicker films.

Figure 32. SEM images of the 40 volt, 4-hour anodic films comparing the 8  $\mu\text{m}$  nanotubes of the polished sample (a) alongside the 11  $\mu\text{m}$  nanotubes of the unpolished sample (b).



Once more, other attributes besides tube length were noted but not analyzed further within the context of this study. Figures 33 and 34 are presented as a comparison of the tube profiles and surface morphologies of the polished and unpolished samples, respectively. Both images indicate the diminished presence of the initial compact oxide layer on the film surface, certainly more diminished than what was observed in the short duration anodization techniques. Figure 34(a) and (b) captures the thinning tube walls nearest to the surface of the anodic film.



Figure 33. SEM images of anodic film produced at 40 volts, 4 hours on a polished substrate that capture nanotube openings at the surface (a), tube wall thickness below the surface (b), and wall thickness closer to the closed bottom ends (c, d).

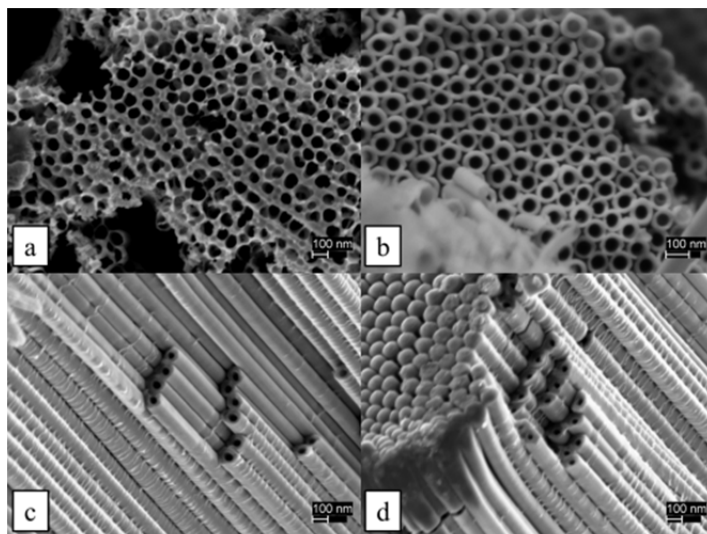
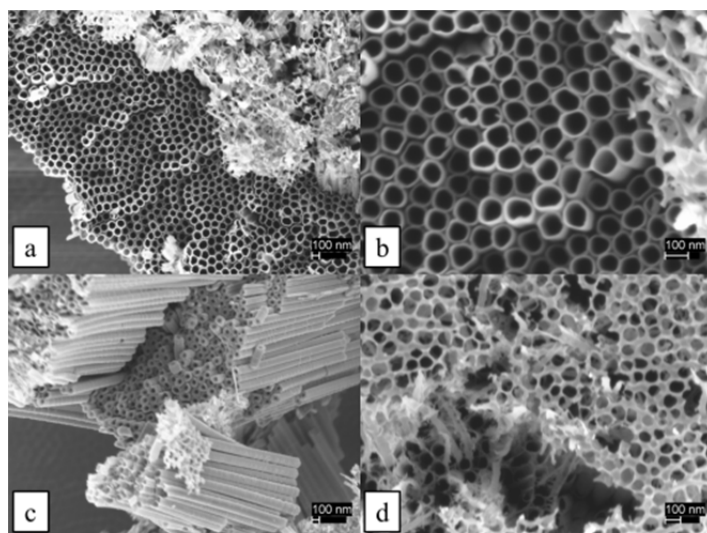


Figure 34. SEM images of anodic film produced at 40 volts, 4 hours on an unpolished substrate that capture nanotube wall thickness below the surface (a), same image at higher magnification (b), intermediate tube wall thickness (c), and general surface morphology (d).



***b. Protocol: 40 Volt, 4 Hour, Low Fluoride, Electrolyte Reuse***

The next protocol variation was designed to determine the impact, if any, of reusing the same electrolyte for a second anodization. According to Paulose et al. [93],

the recycled electrolyte is expected to have a lower concentrations of the  $H^+$  and  $F^-$  species in solution and therefore slower dissolution rates as well as new oxide growth at the tube bottoms. However, their study evaluated the reuse of electrolytes after extremely long duration anodization techniques (4 to 9 days) that produced nanotube films from 360  $\mu m$  to 1000  $\mu m$  in thickness. Given that this study is aiming to grow much thinner films over a much shorter duration, a similar effect may not be observed.

As is depicted in Figure 35, there was not a significant difference in current density trend and peak values over the entire duration of anodization. Subsequent SEM analysis confirmed no discernible difference in tube length between the first and second anodization procedures using the same electrolyte. Both films were measured to be, on average, 8  $\mu m$  thick, and as is apparent in Figure 36 and Figure 37, no change in surface morphology was noted. Both films still showed remnants of the compact oxide layer at their surface. Thus, it was determined that reusing the low fluoride electrolyte for durations of 4 hours or less does not change the resulting anodic film morphology and, more specifically, nanotube length.

Figure 35. Comparison of anodic current densities between new electrolyte and reused electrolyte for the same 40 volt, 4-hour protocol.

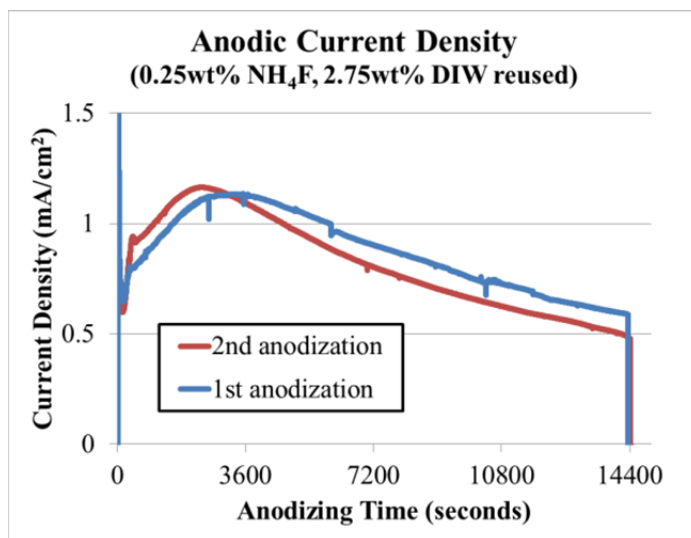


Figure 36. SEM images of anodic film produced at 40 volts, 4 hours (first use) with 8  $\mu\text{m}$  nanotubes (a, b), closed bottom ends (c), and familiar surface morphology (d).

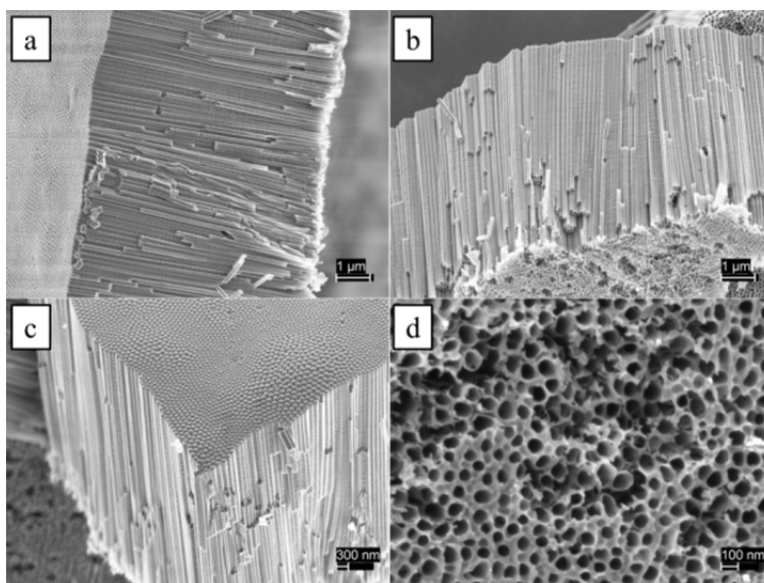
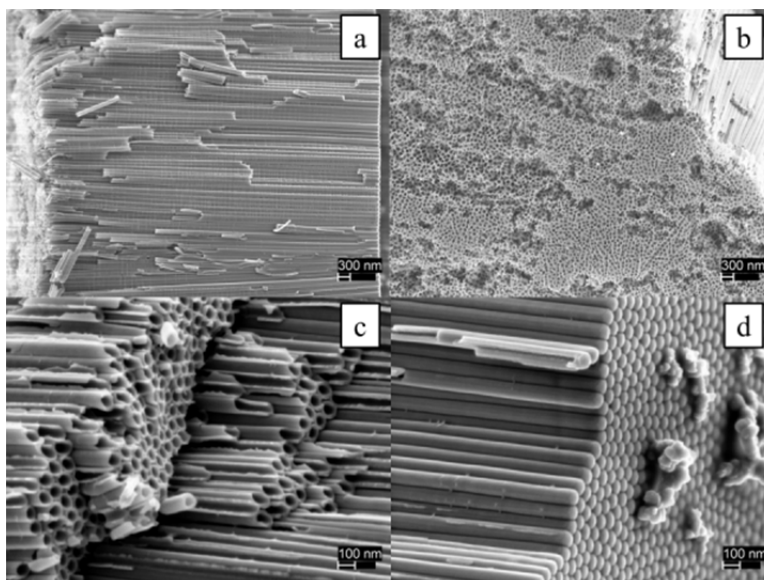
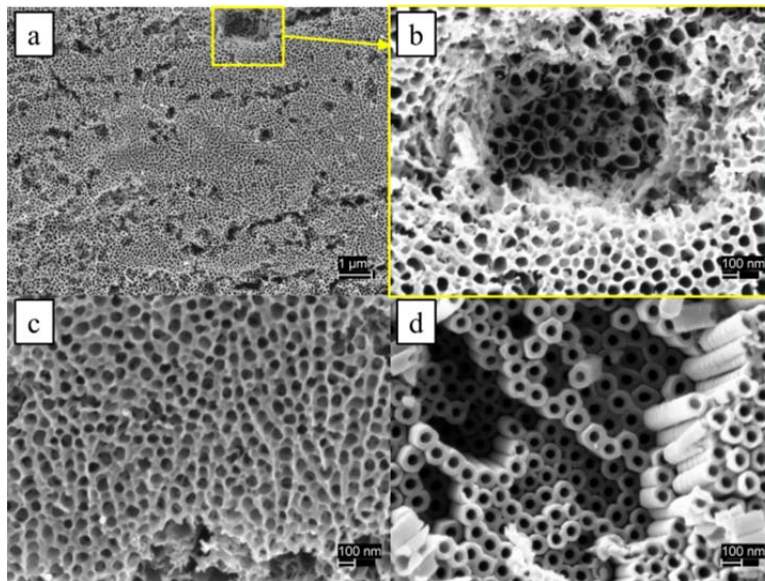


Figure 37. SEM images of anodic film produced at 40 volts, 4 hours (second use) with 8  $\mu\text{m}$  nanotubes (a), open nanotube tops (b), characteristic tube wall thickness at mid-length (c), and closed bottom ends (d).



Because the anodized foils were subsequently used to assemble NTSDM capacitors, a question arose regarding the quality and morphology of the anodic film on both sides of the anode. Previously cited studies made no distinction between characterizations of anodic films grown on either the engaged side (facing the cathode) or the disengaged side (facing away from the cathode). SEM samples from both sides of the anode were prepared from the anodic films produced while reusing the low fluoride electrolyte at 40 volts, 4 hours. Figure 37 contains images from the engaged side, and Figure 38 contains images from the disengaged side. Comparison of the anodic films confirmed that nanotubes measured 8  $\mu\text{m}$ , on average, regardless of anode side. Furthermore, surface morphology on the disengaged side of anode closely resembled the morphology on the engaged side. Thus, either side of the anode was found suitable for capacitor assembly, and only one side required SEM analysis to determine nanotube length.

Figure 38. SEM images of anodic film produced at 40 volts, 4 hours (second use) from the disengaged side of the anode depicting open nanotube tops (a–c) and mid-length wall thickness (d).



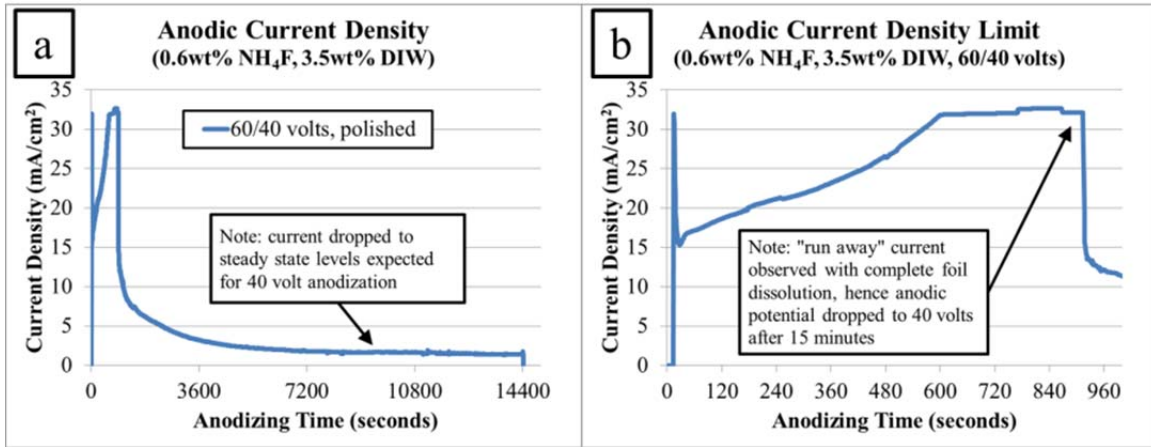
### 3. Thick Films (thickness $\geq 17\mu\text{m}$ )

The growth of longer nanotubes in organic electrolytes containing fluorides presents a challenge in optimizing the anodic potential, electrolyte concentrations and duration of anodization. Some studies cited in the development of this research [87], [93] present general guidelines for growing longer tubes with wide ranges of voltage, concentration and time. In most cases, the need for higher applied voltages ( $> 60$  volts) to grow thicker films during anodization is well documented. Similarly, higher concentrations of water and fluorides in the electrolyte were needed to sustain more anodic dissolution of  $\text{TiO}_2$  at the interface layer in concert with higher  $\text{TiO}_2$  nanotube growth rates. Hence, the protocols designed for thick films incorporated anodization potentials up to 60 volts and nearly triple the concentration of fluorides from previous anodization protocols. The same “high fluoride” electrolyte concentration (0.6 wt%  $\text{NH}_4\text{F}$  and 3.5 wt% DIW in 80 mL of ethylene glycol) was selected for every thick film protocol.

#### *a. Protocol: 60 Volt, 4 Hour, High Fluoride*

Using guidance from the literature [87], [93], the first thick film protocol was designed as a 60 volt, 4-hour procedure. However, unlike previous titanium anodization procedures, the anodic current density plotted in Figure 39 climbed continually over the first 10 minutes to levels not witnessed before. Such a trend was later recognized as early indication of rampant oxide film dissolution at a rate faster than  $\text{TiO}_2$  tube formation. This “runaway” current trend was observed earlier in the 40-volt anodization of tungsten which resulted in substrate dissolution. At approximately 11 minutes into the procedure, it was discovered that the power supplies had reached the maximum achievable current supply and were unable to maintain a constant 60-volt supply and is the cause of the current leveling in Figure 39(b). Simultaneously, the titanium foil anode started dissolving along one of the vertical edges.

Figure 39. Recorded anodic current density for first thick film anodization technique using 60-volt protocol (60 volts for 15 minutes, 40 volts for another 3.75 hours).



The apparent dissolution of both the newly formed oxide film and the titanium substrate along its edge, pictured in Figure 40, prompted an in-situ protocol change. The anodizing potential was dropped from 60 to 40 volts, which halted the anode dissolution. By the 2-hour point, anodic current density appeared to approach steady state levels previously observed at the 40-volt protocols and is pictured in Figure 39(a). Based on this observation, it was expected that any potential for film growth beyond previous 40-volt results would have occurred during the initial 15 minutes at 60 volts potential.

After anodization was complete and the sample was rinsed and dried, the naked eye appearance of the film's color and texture seemed to indicate significant variation in consistency. Two sections of the anode were removed for SEM analysis as seen in Figure 40. Also obvious is the substrate and oxide film dissolution along the right edge that occurred within the first 15 minutes.

Figure 40. Anodized titanium after 60 volt, 4-hour protocol with arrows distinguishing SEM sample cuts from the substrate dissolution (right edge).



The subsequent SEM analysis confirmed the existence of an oxide film with thickness measuring between 13  $\mu\text{m}$  and 18  $\mu\text{m}$ . The associated nanotubes were the longest in this study thus far, but also had the greatest variation in length. Figure 41 is a compilation of SEM images used to document the length and morphology of the  $\text{TiO}_2$  nanotubes. Tube diameter and morphology was similar that that of the shorter film protocols; however, the surface morphology was found to be quite different than previously observed.

Figure 41. SEM images of 60-volt anodic film depicting familiar nanotube morphology with 13  $\mu\text{m}$  to 18  $\mu\text{m}$  long nanotubes (a–c), a carpet-like surface morphology identified as “grassing” (d) and closed nanotube bottom ends (e, f).

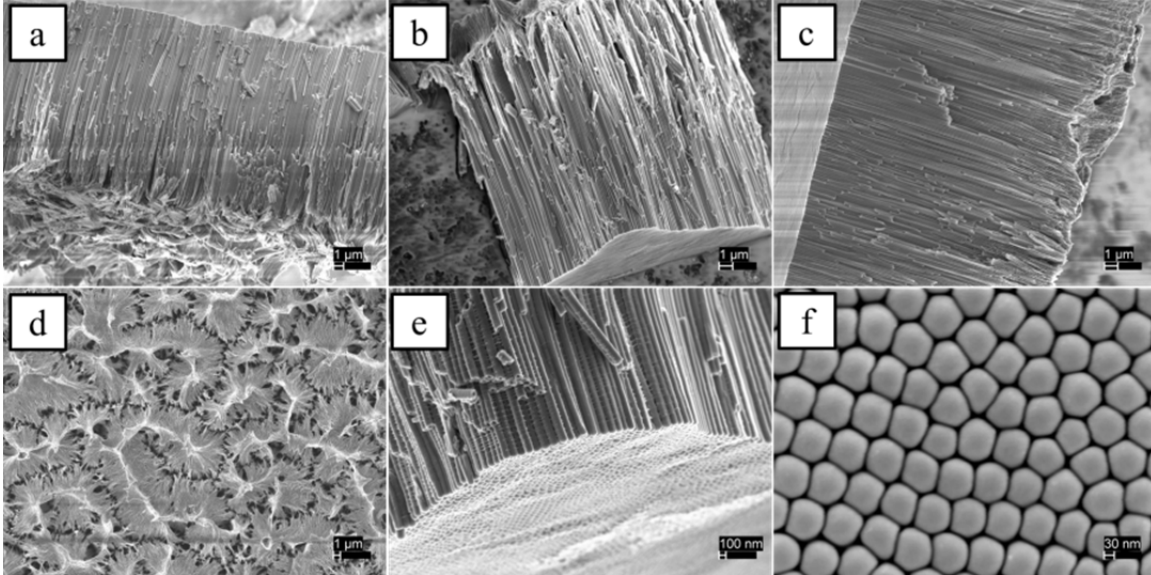


Figure 41(d) depicts the first observed “grassing” due to nearly three times the concentration of fluorides in solution. While the lower fluoride concentration techniques resulted in surface morphologies that retained remnants of the compact oxide layer, the higher fluoride technique caused a more rigorous dissolution or thinning of the tube tops, because fluorides exist in higher concentrations farther away from the regions influenced by field-aided ion transport (i.e., at the tub bottoms). This effect has been observed in a similar study [95]. Though this particular protocol delivered undesired phenomena during anodization, the resulting anodic film was found to be suitable for further analysis in an NTSDM capacitor.

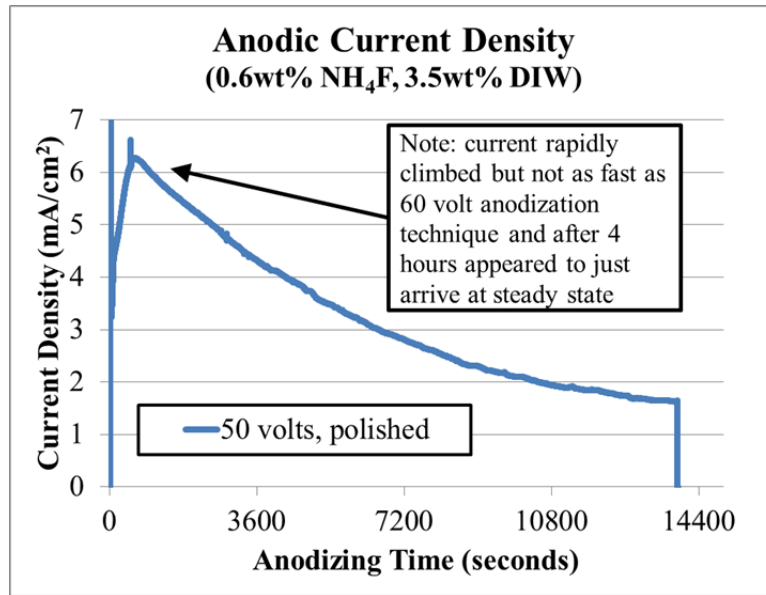
***b. Protocol: 50 Volt, 4 Hour, High Fluoride, Electrolyte Reused***

A follow-on protocol was developed in order to reuse the same electrolyte from the first anodization procedure but to use a lower anodic potential in order to avoid complete substrate dissolution. Figure 42 is a plot of the resulting anodic current density after applying 50 volts for 4 hours. Again, the peak current density (approximately



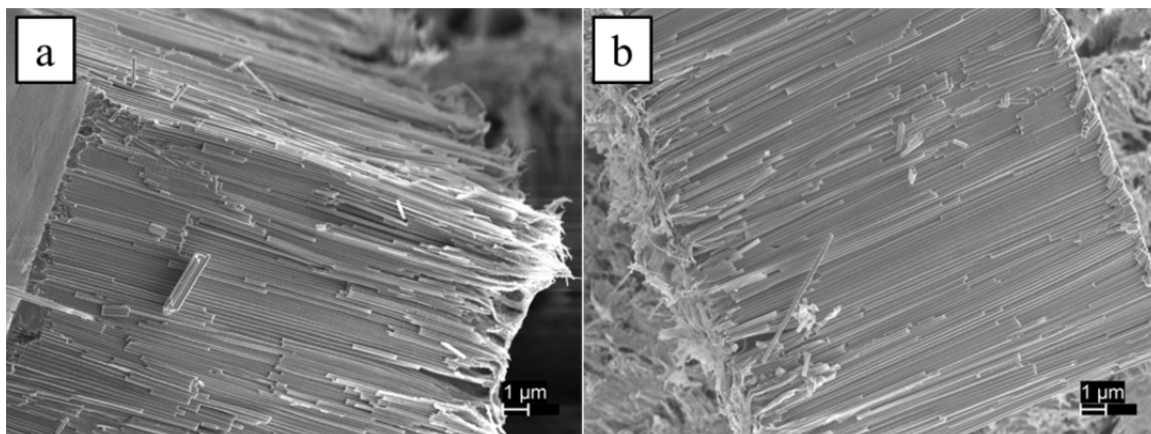
6.3 mA/cm<sup>2</sup>) was higher than any recorded during 40-volt anodization techniques and was an earlier indication of a film made up of longer nanotubes.

Figure 42. Recorded anodic current density for 50 volt, 4-hour technique reusing high fluoride electrolyte from previous 60-volt anodization.



Subsequent SEM analysis confirmed the average film thickness measured 17  $\mu$ m with examples pictured in Figure 43. Unlike the films produced during the first use of the same electrolyte, there was very little variation in nanotube length. Additionally, grassing was observed along the film surface, but not as extensively as the 60-volt anodization result.

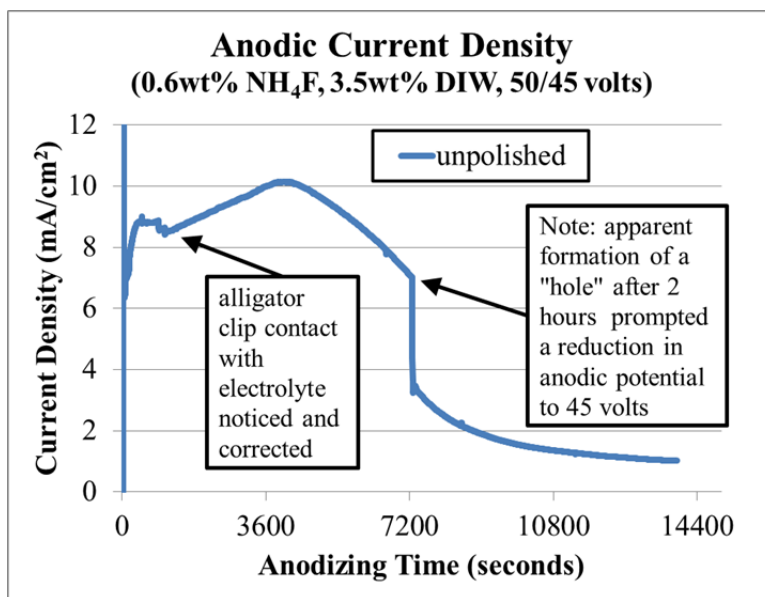
Figure 43. SEM images of 50 volt, 4-hour anodic film depicting familiar nanotube morphology with existence of 18  $\mu\text{m}$  tubes.



*c. Protocol: 50 Volt, 4 Hour, High Fluoride, New Electrolyte*

The seemingly unstable results from the higher voltage and higher fluoride protocols tested to this point were not clearly understood in-situ. Thus, another attempt was made at using 50 volts anodic potential but with a newly prepared 0.6wt%  $\text{NH}_4\text{F}$ , 3.5wt% DIW electrolyte. Additionally, since it was now believed that preparing the anode with metal polish inhibited the growth of longer tubes, the protocol was replaced with a simple ethyl alcohol rinse and allowed to air dry. No further anodization techniques within this study used the metal polish anode surface preparation. The anodization was carried out over 4 hours with careful observation of the anode and anodic current density, which was recorded and is presented in Figure 44.

Figure 44. Anodic current density recorded during the 50 volts, 4 hour, high fluoride anodization procedure; while in progress, the actual protocol was adjusted to 50 volts for 2 hours followed by 40 volts for 2 hours.

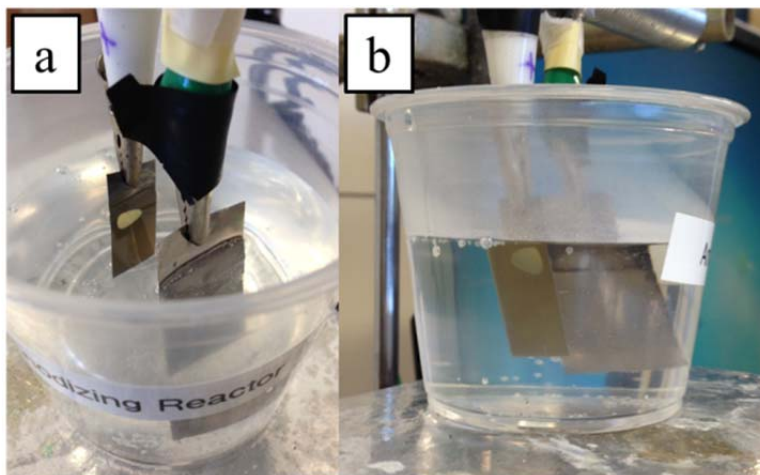


Of the noted differences in the previous 50-volt anodization technique, the first was the initial current density peak at 8.9 mA/cm<sup>2</sup> before slightly levelling. Because the initial peak during the 50 volt, recycled electrolyte protocol had only reached a local maximum of 6.3 mA/cm<sup>2</sup>, this presented cause for concern. However, the current did apparently begin to drop as is evident in Figure 44. At approximately 15 minutes, it was noticed that the alligator clip had made contact with the electrolyte and the platform height was adjusted to correct the anomaly. Shortly thereafter it was noticed that the current density began to slowly rise. Again, this presented cause for concern due to its similarity to the runaway current observed during the 60-volt protocol. A decision was made to reduce the anodic potential to 45 volts if current density continued rising past 25 mA/cm<sup>2</sup>, but after 1 hour and 10 minutes current began dropping.

After 2 hours of anodization, what appeared to be the onset of foil dissolution from the center of the anode was first observed. Figure 45 is a picture of the apparent dissolution. A “hole” formed in the center of the anode; that is, all the metal in the hole was converted to back-to-back oxide films. The anodization potential was immediately reduced to 45 volts and current density sharply dropped to 3.5 mA/cm<sup>2</sup>. This corrective

action did not immediately halt the growth of the apparent hole which continued growing until anodization was secured. A similar result was outlined by Paulose et al. [93], although their research aimed to completely anodize a 1.0 mm thick titanium substrate over nine days. Nonetheless, subsequent anodization techniques were not adjusted to prevent the complete anodization of the titanium substrate, which caused further complications while preparing for NTSDM capacitor analysis.

Figure 45. Complete anodization of a titanium substrate at 50 volts, 4 hours looks like a hole in the center of the anode, but is rather two back-to-back nanotube arrays visible from the engaged side (a) and disengaged side (b).

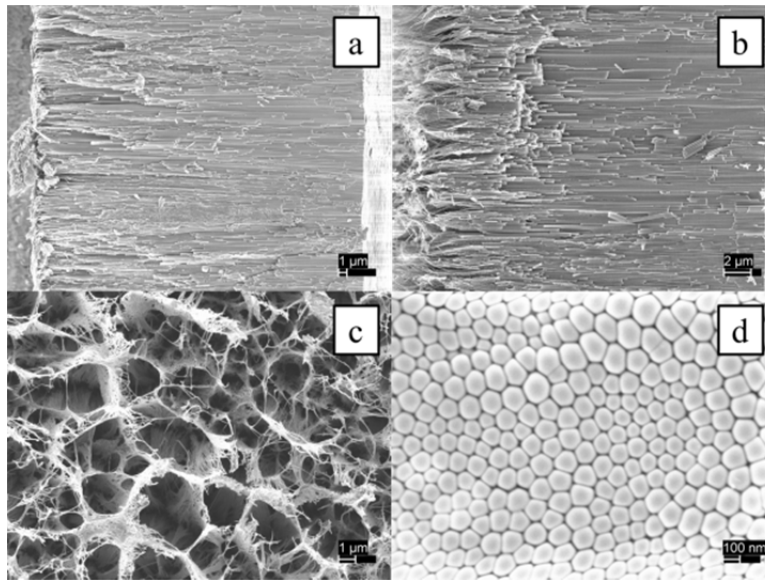


Again, as in the earlier protocol with an abrupt drop in anodizing potential, the subsequent current density dropped to an apparent steady state level consistent with the shorter oxide films. The sharp current drop is obvious in Figure 44. It was believed that any thick film growth likely occurred prior to the voltage drop; however, the generally high currents recorded up to that point indicated a particularly long film should have been grown.

Subsequent SEM analysis confirmed the existence of the thickest yet oxide film with nanotubes measuring up to 39  $\mu\text{m}$  but also with great variation in length down to 26  $\mu\text{m}$ . Cross sectional images of the films are presented in Figure 46(a) and Figure 46(b). Again, grassing was observed along the film surface and is obvious in Figure

46(c). Finally, tube bottoms shown in Figure 46(d) were closed as in previous anodization protocols. The variation in tube length discovered during SEM analysis was also noted during the adjusted 60-volt protocol. This undesired phenomenon led to the conclusion that in-process changes to anodization potential should be avoided at all costs in subsequent anodization techniques.

Figure 46. SEM images of 50 volt, 4-hour anodic film depicting familiar morphology with nanotubes measuring from 39  $\mu\text{m}$  down to 26  $\mu\text{m}$  (a,b), grassing (c), and closed bottom ends (d).



After anodization was complete, the anode was rinsed with DIW and allowed to air dry while lying horizontally within a circular test tube. As the anode dried over a matter of minutes, the oxide film appeared to become detached from the titanium substrate. This was the first apparent exfoliation of anodic film from substrate within the scope of this research. While the anode was being prepared for SEM analysis, the containing test tube, after being stored in a vacuum, was rapidly depressurized causing complete film delamination from both sides of the anode. The detached films also broke into small pieces still useful for SEM analysis but beyond practical use as a capacitor dielectric. Each of the remaining thick film anodizing techniques exhibited some degree of anodic film detachment during the drying process, but was managed in order to preserve usefulness in capacitor analysis.

Although the damaged film was not suitable for capacitor analysis, it was ideal for TEM image analysis. Fragments of the film were ground in a mortar and pestle, suspended in ethyl alcohol and dropped onto coated 3 mm diameter copper grids for TEM studies. Even though this preparation technique may further disintegrate the  $\text{TiO}_2$  nanotube array and fracture them, in this case it yielded excellent specimens for TEM analysis and provided a good insight into the features associated with the product of anodization. This also enabled evaluation of several individual nanotubes as well as groups of attached nanotube arrays.

Of primary interest, Figure 47 clearly depicts the hollow nature of a single nanotube with a slightly varying outer diameter. The average outer diameter of all nanotubes measured was 146 nm. Also apparent in Figure 47(b) and the subsequent images are rib-like features attached to the exterior of the nanotube. The “ribs” have been observed in other literature [96] and are believed to be remnants of a  $\text{TiF}_4$  interface layer left behind after the advance of the dissolution and nanotube growth into the substrate. Figure 48 captures varying nanotube wall thickness from 16 nm nearer the top to 33 nm nearer the bottom. The closed end cap is unmistakable in Figure 49 with a 75 nm thickness. Finally, the densely packed nature of the nanotube matrix is apparent with a pair of adjacent tubes in Figure 50(a) and a cluster of at least five nanotubes in Figure 50(b). TEM imagery provided proof of the nanotube morphology desired for later NTSDM capacitor analysis not readily apparent using SEM analysis.

Figure 47. TEM image capturing a midsection of a nanotube from a 29  $\mu\text{m}$  matrix with outer diameter varying between 147 nm and 158 nm.

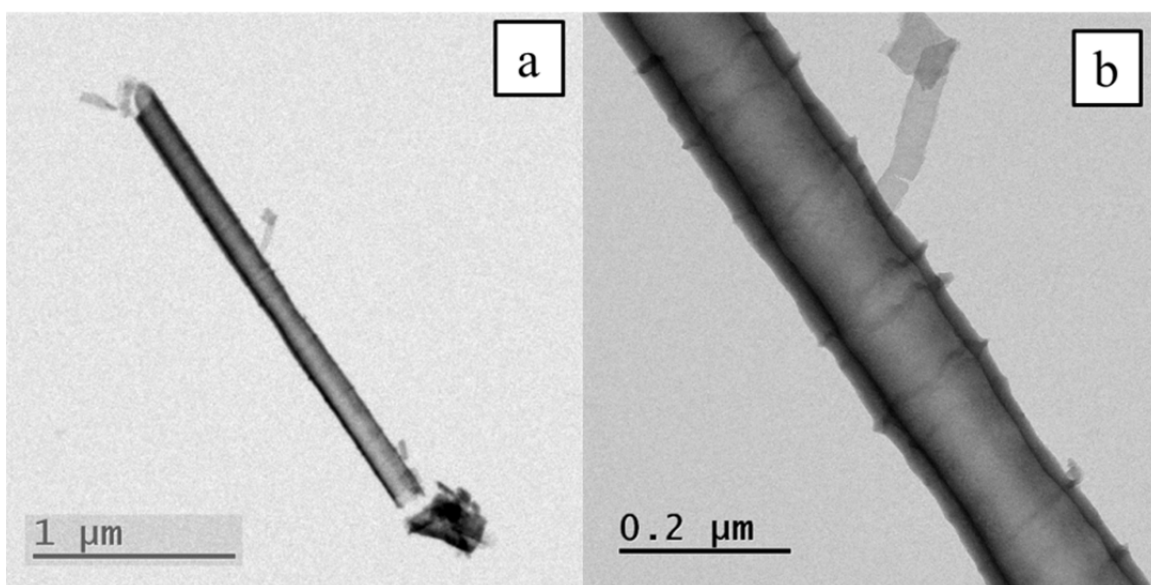


Figure 48. TEM images capturing the varying tube wall thicknesses: 16 nm near the top (a), 20 nm at mid length (b), and 33 nm near the bottom (c).

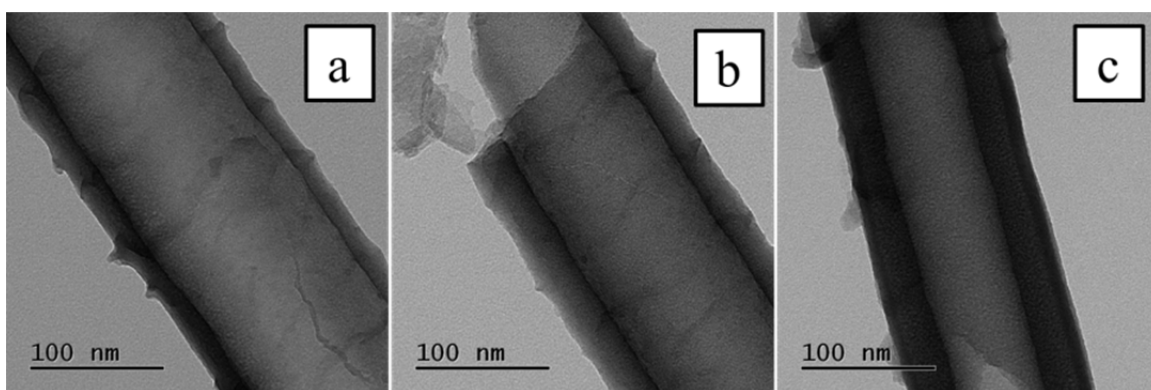


Figure 49. TEM images capturing a nanotube bottom end section from a 27  $\mu\text{m}$  anodic film (a) and the closed bottom end (b); end cap measured at 75 nm thick with 55 nm tube walls at the bottom.

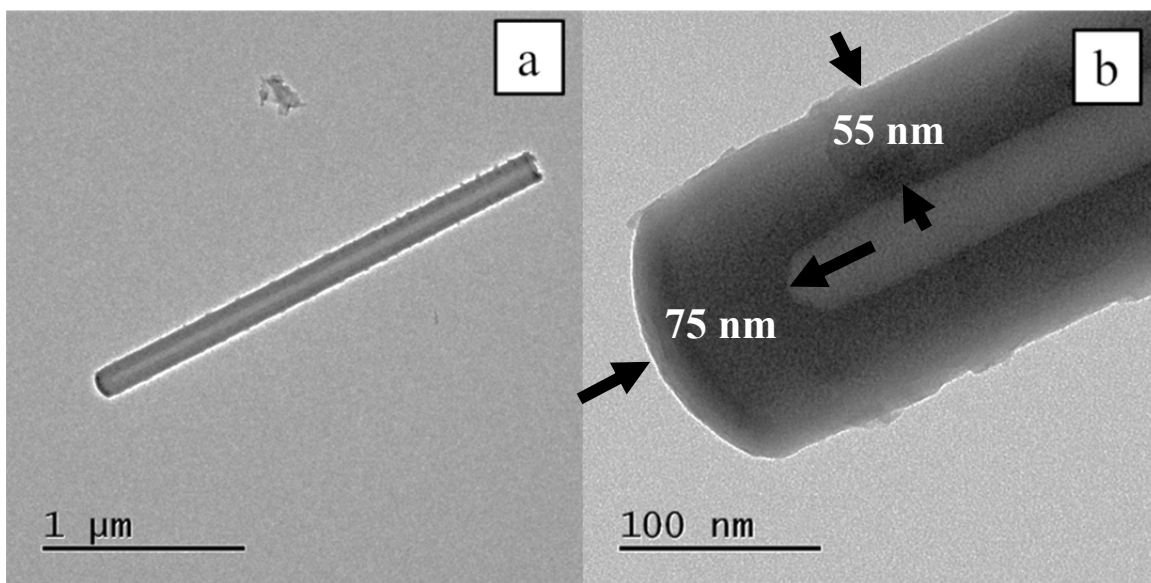
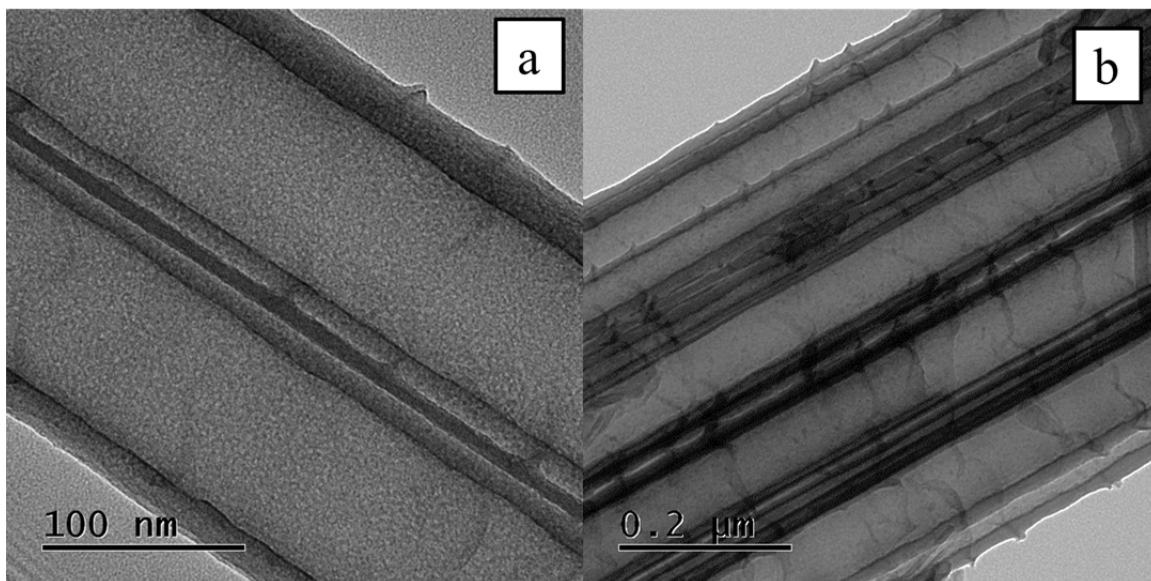


Figure 50. TEM images capturing a nanotube pair (a) and a cluster of at least 5 nanotubes stacked side-by-side and atop one another (b).

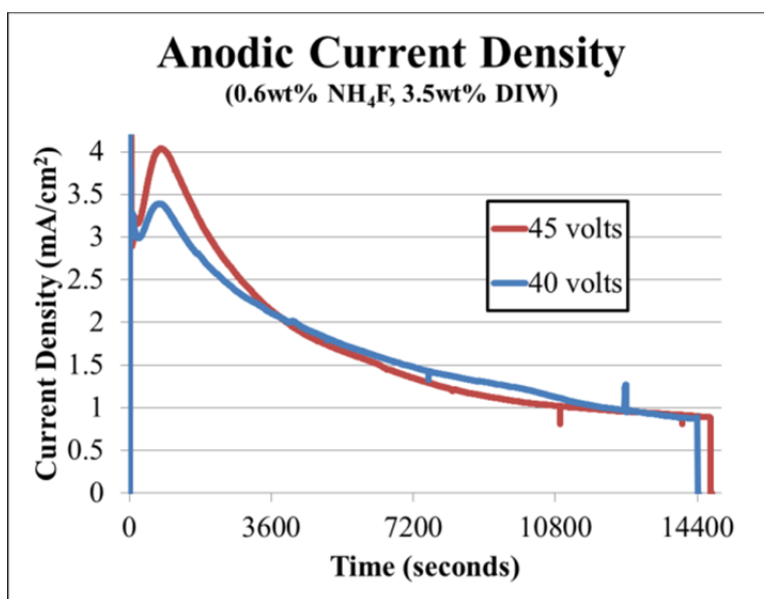




**d. Protocol: 40 Volt and 45 Volt, 4 Hours, High Fluoride**

In an attempt to avoid the complete anodization of the titanium substrate, two lower voltage protocols with high fluoride electrolytes were evaluated. Specifically, a 40 volt, 4-hour anodization followed by 45 volt, 4-hour anodization that reused the same electrolyte were completed. The two anodization techniques were completed with careful observation of the anodes and anodic current densities, plotted together in Figure 51. In both cases, no undesired dissolution of the anodic film or substrate was observed. Based on the current density comparison, the 45-volt anodization technique was expected to produce the longer nanotubes of the two techniques.

Figure 51. Anodic current densities recorded during the 40 volt 4-hour, and 45 volt 4-hour high fluoride anodization procedures.



SEM analysis confirmed that the 45-volt procedure produced longer nanotubes than did the 40-volt technique. Pictured in Figure 52, the 40-volt technique produced 6  $\mu\text{m}$  nanotubes. Other morphological attributes such as grassing and closed tube bottoms were observed and found consistent with earlier high fluoride results and are presented in Figure 52(c) and Figure 52(d). As expected, the 45-volt technique produced 7  $\mu\text{m}$  tubes pictured in Figure 53, though is not conclusive considering the errors involved in

measuring feature in the SEM imagery. A 10% to 15% error is quite within expected experimental error.

Figure 52. SEM images of 40 volt, 4-hour anodic film capturing 6  $\mu\text{m}$  nanotubes (a,b), grassing (c) and closed bottom ends (d).

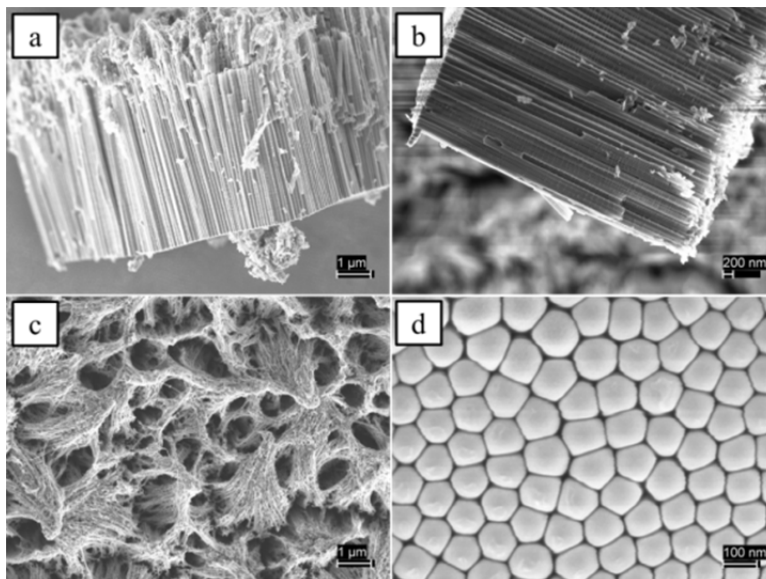
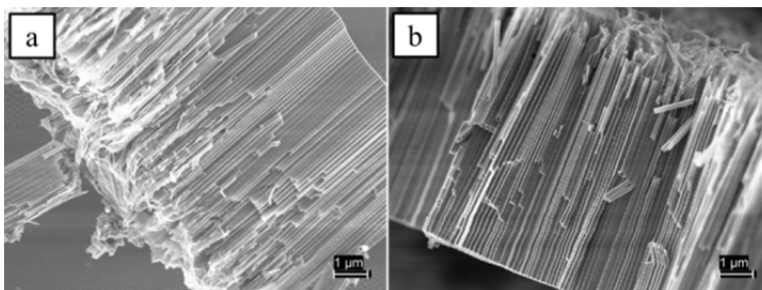


Figure 53. SEM images of 45 volt, 4 hour anodic film capturing 7  $\mu\text{m}$  nanotubes.



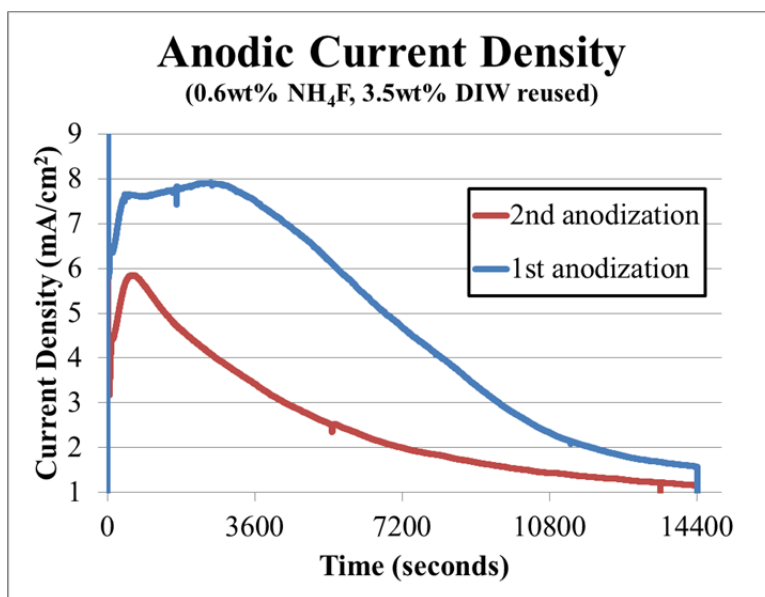
Surprisingly, though, both techniques resulted in anodic films even thinner than those grown using the previously discussed medium film protocols (those using low fluoride concentrations). The results from these high fluoride protocols reinforced the assertions from other studies [87], [93] that higher fluoride concentrations alone are not sufficient to grow thicker films. Higher potentials are necessary to promote the field-aided ionic transport and targeted anodic dissolution at the base of the nanotubes rather

than general dissolution at the outer portions of the anodic films. Effectively, lower anodic potential allows a higher fluoride concentration to exist away from the oxide and metal interface thus causing more rigorous thinning and ultimate dissolution of the nanotube tops. Consequently, this particular anodization technique was identified as a short film protocol and did not exhibit the occurrence of anodic film delamination, characteristic of the thick films. Most likely the delamination is due to the high elastic stresses that develop (mostly from the molar volume differences between the metal and  $\text{TiO}_2$ ) as the oxide film thickens, and will be discussed more later.

*e. Protocol: 50 Volt, High Fluorides, Dried Horizontally*

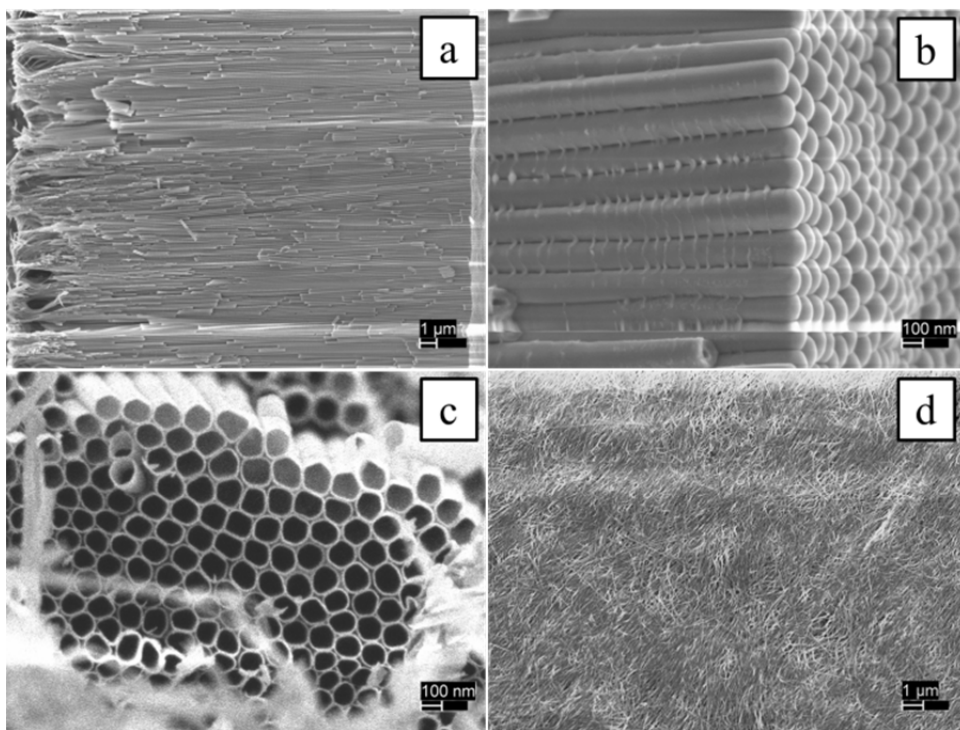
Because the anodic film produced from the earlier 50 volt, 4-hour protocol was catastrophically damaged, the anodization protocol was repeated but with a renewed emphasis on the subsequent anode drying protocol. Also, a second anodization was completed by reusing the electrolyte from the first. Figure 54 plots the first and second anodic current densities together for comparison.

Figure 54. Anodic current densities recorded during the 50 volt, 4-hour (new electrolyte) and second anodization using the same electrolyte.



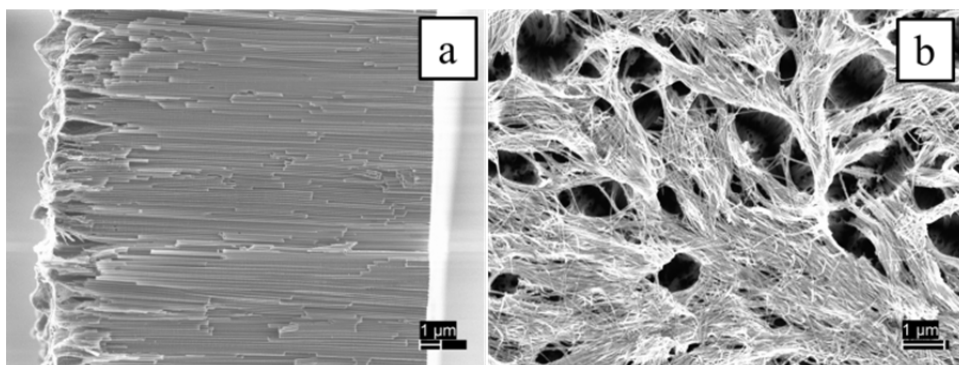
Due to its similarity to the earlier recorded anodic current density in Figure 44, the resulting film thickness was expected to measure between 26  $\mu\text{m}$  and 39  $\mu\text{m}$ . Because the anode did not form a “hole” by complete anodization of both sides from the same case, nanotube lengths were expected to be closer to the shorter side of that range. Analysis of SEM imagery, presented in Figure 55, confirmed a uniform film thickness with 27  $\mu\text{m}$  nanotube lengths on average.

Figure 55. SEM images of 50 volt, 4-hour anodic film capturing 27 $\mu\text{m}$  (a), familiar tubular morphology at tube bases (b), clean tube structure just below grassing (c), and grassing at the surface (d).



The anodic current density from the reused electrolyte trended very similarly to the 40- and 45-volt techniques plotted in Figure 51 with a narrow peak at approximately 10 minutes. Because the peak current density was lower and the peak itself much narrower than that recorded during the first anodization, the produced film was expected to be shorter. SEM imagery, presented in Figure 56, confirmed a shorter film with 18  $\mu\text{m}$  nanotubes and grassing at the film surface, though slightly different from that apparent in Figure 55.

Figure 56. SEM images of 50 volt, 4-hour (reused electrolyte) anodic film capturing 18  $\mu\text{m}$  nanotubes (a) and grassing at low magnification (b).



As mentioned earlier, subsequent storage and preparation for these thicker film specimens presented complications with delamination during rinsing and drying protocols. Whereas the thinner films exhibited great adherence to the titanium substrates, the thicker films would peel away from the substrate while they were set to dry. Figure 57 and Figure 58 depict the oxide film exfoliation that occurred when each specimen from this protocol was set on a horizontal surface to dry. For both specimens, the anodic film on side opposite delamination remained well-adhered and was suitable for further analysis as a capacitor dielectric.

Figure 57. Delamination of anodic film observed with the 27  $\mu\text{m}$  film after drying for approximately 1 hour; the arrow (b) denotes the height of the rigidly suspended anodic film.

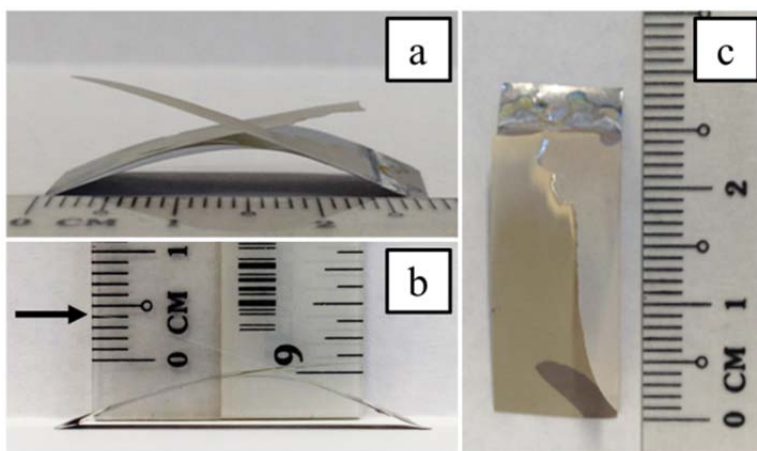
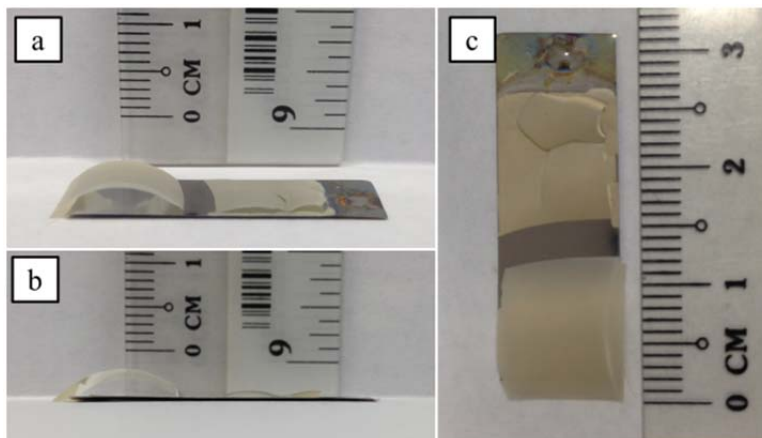


Figure 58. Delamination of anodic film observed with the 18  $\mu\text{m}$  film after drying overnight in an enclosed container.

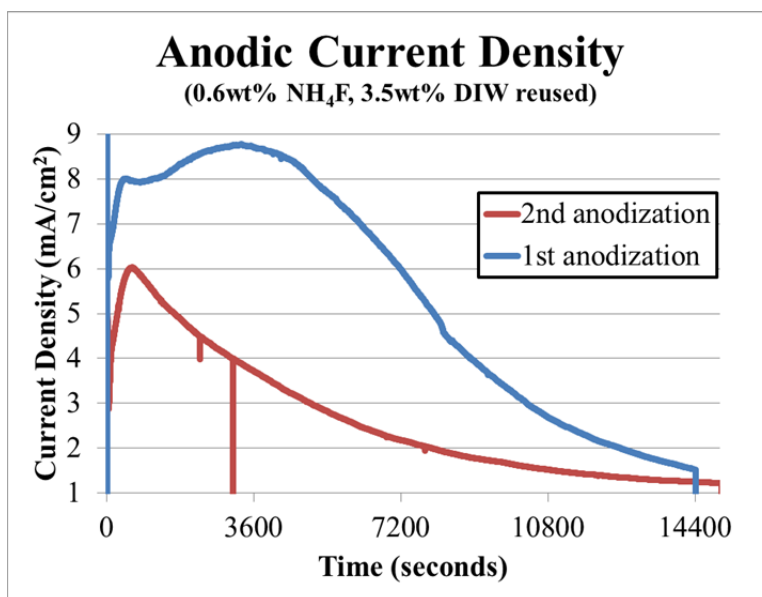


Similar problems were experienced in other studies [93] and are attributed to the surface tensional forces that develop during the drying process. Specifically, a compressive stress develops at the barrier layer and promotes anodic film separation from the titanium substrate. From the observed substrate curvature in Figure 57, it is apparent that the anodic film which remained adhered to the facedown anode surface applied a tensile force onto the substrate. Once the upper surface delaminated, the substrate curved similar to a simply supported beam with a coupled moment applied. Later, it was determined that the diminished substrate thickness, due to thick film anodization techniques, provided less than optimal rigidity and structural support when assembling NTSDM capacitors.

***f. Protocol: 50 Volt, High Fluorides, Dried Vertically***

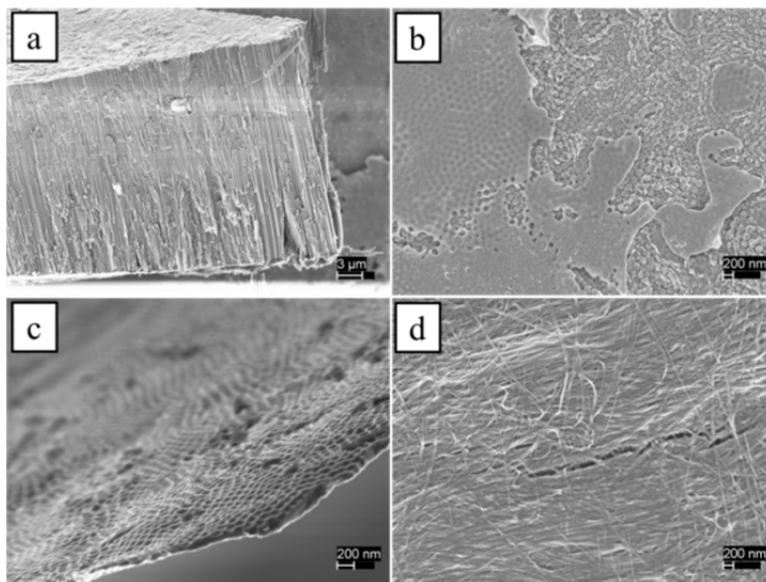
The last high fluoride protocol analyzed was a repeat combination of anodic potential and time with amended drying procedure in an attempt to prevent delamination. The anodic current density profiles for both the first and second use of the high fluoride electrolyte, plotted in Figure 59, were nearly identical to those in the previous protocol. One noticeable difference, though, was that the first anodization peaked at a current density 12% higher than the previous attempt with the same technique. Given the resulting film thickness from that earlier attempt, this new film produced from the first use of the electrolyte was expected to measure in excess of 28  $\mu\text{m}$ .

Figure 59. Anodic current densities recorded during another 50 volt, 4-hour (new electrolyte) and second anodization using the same electrolyte.



Approximately 2 hours into the anodization technique, another “hole” started forming in the center of the electrode; however, anodic potential was not reduced as it had been in the earlier protocol. SEM analysis was conducted on the resulting anodic film and was measured to be 26  $\mu\text{m}$  thick, depicted in Figure 60. Unique features were discovered between the back-to-back oxide films where the anode was completely anodized. Figure 60(b) shows the remnants of the titanium substrate that were not dissolved after becoming completely insulated from the anode and losing the field-aided ionic transport to sustain anodization. Figure 60(c) is another depiction of the thin substrate remnant.

Figure 60. SEM images of 50 volt, 4-hour (reused electrolyte) anodic film capturing 26  $\mu\text{m}$  nanotubes (a), tube bottoms with non-anodized substrate remnants (b), remnant of titanium substrate (c) and grassing (d).



The film produced from the second anodization with recycled electrolyte contained nanotubes 17  $\mu\text{m}$  in length and are pictured in Figure 61. As had come to be expected for the high fluoride protocols, grassing formed at the tube tops; however, remnants of the compact oxide layer were occasionally present. Pictured in Figure 62, this was an indication of the reduced fluoride concentration believed to exist in the recycled electrolytes.



Figure 61. SEM images of 50 volt, 4-hour (reused electrolyte) anodic film capturing 17  $\mu\text{m}$  nanotubes.

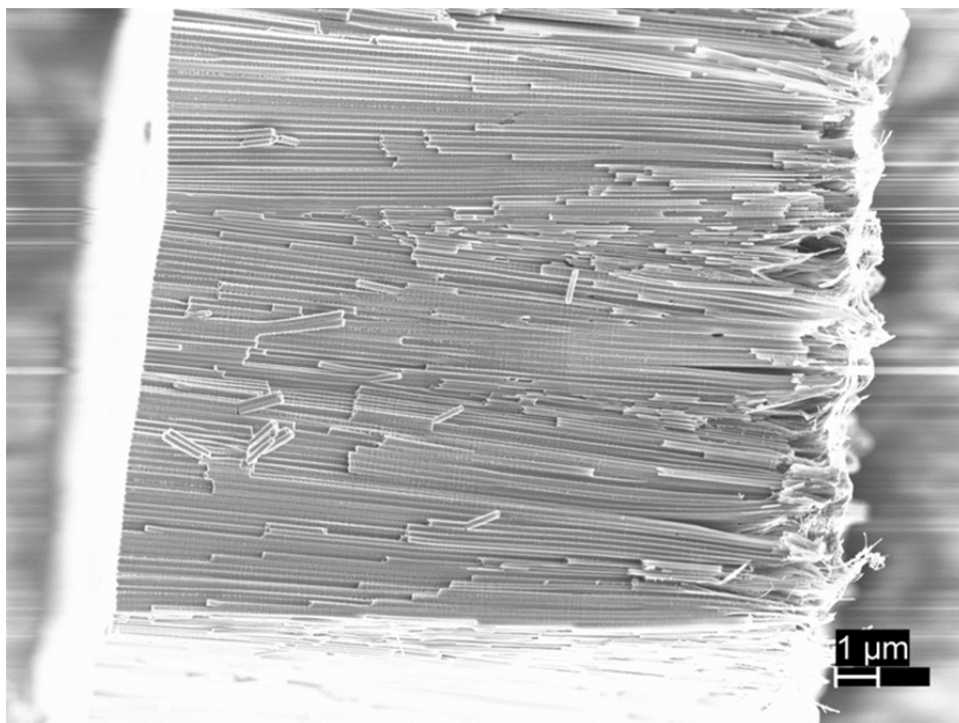
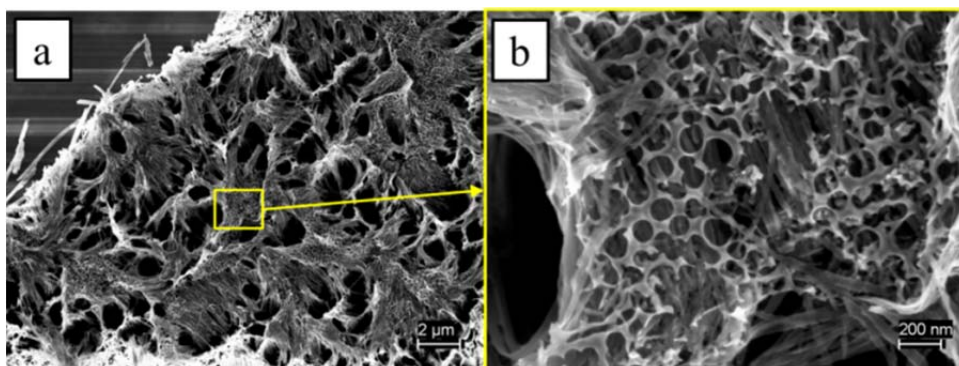


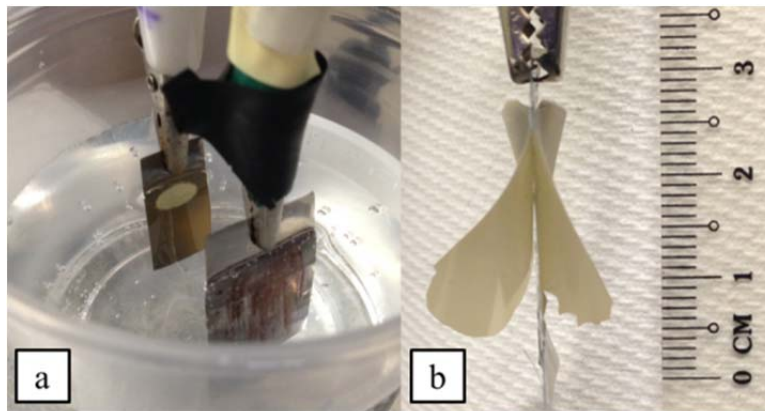
Figure 62. SEM images of 50 volt, 4-hour (reused electrolyte) anodic film with grassing (a) and apparent remnant of compact oxide layer (b).



As stated earlier, amended drying protocols were evaluated for the anodic films produced during this protocol. After being rinsed with DIW, the 26  $\mu\text{m}$  film was suspended vertically within a glass beaker containing DIW and was draped with a moist paper towel in an effort to slow down the drying process. Nonetheless, the anodic film on

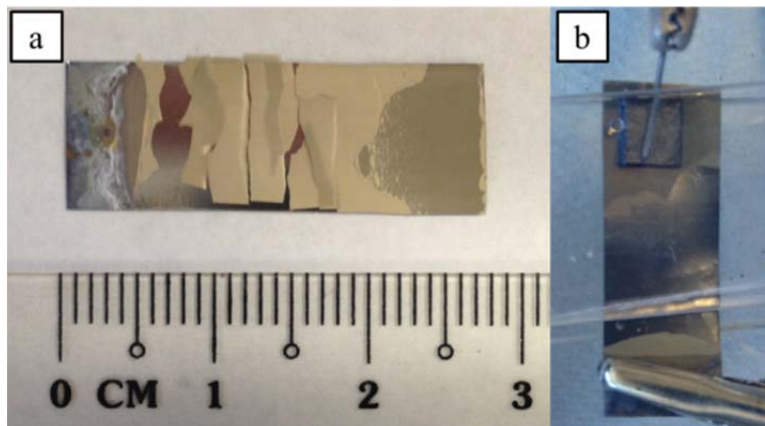
each side of the anode peeled away from the vertically suspended substrate and is pictured in Figure 63.

Figure 63. Titanium substrate completely anodized at 50 volts, 4 hours (a); subsequent 26  $\mu\text{m}$  film delamination while suspended vertically to dry (b).



The 17  $\mu\text{m}$  film was rinsed with DIW and kept in ethyl alcohol overnight. The next day it was removed and dried for capacitor analysis. Yet again, as the anode dried, the anodic film became detached from the substrate, though not as completely as the 27  $\mu\text{m}$  film. As pictured in Figure 64, a section remained adhered and was successfully used during NTSDM capacitor analysis.

Figure 64. A portion of the 17  $\mu\text{m}$  oxide film remained attached (a) and therefore viable for subsequent capacitor analysis (b).



## E. DELAMINATED FILM ANALYSES

Complications during the drying of thick films were problematic, but provided opportunities to further characterize the oxide films separate from the substrates. The most complete section of the 26  $\mu\text{m}$  anodic film, piece number 3 in Figure 65, was weighed and measured. Recorded and calculated values are tabulated in Table 6. The effective anodic film density was calculated using an assumed rectangular volume bounded by the immersed anode surface area on one side ( $2.5\text{ cm}^2$ ) and the recorded film thickness by SEM analysis. The effective density was calculated to be  $1.86\text{ g/cm}^3$  which is less than half of theoretical density for amorphous  $\text{TiO}_2$ , reported to be  $3.80\text{ g/cm}^3$  [97]. For the purpose of NTSDM analysis within this research, the volume fraction of  $\text{TiO}_2$  within the nanotube matrix is assumed to be 49.0%. The remaining volume is assumed to be completely filled with NTSDM salt solution and will be discussed in greater detail in the next chapter.

Figure 65. Thick anodic film (27  $\mu\text{m}$ ) delaminated during drying procedure from both sides of substrate (a) with visible remnants of non-anodized titanium (b).

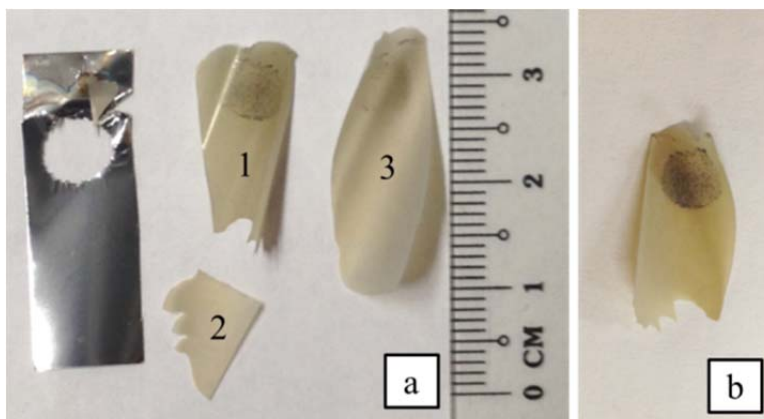


Table 6. Measurements used to calculate effective NTSDM density and weight.

<b>TiO<sub>2</sub> anodic film (26 <math>\mu</math>m) measurements</b>	
length (cm)	2.5
width (cm)	1.0
thickness ( $\mu$ m)	26
volume (cm <sup>3</sup> )	0.0065
weight (g)	0.0121
film density (g/cm <sup>3</sup> )	1.86
TiO <sub>2</sub> theoretical density (g/cm <sup>3</sup> )	3.80
TiO <sub>2</sub> volume fraction (%)	48.99
NTSDM density at 16.7% salt (g/cm <sup>3</sup> )	1.95
NTSDM density at 33.3% salt (g/cm <sup>3</sup> )	2.03

## 1. Compositional Analyses

Again, the 26  $\mu$ m thick anodic film was used for analyses other than capacitance experimentation. A small section of film, piece number 2 in Figure 65, was used for XRD analysis. The broad hump-like curve in Figure 66 with few distinct 2-theta peaks indicated a largely amorphous film composition. This is certainly expected for non-annealed films; however, two distinct diffraction peaks were found to be consistent with a documented [98] orthorhombic phase of TiO<sub>2</sub> as plotted in Figure 67. Yet, the quantitative analysis of the XRD pattern indicated that only 2.6 wt% of the overall TiO<sub>2</sub> film had a crystalline structure. For a specimen that had not been annealed, such a small quantity may be the remnant of a small oxide layer that existed on the as-received titanium foil from the manufacturer. For all practical purposes, the anodic TiO<sub>2</sub> nanotube arrays are considered wholly amorphous.

Figure 66. Mostly amorphous XRD patter for the anodic  $\text{TiO}_2$  film.

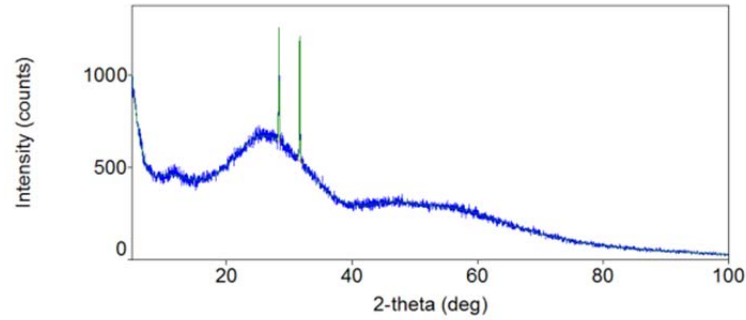
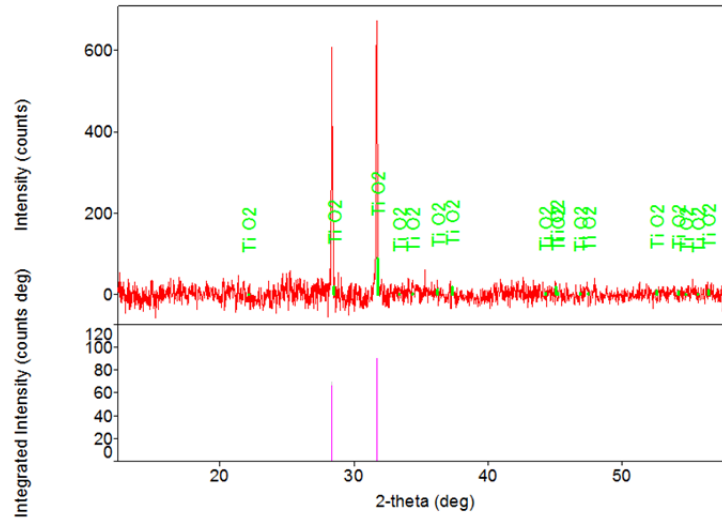


Figure 67. XRD diffraction pattern (after subtraction of the amorphous pattern corresponding to orthorhombic  $\text{TiO}_2$  (PDF Card No. 01-080-5176 in Appendix A).



## F. SUMMARY

The first aim of this research was to achieve the creation of a complex nanostructured oxide matrix for incorporation into an NTSDM capacitor. This study successfully developed and evaluated a standardized procedure for growing nanotube films of a predictable length and quality using simple materials and equipment. It is proposed that the low fluoride (0.25 wt%  $\text{NH}_4\text{F}$ , 2.75 wt% DIW), 40 volt, 4-hour anodization technique with a metal polish surface preparation produces the most well-formed nanotube anodic films with clean, open tube top surface morphology.

While the overall morphology of each TiO<sub>2</sub> nanotube film was evaluated, the primary attributes of concern to this research were the nanotube lengths, closed bottom ends, open tube tops, and general film integrity. Table 7 summarizes the successful results from all protocols detailed in Appendix B and is intended as a guide for future NTSDM anodization research.

Table 7. Summary of titanium anodization results.

Anodization voltage (V)	Anodization time (hours)	Ethylene glycol electrolyte	Electrolyte recycled	Surface preparation	Film thickness (μm)	Nanotube top morphology	Peak current density (mA/cm <sup>2</sup> )	Narrow or wide peak	Film Adhesion	Reliably suitable NTSDM
40	1	low fluoride	yes	metal polish	3 - 3.8	open tops	1.5	wide	well-attached	yes
40	2	low fluoride	no	alcohol rinse	6	open tops	---	---	well-attached	yes
40	4	high fluoride	no	alcohol rinse	6	grassing	3.4	narrow	well-attached	yes
45	4	high fluoride	yes	alcohol rinse	7	grassing	4.1	narrow	well-attached	yes
40	4	low fluoride	yes	metal polish	8	open tops	1.2 - 1.5	wide	well-attached	yes
40	4	low fluoride	no	metal polish	8 - 9	open tops	1.1 - 1.2	wide	well-attached	yes
40	4	low fluoride	no	alcohol rinse	11	open tops	1.9	wide	well-attached	yes
60	4	high fluoride	no	metal polish	13 - 18	grassing	35	runaway	exfoliated	no
50	4	high fluoride	yes	alcohol rinse	17 - 18	grassing	5.8 - 6.3	narrow	exfoliated	no
50	4	high fluoride	no	alcohol rinse	26 - 39	grassing	7.9 - 10.1	wide	exfoliated	no

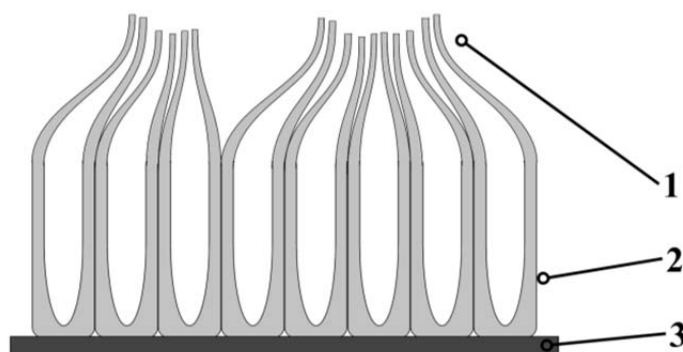
In general, thinner films with open nanotube tops can be produced at lower potentials and lower fluoride concentrations. In some cases, thin films were produced at higher potentials and fluoride concentrations but developed grassing which covered the open tube tops. NTSDM capacitors rely on the ability to fill the nanotube matrices with an aqueous salt solution, which may be more difficult with the collapsed tube tops that make up the grassing phenomenon. As pointed out earlier, grassing is due to the thinning of the tube walls after prolonged exposure to high fluoride concentrations. Thus, shorter films with clean tube openings may be achievable at higher fluoride concentrations but only at shorter durations. Other research [95] developed techniques to remove the grassing to reveal clean nanotube tops and should be considered in future iterations of this research.

Thicker films require greater than 50 volts anodic potential in concert with higher fluoride concentrations, though complete anodization of the 0.05 mm titanium substrates became a problem. If future research is to continue with the 0.05 mm substrates, utmost consideration should be placed on insulating one side of the anode within the

electrochemical cell (with tape or paint). This would prevent substrate consumption from both sides of the anode. Better yet, thicker substrates would prevent complete anodization and may simultaneously provide the structural rigidity necessary to prevent film delamination.

Surprisingly, this research discovered that increasing fluoride and water concentration without increasing voltage will actually shrink nanotube length. It is now believed that this trend is a function of more rigorous tube dissolution near the top than that at the bottom end, where lower field strength causes slower or lesser ion transport. At all voltages, much thinner tube tops formed as a result of the more rigorous dissolution with high fluoride concentrations. Figure 68 is a proposed cross-sectional depiction of the nanotube morphology that results in the grassing phenomenon observed in anodic films formed at higher fluoride concentrations.

Figure 68. Depiction of thinning tube tops and formation of grassing (1), over well-formed nanotubes (2), and titanium foil substrate (3).



In case of medium film thicknesses (7  $\mu\text{m}$  to 11  $\mu\text{m}$ ), SEM analysis confirmed metal polishing the titanium foil substrate prior to anodization reduced the overall film thickness by up to 3  $\mu\text{m}$ . At lower anodic potentials and fluoride concentrations, SEM analysis confirmed no discernible difference in tube length between the first and second anodization procedures using the same electrolyte. This was not true for 50 volt, 4-hour anodization techniques, where reusing the high fluoride electrolyte resulted in films 50% shorter than the electrolyte first use. The concentration of  $\text{NH}_4\text{F}$  and DIW is understood to be greatly depleted resulting in the shorter nanotube lengths. Future

research should consider a 50 volt, 4-hour anodization technique utilizing the lower fluoride concentration to determine the critical point at which films greater than 11  $\mu\text{m}$  are achievable.

Comparison of the anodic film from both sides of a single anode confirmed nanotube length and morphology was consistent between the two. Thus, either side of an anodized titanium substrate is suitable for capacitor analysis and, perhaps desirable, if future research attempts to fabricate multi-layer NTSDM capacitors.

Anodic film delamination presented itself as a complication to subsequent capacitor analysis. It is interesting to note that the elastic stresses at the metal/oxide interface likely caused delamination, yet the oxide film in most cases remained nearly intact. From Table 7, it is apparent that once film thickness reaches somewhere between 11 to 13  $\mu\text{m}$ , the proposed interfacial stress is sufficient to cause anodic film delamination. This is an important consideration when selecting the optimum recipe for producing  $\text{TiO}_2$  nanotube matrices for NTSDM capacitor prototypes.

Undesirable as it was, the occurrence of delamination allowed for additional analyses of the  $\text{TiO}_2$  nanotube matrices separate from the titanium substrate. Recorded weights and calculated volumes verified that nearly 50% of the anodic film is amorphous  $\text{TiO}_2$ , leaving the remaining volume to be filled with aqueous electrolytes for NTSDM analysis. TEM imagery proved the existence of desired nanotube morphology and is believed to be a collection some of the best quality TEM images of  $\text{TiO}_2$  nanotubes as compared to the bulk of literature cited beforehand.

Finally, this portion of the research successfully created 17 unique anodized titanium substrates that were found suitable for NTSDM capacitor analysis in all but two cases. This will be discussed more in the next chapters, but it is proposed that the low fluoride (0.25 wt%  $\text{NH}_4\text{F}$ , 2.75 wt% DIW), 40 volt, 4-hour anodization technique with a metal polish surface preparation produces the “best” nanotubes for performance as an NTSDM capacitor. The remaining research hereon documents the methods and analysis of NTSDM capacitor analysis in nearly 153 individual charge/discharge cycles over a 6-month period.



THIS PAGE INTENTIONALLY LEFT BLANK

## IV. NTSDM CAPACITOR EXPERIMENTAL METHODS

### A. INTRODUCTION

In order to better understand the behavior of an NTSDM capacitor as an energy storage device, their effective charge and, in particular, discharge rates must be studied. As is pointed out by Conway et al. [53], capacitive behavior can be practically demonstrated and characterized by several functional responses depending on the type of signal applied to the capacitor:

- Applied constant current where the potential difference across the capacitor changes linearly with time.
- Cyclic-voltammetry experiment with a constant voltage sweep rate where a constant capacitive charging current arises.
- Discharge experiment through a load resistor where a time dependent constant is interpolated.
- Self-discharge through a Faradic leakage process from which the Faradic or leakage resistance is observed
- Alternating current impedance experimentation

In this study, NTSDM capacitor characterization relied solely on direct current (DC) methods and primarily utilized the load resistor discharge method. For select NTSDM capacitors, a modified self-discharge method was utilized to quantify the internal and output leakage resistances inherent to each assembled capacitor.

Thus, this study focused, first, on determining the effective capacitance of a number of NTSDM capacitor designs assembled with variations in electrolyte composition, and concentration, titanium nanotube matrix thickness, electrode surface area, and applied voltages. Low frequency charge/discharge cycles were used to determine capacitance and dielectric constants of each NTSDM combination, but the ultimate goal was to determine a correlation between the varying design parameters and energy density. An optimum design yielding highest achievable energy density was identified.

The five basic means of measuring capacitance, discussed earlier, each have limitations depending on the desired analysis. Hence, it is important to select the method that best provides data supporting the proposed application. As an example, AC

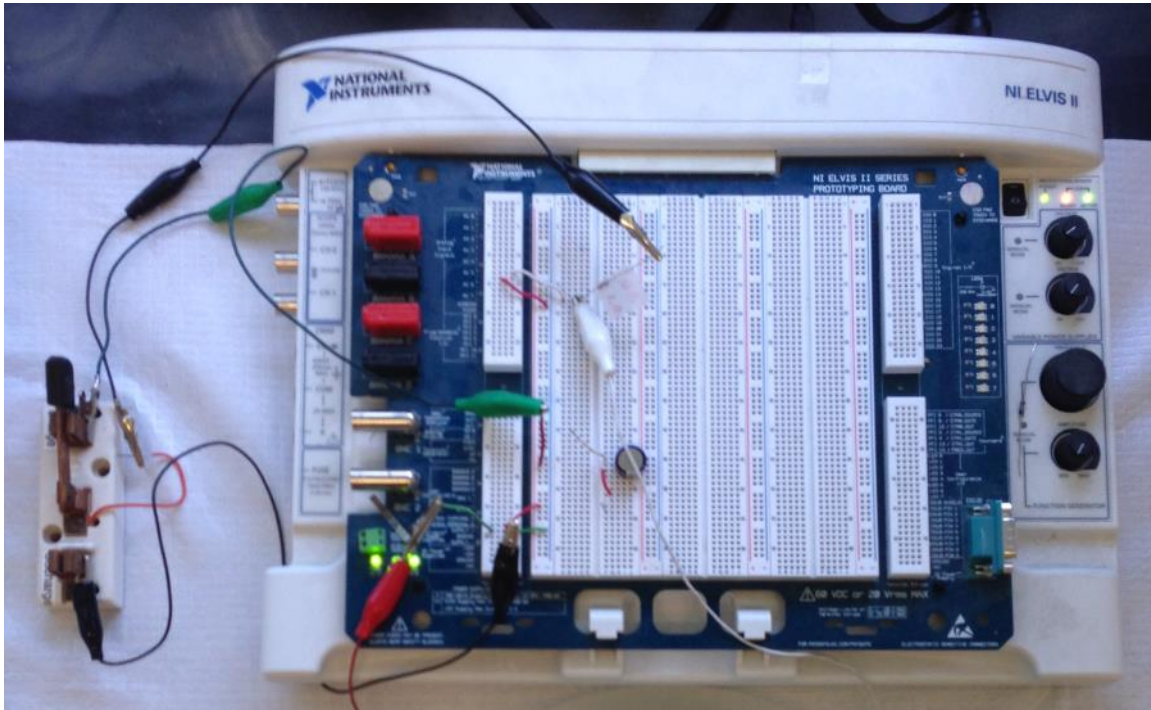
impedance experimentation, also known as impedance spectroscopy is based on deconvolution of RC time constants collected during high frequency, low amplitude charging and discharging centered on a particular voltage. A typical experiment [92] may cycle voltage  $\pm 5$  mV at 100,000 Hz centered upon a “constant” 0.1 volts. The results of such experimentation rarely include energy output as a direct measurement. If useful energy and/or energy density are to be extrapolated from such data, it can only be gained from a model of capacitance inferred from the results along with an estimated maximum achievable voltage. Therefore, such a method would be inadequate to measure the actual energy released from a fully charged NTSDM capacitor. Hence, low frequency direct current cycling was used rather than a high frequency technique which would have been more prudent if the study aimed to prove NTSDM capacitor suitability in precision electronic applications such as signal processing and filtering.

In this study and others focused on the characterization of dielectric materials and their application in energy storage capacitors [31], [32], [33], [34], capacitance was measured using the classic RC time constant method discussed earlier. In short, this was accomplished by repetitively charging each NTSDM capacitor with a constant DC voltage, and then discharging through a load resistor, all the while measuring the potential across the capacitor. The methods and equipment used to accomplish this task are discussed in greater detail in the next section.

## **B. CIRCUIT SETUP AND MEASUREMENT METHODS**

All capacitor experimentation was carried out using a customizable workstation and prototyping board (National Instruments ELVIS II Series) in conjunction with the LabVIEW-based software on a connected computer workstation. The prototyping board, pictured in Figure 69, employed alligator clips, insulated copper wire (American wire gage 20), and a copper knife switch mounted on a ceramic bedplate. The applied voltages during charge were specified using the LabVIEW computer interface, while the voltage across the capacitor was plotted in-situ and recorded directly on the computer using the same.

Figure 69. National Instruments ELVIS II workstation with ceramic bedplate knife switch for charging and discharging.



The classic RC discharge circuit wired onto the prototyping board is presented as a schematic in Figure 70 with the switch in the charging position. In this arrangement, each NTSDM capacitor was charged for specified length of time. On discharge the switch was flipped, depicted in Figure 71, at which point the voltage drop across the capacitor was recorded over time. The load resistor for all experiments was rated as 10k $\Omega$ , but measured to be 10.8 k $\Omega$  using a Fluke multimeter. All RC time constant calculations were based on the measured resistance.

Figure 70. NTSDM test circuit schematic with switch in charge position.

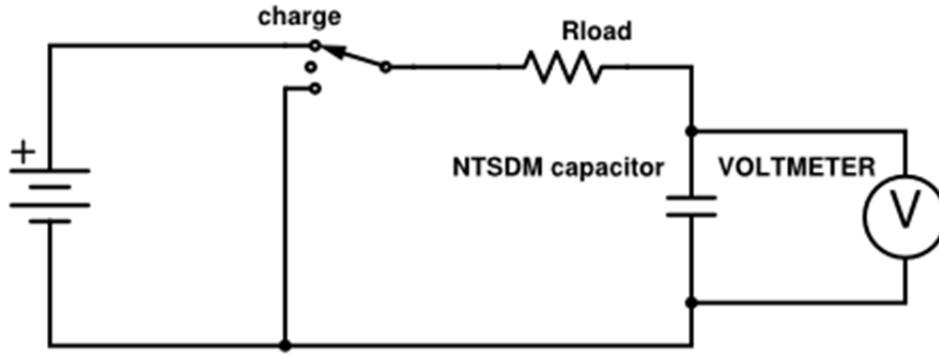
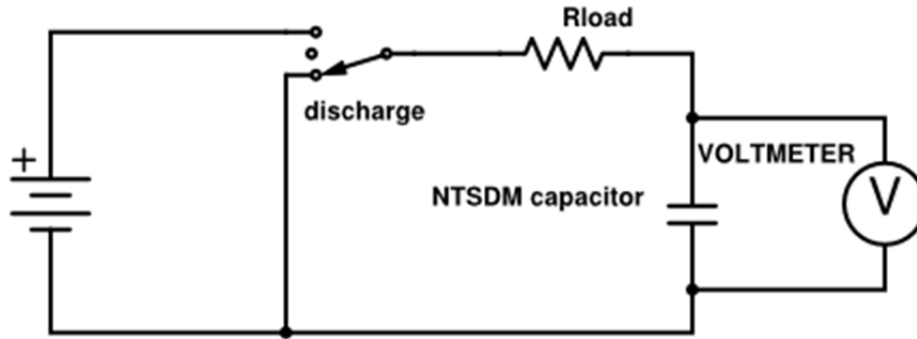


Figure 71. NTSDM test circuit schematic with switch in discharge position.



## 1. Capacitance Measurement

Voltage was recorded for each second during each charge and discharge cycle and then plotted as a function of time. As was expected for the load resistance discharge method, a (saw) tooth curve was readily apparent and is depicted in Figure 72. The time dependent relationship of discharging voltage is governed by the following relationship:

$$V(t) = V_o \exp \left[ -\frac{t}{RC} \right] \quad (7)$$

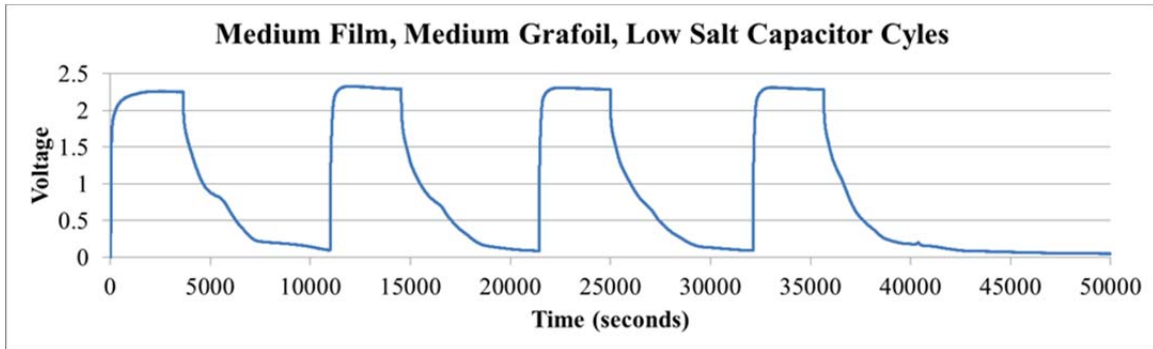
Then, the  $RC$  time constant was calculated by recording the slope ( $-1/RC$ ) of the interpolated linear fit in accordance with the following mathematical expression:

$$\ln \left[ \frac{V(t)}{V_o} \right] = -\frac{t}{RC} \quad (8)$$

Figure 73 is provided as an example of the log pot vs. time of a particular discharge. As has been discussed before, NTSDM capacitors appeared to exhibit three distinct regions of capacitance across high, intermediate, and low voltage ranges. The three distinct linear regions are apparent in Figure 73. Each region also has a corresponding linearly interpolated equation whose slope is the  $-1/RC$  value for that region.

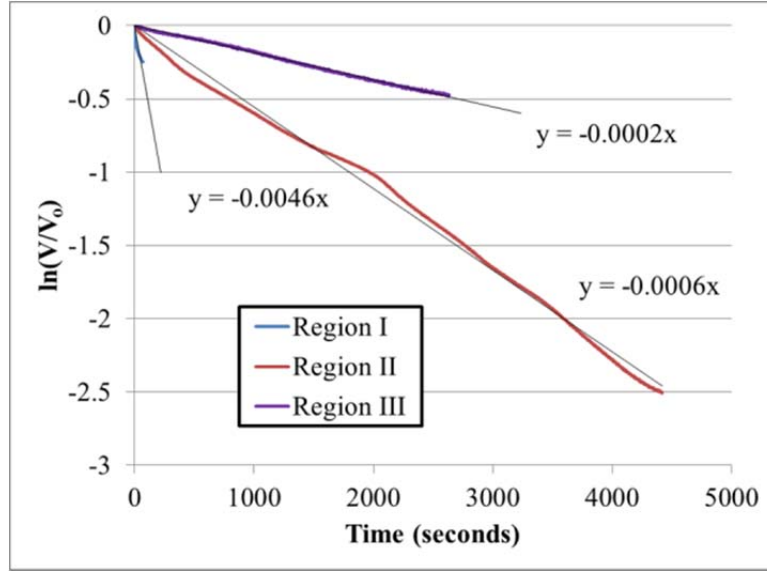
The vast majority of all NTSDM capacitors were found to have increasing values of capacitances from Region I to Region III. However, as will be discussed in the section pertaining to energy density calculation, the only useful contribution to energy storage was found to exist in Region II. The effective capacitance from each region was calculated based on a known load resistance and the interpolated RC time constant. In all cases, Region II was found to contain the bulk of energy and usually encompassed the widest range of voltage. For this reason, each NTSDM capacitor was characterized based on its performance in Region II.

Figure 72. Example of an NTSDM charge/discharge plot with 6 volts applied during charge; this particular plot contains 4 charge/discharge cycles.



Note the typical discharge time is about 5,000 seconds, but was adjusted according to the applied voltage for different experimental regimens.

Figure 73. Example of an NTSDM discharge log plot over time with three distinct regions of linear behavior.



## 2. Dielectric Constant Calculation

Referring back to the background discussion on capacitor technology, it is proposed that NTSDM capacitors most closely fit within the electrostatic capacitor category. That is, the simplest explanation of an NTSDM capacitor is simply a parallel plate capacitor with a dielectric material between. Even though it is acknowledged that certain attributes of their design and performance mimic characteristics of other capacitor categories, it is still appropriate to apply Equation (2) in determining the dielectric constant of the NTSDM. Equation (2) was rearranged, solving for the relative permittivity of the NTSDM and is presented as Equation (9).

$$\epsilon_r = \frac{C}{\epsilon_o} \frac{d}{A} \quad (9)$$

Just as in the determination of capacitance, each NTSDM was characterized by its respective capacitor performance in Region II. Hence, the calculated capacitance from Region II was used to determine the dielectric constant of the NTSDM in Region II. The relative permittivity of each NTSDM was characterized based on its Region II dielectric constant.

### 3. Energy Density Calculation

Energy stored and delivered during each discharge cycle was calculated separately according to the measured capacitances and associated voltage ranges across Regions I, II, and III. The resulting energies were summed up to determine the total energy delivered during each cycle. As previously discussed, the majority of the energy delivered by NTSDM capacitors on discharge occurs in Region II. The energy density was then calculated by dividing the calculated energy by the rectangular volume of the dielectric material bounded by Grafoil length, Grafoil, width, and anodic film thickness (nanotube length).

Two different methods were used to calculate the average energy density for each NTSDM capacitor. Values are reported in units of joules per cubic centimeter ( $\text{J}/\text{cm}^3$ ) and are the average of all charge/discharge cycles for that particular NTSDM combination. Equation (10) represents the basic calculation of energy stored by a capacitor from peak voltage down to zero and assumes a constant capacitance over the entire range of discharge.

$$\text{Energy stored} = \frac{1}{2} CV^2 \quad (10)$$

Equation (11) is the calculation of energy for each unique region of discharge where different values of capacitance were observed.  $V_{high}$  represents the maximum voltage in each region and  $V_{low}$  is the minimum voltage in each region.

$$\text{Energy stored in each region} = \frac{1}{2} C(V_{high}^2 - V_{low}^2) \quad (11)$$

The accuracy of the energy density calculation for each NTSDM capacitor using Equations (10) and (11) is assumed to be only as accurate as the linear interpolation of the RC time constant according to Equation (8). For this reason, a more accurate method of calculating energy density was considered. Energy stored was also calculated by numerical integration of the recorded discharge voltages ( $V_i$ ) squared divided by the load resistance according to Equation (12).



$$\text{Energy stored} = \sum_{i=1}^{end} \frac{V_i^2}{R_{\text{load}}} * \Delta t \quad (12)$$

Because most discharges rarely discharged down to zero, the most correct numerical analysis should not consider the lowest recorded voltage for energy storage purposes. Equation (13) is the numerically integrated calculation of energy from the recorded voltages over each second minus the energy remaining at the last recorded voltage.

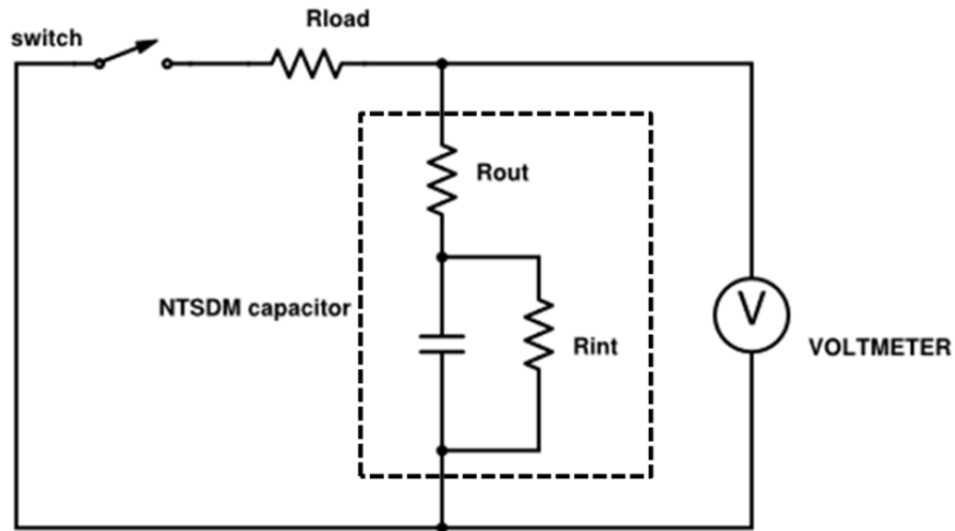
$$\text{Energy stored} = \sum_{i=1}^{end} \left( \frac{V_i^2}{R_{\text{load}}} \right) * \Delta t - \frac{V_{\text{end}}^2}{R_{\text{load}}} * t_{\text{end}} \quad (13)$$

For all NTSDM capacitors tested, the numerically integrated energy density was found to be a lesser value than the energy density calculated from interpolated capacitance values. However, the best performing NTSDM capacitor with the highest capacitances demonstrated less error between the three region interpolation energy density and that estimated by numerical integration. For the purpose of this study, each NTSDM capacitor's energy density was characterized by the numerically integrated value and is the average energy density listed in Appendix C.

#### 4. Leakage Resistance Measurement

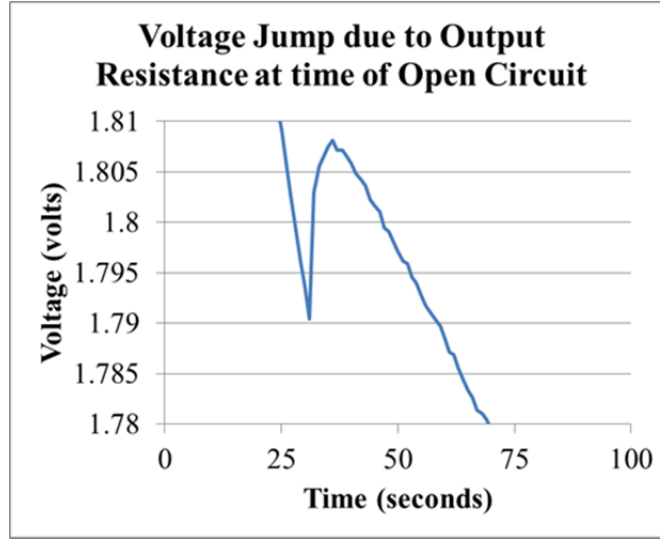
While an ideal capacitor would store its charge indefinitely and then discharge it with zero resistance, the real world case is much different. All capacitors regardless of design or construction can actually be modeled as a theoretical circuit with one output resistor ( $R_{\text{out}}$ ) in series and one internal resistor ( $R_{\text{int}}$ ) in parallel [53]. The portion bounded with a dotted line in Figure 74 is the theoretical circuit contained within each NTSDM capacitor.

Figure 74. Schematic of the equivalent discharging circuit with theoretical NTSDM capacitor components; switch is depicted in the open circuit position.



A fully charged capacitor will not indefinitely hold its charge when disconnected from its charging source. The charge built up on each plate will slowly discharge, and so capacitors are assumed to have a leakage resistance which is modeled as the  $R_{int}$  resistor. Likewise, at the instant the discharging capacitor is disconnected from its load, a voltage spike can be recorded. Figure 75 is an example of the transient spike recorded after open circuiting the NTSDM capacitor. For most cases, the capacitor was discharged normally for 30 seconds to ensure the capacitor was discharging in Region II prior to the open circuit. The spike in potential is attributed to the equivalent voltage divider circuit created by the disappearance of load resistor ( $R_{load}$ ) and the presence of the output resistance ( $R_{out}$ ) within the NTSDM capacitor.

Figure 75. Voltage spike recorded at instant of open circuit on a charged NTSDM capacitor.



The following equations were derived using loop and nodal analysis on the circuit pictures in Figure 74.

$$R_{out} = \frac{V_{peak} - V_{load}}{V_{load}} * R_{load}$$

$$V_{peak} = \text{peak voltage after open circuit}$$

$$V_{load} = \text{voltage recorded at open circuit}$$
(14)

The internal resistance, or that which is simulated by  $R_{int}$  in Figure 74, is calculated by recording the slope (inverse RC time constant) of the linear interpolation of the open circuit discharge in accordance with Equation (14). The internal resistance is solved for by using the average recorded Region II capacitance from previous discharge cycles.

### C. MATERIALS AND NTSDM ASSEMBLY

The concept for NTSDM assembly was based on previous work completed at NPS [2], but modified according to “best practices” discovered during the course of this study. The first phase of assembly involved “soaking” one of the suitable anodized foil specimens in a aqueous salt solution. Various soak times, from 1 hour to 1 week, were evaluated with no discernible advantage or improved performance between them. By and large, the 1 hour soak time was the most often used protocol. Three electrolyte salts at

various concentrations were used during the course of this study: boric acid (Sigma Aldrich), non-iodized table salt (Morton), and pure sodium chloride (Sigma Aldrich).

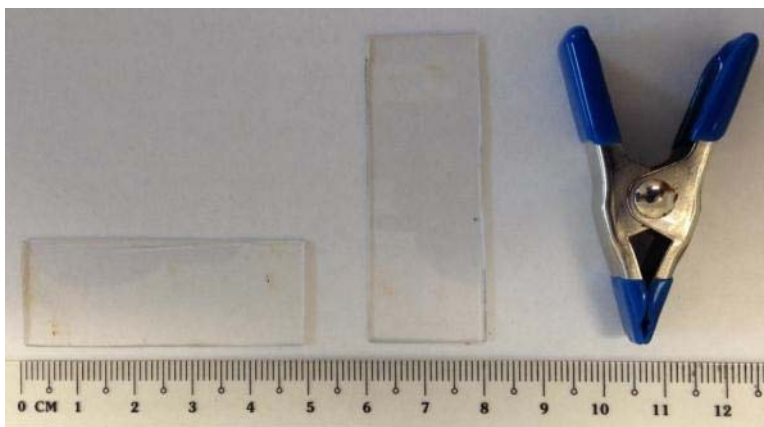
Of note, the table salt contained an unspecified quantity of calcium silicate, used as an anticaking agent. The presence of this additive was especially noticeable as a film remaining on the surface of the solution, when mixing with DIW close to the solubility limit. After this discovery, the table salt was replaced with pure NaCl. Another complication discovered during the experimental regimen was the particularly high acidity, pH 3 measured with pH indicator strips (EMD Chemicals Cat. 9590), of the DIW used during the first two months of experimentation. This discovery was made after experiencing great difficulty in achieving complete salt dissolution at concentrations less than but close to the solubility limit, even at elevated temperatures. This problem ceased after replacing with a new batch of DIW measured at pH 6. Table 8 lists the specific salts and concentrations evaluated during this study.

Table 8. List of various salts and accompanying concentrations used during NTSDM capacitor analysis.

<b>Salt</b>	<b>Concentration (wt%)</b>
boric acid	3.33
table salt	16.7
pure NaCl	16.7
pure NaCl	33.3

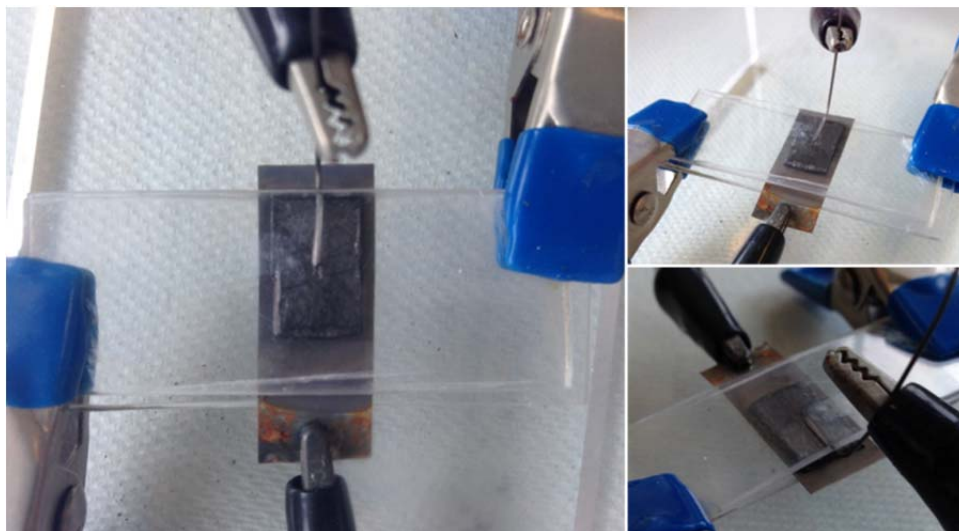
The next phase of capacitor assembly was to actually assemble the capacitor. Each NTSDM capacitor was suspended between two rectangular plastic retainers (length, width, thickness), pictured in Figure 76. The plastic was held together using the spring loaded clamps, also pictured in Figure 76 at right, one at each end. Clamp placement was decided in order to provide sufficient force to ensure full surface area contact between the electrodes, but not so strong that it would cause damage to the anodic film with excessive pressure.

Figure 76. Capacitor assembly components.



In each NTSDM capacitor, the soaked anodized foil (negative electrode) with Grafoil (positive electrode) and tungsten wire electrode were carefully placed and set. Figure 77 depicts an example of a fully assembled NTSDM capacitor ready to be put through charge discharge cycles. Special attention was paid to the tungsten wire electrode to ensure it did not make contact with any excess moisture at the edge of the negative electrode.

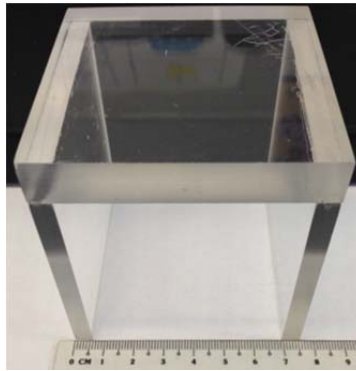
Figure 77. Fully assembled NTSDM capacitor ready for testing.



As in previous research [2], a tungsten wire was chosen over a copper wire after discovering an undesirable chemical reaction that occurred between the copper and the

salt electrolyte during anodization. Also, particular care was taken to ensure the Grafoil was centered in the middle of the anodized foil. Previous research [2] determined that an electrical short was likely to develop between the Grafoil and the anodized titanium if the two made contact at the edge. Finally, the assembled capacitors were protected from mechanical disturbance by covering with a plastic containment, pictured in Figure 78.

Figure 78. NTSDM capacitor containment chamber.



Every assembled NTSDM capacitor resembled that in Figure 77 with variations in Grafoil size, salt concentration, moisture content, and clamp placement. Each capacitor was charged and discharged for at least two cycles but as many as nine over a three day period. The primary control parameters evaluated during the capacitor method of experiments were electrolyte concentration, anodic film thickness and Grafoil size (surface area). Table 9 is a summary of the varying parameters used during the method of experimentation.

Table 9. Control parameters used in NTSDM capacitor method of experiments.

Film Thickness	Salt Concentration	Gafoil Size
Short ( $d \leq 6 \mu\text{m}$ )	Low (16.7 wt%)	Small ( $25 \text{ mm}^2$ )
Medium ( $6\mu\text{m} < d \leq 17 \mu\text{m}$ )	-	-
Thick ( $d > 17 \mu\text{m}$ )	High (33.3 wt%)	Large ( $96 \text{ mm}^2$ )

Finally, it was discovered that the duration of cycle repetition and, similarly, the maximum number of cycles was limited by the ability to maintain a constant level of humidity within the NTSDM containment. During the course of NTSDM capacitor analysis, an additional measure was taken to prevent the dielectric from drying out and, conversely, from becoming too wet from excessive humidity in the containment. First, a damp paper towel was draped over the cube-shaped containment chamber taking care not to make contact with the tungsten wire or alligator clips. A hole was cut in the paper on top of the containment in order to provide a window for observation. Second, the hemispherical lid of a vacuum chamber was placed over the entire assembly to further mitigate the dry out of the electrolyte. The entire assembly is pictured in Figure 79.

Figure 79. NTSDM capacitor test assembly with humidity control cover.



#### D. VERIFICATION OF CAPACITOR CIRCUIT

In order to verify the assembled switching circuit and voltmeter operated correctly, a 220 mF super capacitor (PowerStor KW Series 5R5C224-R) was analyzed over a single charge and discharge cycle. The supercapacitor was charged using a 5-volt DC source, and discharged after reaching 2.3 volts (a level comparable to NTSDM maximum operating voltage). Analysis from this cycle was subsequently used as a comparative benchmark for NTSDM capacitor performance and characterization. The charge/discharge cycle is plotted in Figure 80 and certainly exhibits a clean “saw-tooth” shape expected for RC time constant analysis. The discharge voltages were then plotted on a log plot over time. Figure 81 is the resulting clean, linear plot from which the RC time constant was interpolated.

Figure 80. A single charge/discharge cycle using a 220 mF supercapacitor with 5.0 volts applied to verify circuit and switching operation.

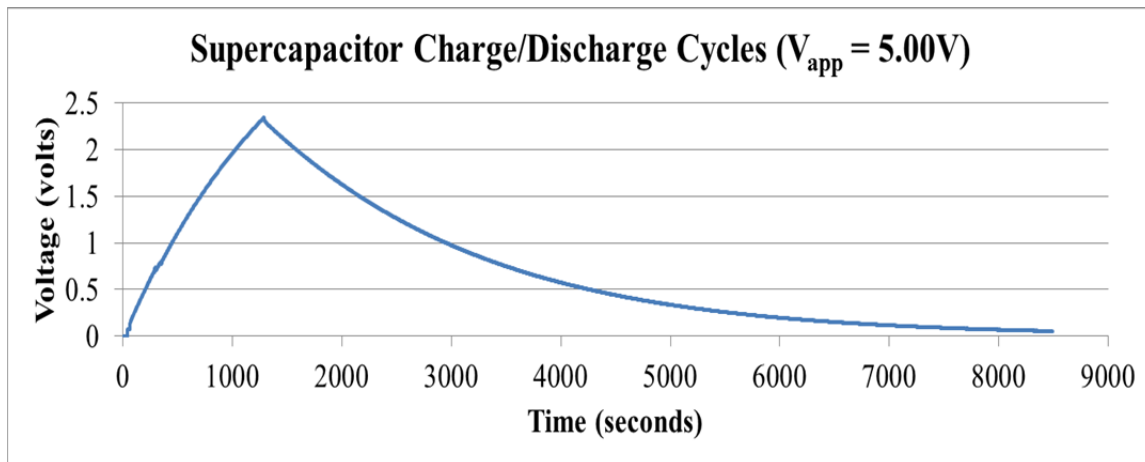
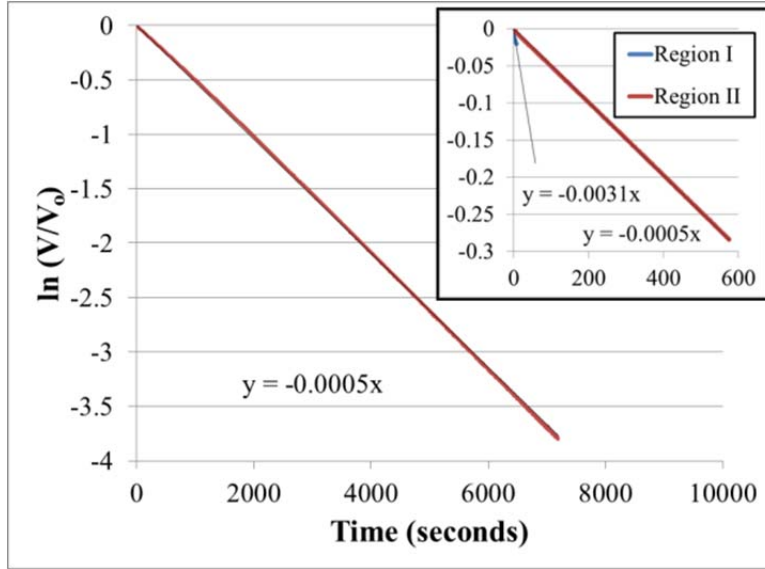




Figure 81. Discharge log plot versus time demonstrating RC time constant by linear interpolation; inlay plot has shortened time scale demonstrating Region I discharge still exists in supercapacitors.



By comparing Figure 81 to Figure 73, it is obvious that the supercapacitor does not exhibit the three separate regions of capacitance observed in NTSDM capacitors. However, a short initial region of discharge (Region I) is still apparent and is consistent with the initial discharge transient expected in the initial seconds after discharge commences. It is proposed within this study, that the Region I discharge is a product of the rapid reversal of polarity and instantaneous flow of electrons from the capacitor to the load resistor. The initial rapid loss of voltage slows down after current becomes limited by flow through the load resistor. In the case of the supercapacitor, the subsequent steady state discharge is a clean straight line on the  $\ln(V/V_o)$  plot indicating a constant capacitance value over the entire range of discharge. Table 10 and Table 11 are tabulations of the two different calculations for energy and energy density. The predictable behavior of EDLC energy storage is further highlighted by the matching values for energy stored between the two methods. Even though the measured capacitance is less than the rated capacitance, it falls within the manufacturer specified tolerance. Density calculations were based on a measured volume of  $1.06 \text{ cm}^3$  according to the measured dimensions pictured in Figure 82.

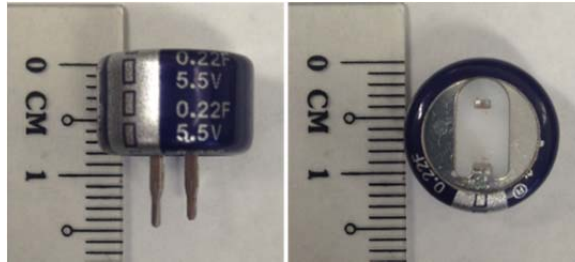
Table 10. Supercapacitor energy analysis using calculated value for capacitance.

Energy calculation based on $\frac{1}{2}CV^2$ by region			
Region	I	II	TOTAL
V high (V)	2.35	2.30	-
V low (V)	2.30	0.05	-
-1/RC	0.00312	0.00050	-
C (F)	0.0297	0.1837	-
Energy (J)	3.42E-03	4.85E-01	0.49
ED (J/cm <sup>3</sup> )	3.22E-03	4.57E-01	0.46

Table 11. Super capacitor energy analysis based on numerical integration.

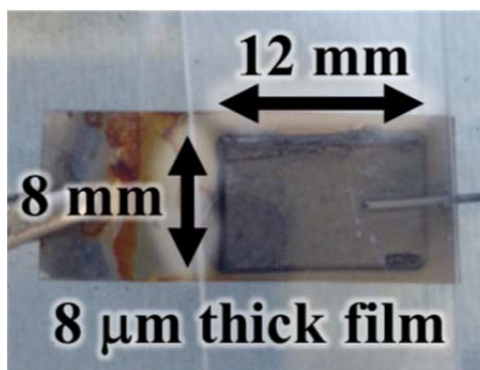
Numerical Integration of $V^2/R$		
Energy (J)	=	0.49
ED (J/cm <sup>3</sup> )	=	0.46

Figure 82. Supercapacitor used for circuit verification and benchmark energy density comparison.



Finally, it is worth noting the physical size of the 184 mF (by empirical analysis) supercapacitor compared to the best large Grafoil NTSDM capacitor calculated at 199 mF. A picture of the 199 mF NTSDM capacitor is capture in Figure 83.

Figure 83. NTSDM capacitor with 96 mm<sup>2</sup> Grafoil electrode and 8 μm thick anodic film with 199 mF capacitance.



Where the supercapacitor occupies an approximate 1 cm<sup>3</sup> volume, the effective volume of the NTSDM was measured to be 7.68E-4 cm<sup>3</sup>. Although a liberal estimate, the NTSDM capacitor demonstrates 99.9% volume reduction alongside 8.2% increased capacitance. Such a significant reduction in volume is startlingly optimistic, and certainly demonstrates promise for refinement and application of NTSDM capacitor technology.

## **V. NTSDM RESULTS AND ANALYSIS**

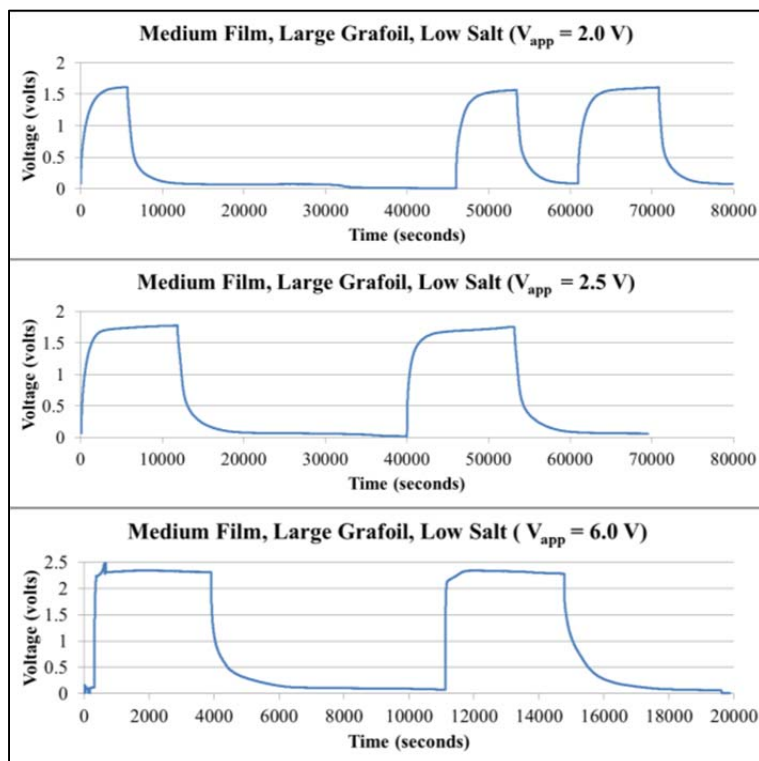
### **A. ASSUMPTIONS AND INITIAL CONDITIONS**

Unless otherwise specified, the results discussed herein are for NTSDM capacitors comprised of a TiO<sub>2</sub> nanotube matrix, an aqueous NaCl electrolyte solution and a Grafoil positive electrode. A comprehensive list of all findings for each capacitor is included in Appendix C of this thesis, but the ultimate performance metric for NTSDM capacitors was their associated energy densities. Of course, capacitive energy density is proportional to voltage squared according to Equation (10), presented in the previous chapter. The apparent operating voltages of NTSDM capacitors present a real limitation to the total energy stored and practical application of such devices. Particularly during charge and discharge cycling, the NTSDM capacitors demonstrated an upper limitation on operating voltage between 2.0 and 2.3 volts. A previous NPS study [2] routinely used an arbitrarily chosen 6.0 volt charging voltage and identified a maximum charge potential of 2.0 to 2.2 volts. However, within the scope of this study, it was important to select the optimum charging voltage—one that would guarantee a timely charge, an energy dense discharge, and multiple cycles without apparent damage to the NTSDM.

#### **1. Maximum Operating Voltage vs. Applied Voltage**

One particular NTSDM design (Ti\_042415\_AM from Appendix C) with medium film thickness (8  $\mu\text{m}$ ) and large Grafoil electrode (96  $\text{mm}^2$ ) was selected to test the impact of applied voltage on capacitance and energy density. The first regimen of voltage variation utilized a low salt concentration (16.7 wt%), while the second iteration a high salt concentration (33.3 wt%). The low salt capacitor was charged and discharged using 2.0 volts, 2.5 volts and 6.0 volts multiple times each. In most cases, discharges were not commenced until the rate of charge dropped to less than 1 mV/min. The recorded voltages just prior to discharge were classified as the maximum operating voltage. That is, the rate of charge had reached the point of useful return on energy storage. Figure 84 is a comparison of the charge/discharge cycles for each voltage utilized.

Figure 84. Low salt NTSDM charge/discharge cycles for various applied voltages.



Of note, the maximum operating voltage increased as applied voltage was increased. While the protocols with lower voltages required up to 3 hours to achieve the maximum charge voltage, the 6.0 volt charging protocol only required 30 minutes to achieve the maximum operating voltage. Note the much shorter time scale for the 6.0 volt plotted data in Figure 84. The two 6.0-volt cycles were actually charged for just over 1 hour. The earlier protocols in the experimental regimen called for 1-hour charge cycles, but were later changed to commence discharge as soon as charge rate dropped below 1.0 mV/min. Figure 85 overlays the two 2.5-volt discharges on top of one another with an expanded time scale and is useful in portraying the typical capacitive discharge of an NTSDM capacitor. The similarity between the two discharge profiles also demonstrates the consistent discharge behavior between subsequent discharges.

Figure 85. Two discharges from 2.5-volt charge protocol overlaid onto the same graph.

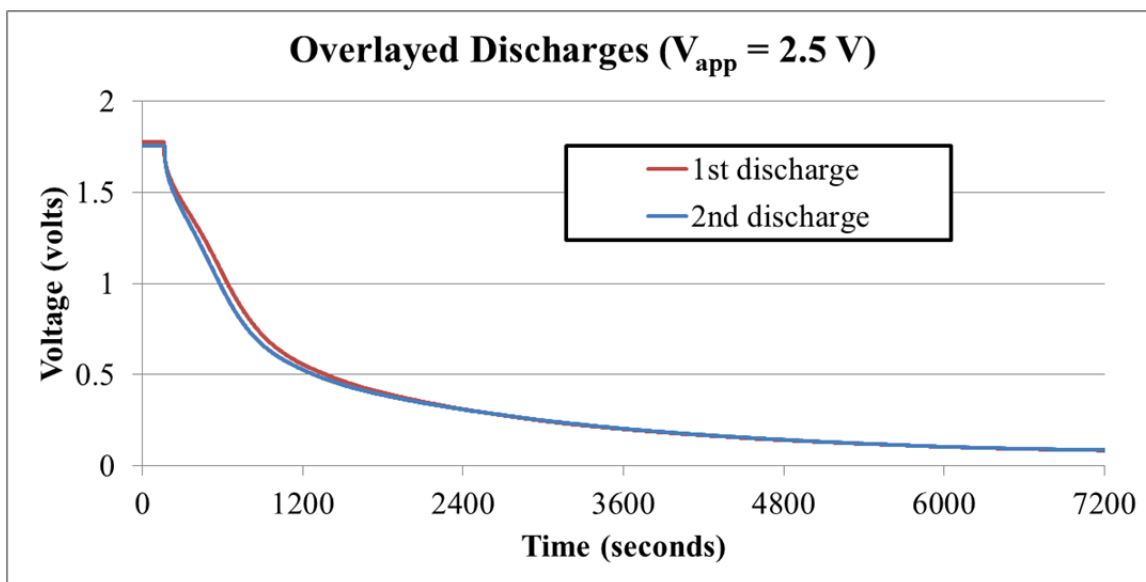
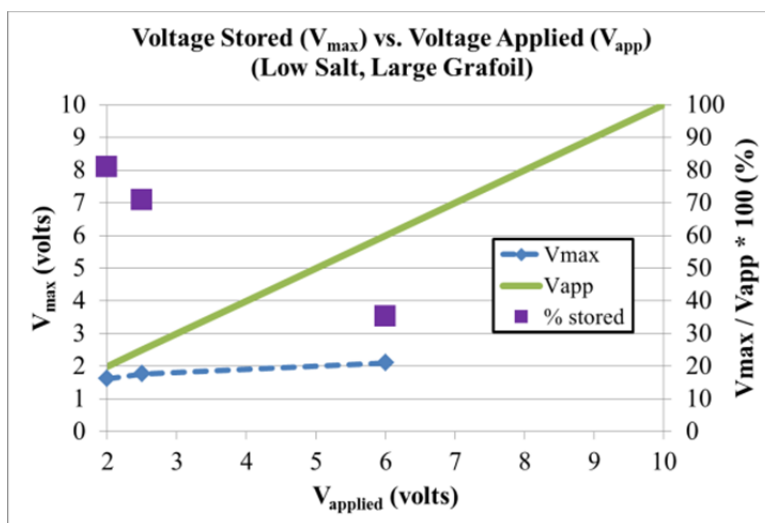


Figure 86 is a plot of the apparent maximum operating voltage as a function of the applied voltage. The plotted percentage of voltage stored indicated an exponential decrease as applied voltage was increased. This indicated that the maximum operating voltage should reach a limit, or level off, as applied voltage is increased. The original experimental regimen called for retiring the low salt NTSDM capacitor after evaluating it up to 6.0 volts. A repeat of the test with higher applied voltages seemed prudent after noting the apparent operating voltage limit from the low salt data. The follow-on high salt analysis charged an NTSDM capacitor up to 10.0 volts.

Figure 86. NTSDM capacitors with 16.7 wt% NaCl electrolyte reach a high voltage limit of approximately 2.3 volts with 6 volts applied.



The high salt capacitor was charged and discharged using 2.0 volts, 4.0 volts, 6.0 volts, 8.0 volts and 10.0 volts. In most cases, discharges were not commenced until the rate of charge dropped to less than 1 mV/min. Figure 87 is a comparison of the cycle performance at each applied voltage from which two observations are readily apparent. First, the maximum operating voltage increases as the applied voltage is increased just as in the case of the low salt capacitor. Second, the required charge time is dramatically reduced at the higher applied voltages. When 10.0 volts were applied, the charge cycle only lasted for 10 minutes.

Figure 87. High salt NTSDM charge/discharge cycles for various applied voltages

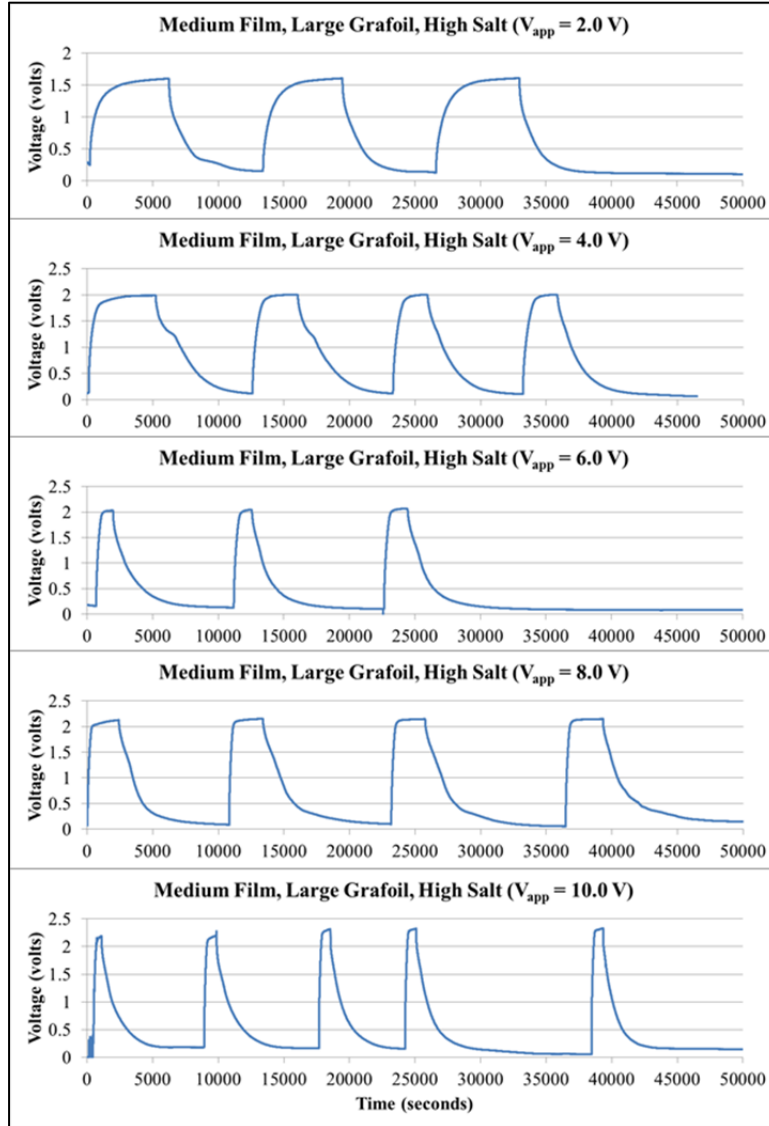
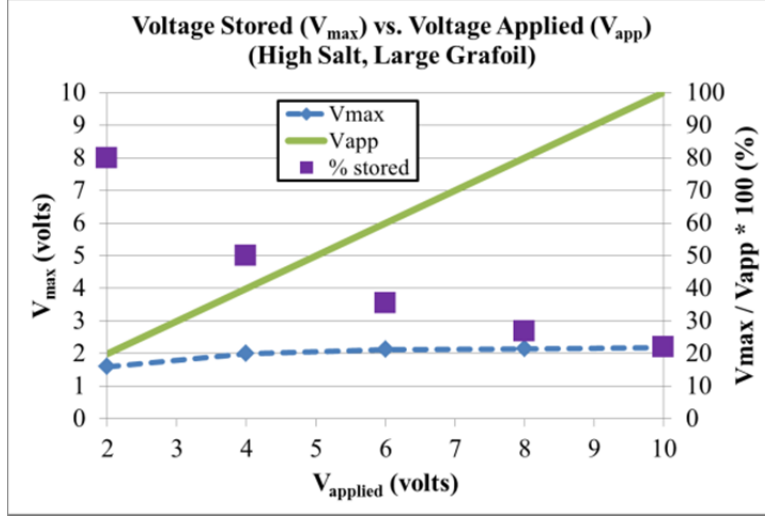


Figure 87 is a plot of the apparent maximum operating voltage as a function of the applied voltage for the high salt capacitor. Again, the percent of voltage stored of that applied indicated an exponential decrease, and the maximum operating voltage did appear to reach a limit as applied voltage was increased. Specifically, the highest achieved voltage for this particular design was 2.19 volts at the highest applied voltage. As evidenced by the recorded data in Appendix C, higher maximums were observed in other capacitor designs at 6.0 volts applied. Hence, the true maximum is believed to be a



design dependent variable which is subject to subtle variations in each design that occur during the anodization or assembly process.

Figure 88. NTSDM capacitors with 33.3 wt% NaCl electrolyte reach a high voltage limit of approximately 2.01 volts with 6 volts applied.



## 2. Energy Density vs. Applied Voltage

As mentioned earlier, an advantage to higher applied voltages is the shorter duration required to reach the apparent voltage limit. Because energy stored is proportional to voltage squared, it was assumed that the associated energy density for each higher applied voltage would also be greater. However, the energy stored is also a function of the capacitance which should also be unique to each capacitor design (salt concentration, film thickness and electrode surface area). As discussed earlier in the background theory, the proposed NTSDM model relies on the polarization of the electrolyte in each nanotube to form a dipole. Therefore, higher field strength as a function of the applied voltage should form stronger dipoles and thereby greater capacity for energy storage. That is, the measured RC time constants for each discharge were expected to be characteristics specific to each assembled capacitor and the applied voltage. For both the low and high salt capacitors, the capacitance and energy density for each discharge was averaged and is tabulated in Table 12.

Table 12. Low and high salt NTSDM capacitances and voltages for varying applied voltages.

$V_{app}$	$V_{max}$		Capacitance (mF)		Energy Density (J/cm <sup>3</sup> )		Theoretical ED (J/cm <sup>3</sup> )	
	Low Salt	High Salt	Low Salt	High Salt	Low Salt	High Salt	Low Salt	High Salt
2.0	1.62	1.61	67.3	112.7	107	162	-	-
2.5	1.77	-	79.8	-	169	-	151.5	-
4.0	-	2.00	-	160.4	-	371	-	355.8
6.0	2.11	2.13	199.0	192.2	334	396	536.7	483.6
8.0	-	2.15	-	153.8	-	429	-	394.3
10.0	-	2.19	-	130.1	-	295	-	346.0
4.0	-	2.11	-	165.9	-	420	-	409.6

Although, the full range of applied voltages were not thoroughly evaluated with the low salt capacitor, obvious trends presented themselves. Qualitatively, the high salt capacitor recorded larger values of capacitance than its low salt counterpart to a point. By doubling the salt concentration in this particular design, a 67.5% increase of capacitance was recorded at 2.0 volts but a 3.4% decrease at 6.0 volts. The low salt capacitor achieved a maximum capacitance of 199.0 mF with 6.0 volts applied and a maximum energy density of 334 J/cm<sup>3</sup>. At the same voltage, the high salt capacitor achieved 192.2 mF and 396 J/cm<sup>3</sup>.

Up to 6.0 volts, the data for both salt concentrations tended to support the theory that a stronger field results in higher capacitance. However, as charge/discharge cycles were continued at 8.0 and 10.0 volts applied on the high salt capacitor, the calculated capacitances dropped. However, at 8.0 volts applied the reduction in capacitance was mitigated by the increased maximum voltage achieved and resulted in the highest energy density recorded for a large Grafoil capacitor at 429 J/cm<sup>3</sup>. Yet, charging with 10.0 volts resulted in a rapid drop in energy density down to 295 J/cm<sup>3</sup>.

If Equation (10) holds true, then the relationship defined by Equation (15) should also hold true for any combination of applied voltage and capacitance where the theoretically achievable energy density ( $ED_B$ ) is proportional to the ratio of calculated capacitances and the square of the ratio of the maximum achieved voltages.

$$ED_B = ED_A * \left( \frac{C_B}{C_A} \right) \left( \frac{V_B}{V_A} \right)^2 \quad (15)$$

The data recorded in the fifth column of Table 12 was calculated according to Equation (15) using the calculated capacitance and energy density at 2.0 volts applied for  $C_A$  and  $V_A$ , respectively. The highlighted values for both the low and high salt capacitors indicate the theoretical calculation exceeded the recorded value. Hence, it would appear a breakdown in the relationship governed by Equation (10) occurs at applied voltages beyond 6.0 volts. Yet, as demonstrated in Figure 89 and Figure 90, the trend between maximum achieved voltage on charge and the calculated energy density indicate a distinct similarity or interdependence up to 8.0 volts.

Figure 89. Energy density and maximum achieved voltage trends in a low salt NTSDM capacitor up to 6 volts.

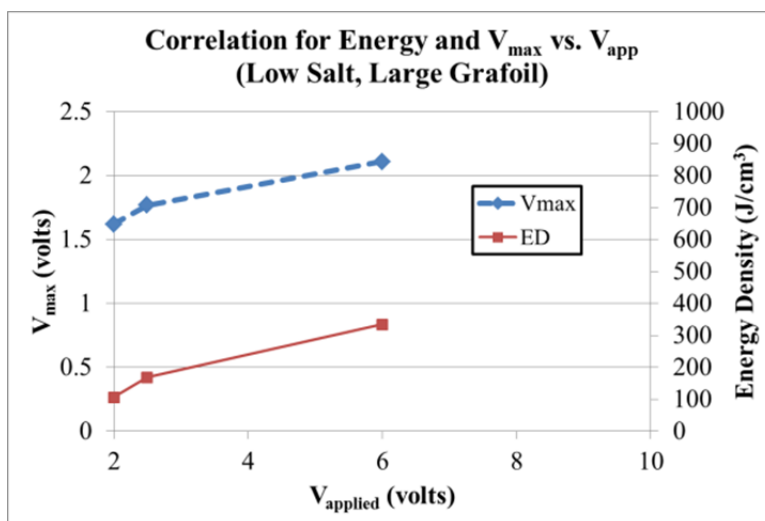
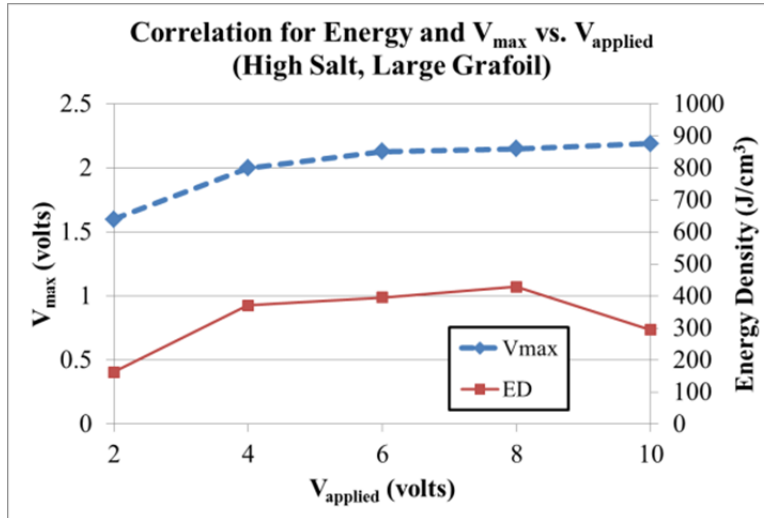


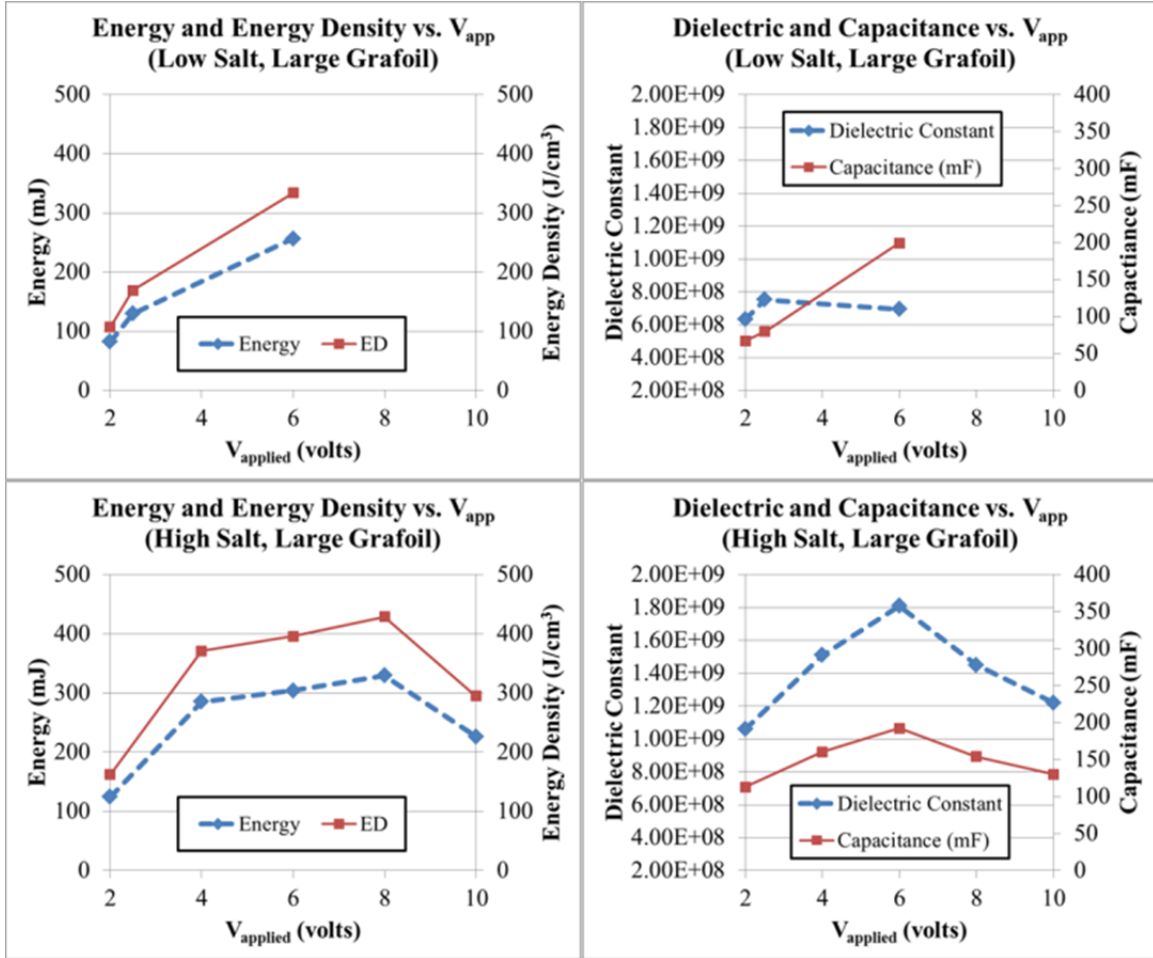
Figure 90. Energy density and maximum achieved voltage trends in a high salt NTSDM capacitor up to 10 volts.



Given the drop in capacitance and energy density against a marginal increase in maximum achieved voltage with 10.0 volts applied, some concern was raised regarding the possibility of an undesired chemical reaction in the capacitor at high applied voltages. As such, the same high salt capacitor was again charged and discharged at 4.0 volts applied. The recorded and calculated data from this final test are contained in the last row of Table 12. The results indicate that the capacitor was again rated at nearly the same value (165.9 mF) as that during the first 4.0 volt test (160.4 mF) with an improved energy density at 420 J/cm<sup>3</sup> that exceeded the theoretical value. It is worth noting that up to this point, this particular capacitor had been cycled over 49 times across a 4-week period. Hence, the material integrity of the capacitor seemed to withstand repeated low frequency cycling as well as disassembly and reassembly.

Finally, the results of the variation in applied voltage led to the conclusion that 6.0 volts was the optimum charge potential for subsequent NTSDM capacitor analysis. Although, Figure 91 clearly indicates the maximum energy density occurred with 8.0 volts applied, the peak capacitance occurred with 6.0 volts applied. Given the perceived breakdown of the governing relationship on capacitive energy storage at the lower value, 6.0 volts was selected as the optimum charge voltage at which all remaining capacitor analysis should be carried out.

Figure 91. Comparison of energy density and capacitance for both low salt (left) and high salt (right) capacitors as a function of the applied voltage on charge.



## B. DISCUSSION OF NTSDM CAPACITOR BEHAVIOR

It is important to again highlight the behavior of NTSDM capacitors, especially when it differs from that of COTS capacitors. The greatest behavioral distinction from electrostatic capacitors and supercapacitors, as discussed in the previous chapter, was the three distinct regions of capacitance on discharge. For some of the lesser performing capacitors with lower values of capacitance, three distinct linear regions were not as obvious when plotted as  $\ln(V/V_o)$  over time.

## **1. Three Region Capacitance**

In most cases, Region I should be considered the top voltage range over which an initial discharge transient was recorded. As the stored charge rapidly released back into the discharge circuit, the initial recorded voltages dropped rapidly. This initial rapid spike in electrical current would quickly be mitigated by the circuit load resistor causing a deceleration of discharge rate to steady state levels. This effect was also observed in the commercial supercapacitor during the circuit verification test. Accordingly, the energy delivered by Region I was usually inconsequential and for all practical purposes useless for any real world application.

For the majority of NTSDM capacitors tested, the Region II delivered the load share of energy and is the region by which each NTSDM capacitor was characterized. That is, the measured capacitances in Region II are considered the effective capacitances for the entire NTSDM capacitor. The bounds of Region II were found to be independent of capacitor design and tended from 2.0–1.7 volts down to 0.3–0.1 volts and are consistent with earlier NPS results [2]. Table 13 is a tabulation of the key NTSDM attributes and performance parameters for various capacitor designs listed in order of lowest to highest percent energy stored in Region II.

Table 13.

Ascending percent energy stored in Region II according to film thickness, electrode size and salt concentration; cell highlighting denotes affinity to higher salt, larger Grafoil, and magnitude of capacitance.

Film Thickness ( $\mu\text{m}$ )	Salt Concentration (wt%)	Grafoil Electrode Size ( $\text{mm}^2$ )	Average % ED in Region II	Average Region II Capacitance (mF)	Average Region II dielectric constant
3	16.7	96	43.0%	36.9	1.30E+08
8	16.7	25	51.5%	139.1	5.03E+09
3.8	33.3	25	58.1%	100.9	1.73E+09
11	16.7	25	59.9%	134.3	5.35E+09
8	16.7	25	64.5%	86.7	3.14E+09
9	16.7	48	71.6%	170.0	3.60E+09
8	16.7	96	76.8%	199.0	6.94E+08
3.8	16.7	25	77.0%	12.4	2.13E+08
3	33.3	96	78.8%	51.1	1.80E+09
8	16.7	25	80.1%	69.1	2.50E+09
8	33.3	96	88.7%	192.2	1.81E+09
6	33.3	96	89.3%	112.3	7.93E+08
9	16.7	48	89.7%	160.5	3.40E+09
27	33.3	96	90.4%	170.1	5.41E+09
8	33.3	96	90.4%	138.3	1.30E+09
8	16.7	25	91.2%	114.4	4.14E+09
18	33.3	25	92.1%	203.8	1.66E+10
18	33.3	96	93.1%	150.7	3.19E+09
7	33.3	25	96.4%	79.3	2.51E+09
18	16.7	96	97.0%	160.9	3.41E+09
17	16.7	25	97.3%	86.1	6.61E+09

For the purposes of this study, a “good” NTSDM capacitor was considered to have  $\geq 75\%$  of its stored energy in Region II. Any less, the NTSDM capacitor was considered suboptimum. As is qualitatively evident in Table 13, the majority of “good” capacitors were found to have larger sized Grafoil electrodes and/or higher electrolyte concentrations (cells highlighted in green). Similarly, the majority of those same capacitors tended to have anodic film thicknesses with 8  $\mu\text{m}$  or greater. Lastly, ten of the 15 “good” capacitors had capacitances above 100 mF, with seven of those greater than 150 mF. By comparison, four of the six suboptimum capacitors were calculated above 100 mF, with only one above 150 mF.

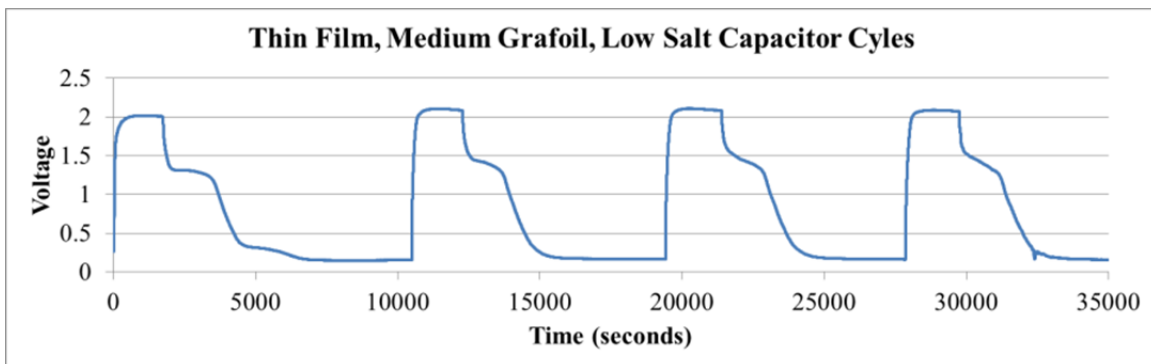
The last region of discharge was recorded down to a discharge rate less than 1 mV/minute or down to zero in the case of capacitor dry out. Corresponding capacitances of these regions were usually very high but cannot be considered useful or meaningful. The low voltage range of Region III meant the energy delivered and

subsequent energy density was negligible. Again, this is another indication why the Region II values are those that should characterize each NTSDM capacitor.

## 2. Pseudocapacitance Behavior

Some of the most compelling energy densities recorded were from NTSDM capacitors that exhibited a discharge profile with a knuckle or a slowing down between 1.3 and 1.0 volts. This phenomenon is considered to be caused by pseudocapacitance found in recent literature as discussed earlier. Within the bounds of this research, pseudocapacitance behavior was an accidental discovery. None of the selected control variables were chosen nor manipulated to create or mitigate the occurrence of pseudocapacitance. However, NTSDM capacitors that exhibited such behavior delivered nearly double the energy and accordingly had twice the energy density of similar NTSDM capacitors with normal discharge profiles. The discharge profile for a distinctive pseudocapacitance discharge looks like two different capacitor discharges stacked on top of one another causing a “stair step” appearance an example of which is presented in Figure 92.

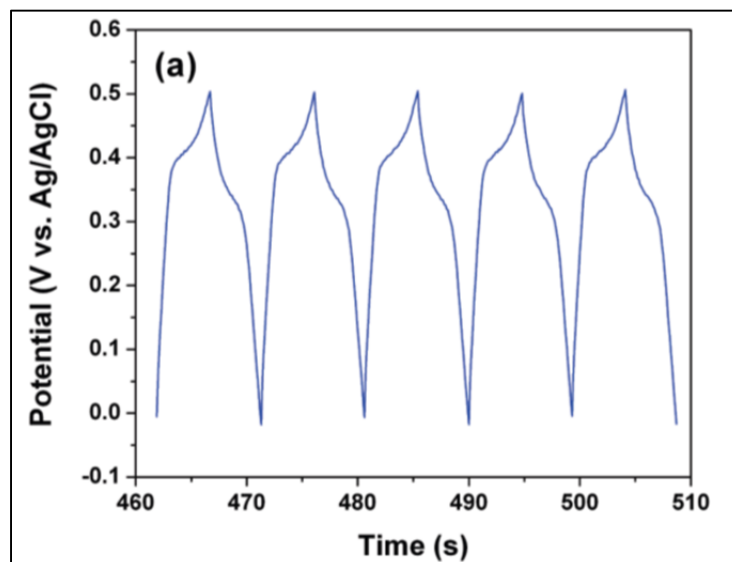
Figure 92. NTSDM capacitor discharge cycles with distinct behavior proposed to be a relic of pseudocapacitance.



Although recorded during a completely different experimental protocol, one study by Kim et al. [90] clearly demonstrated the typical voltage profile consistent with pseudocapacitive charge and discharge cycles. Presented here as Figure 93, the resulting “humps” on each discharge exhibit a similarity to those that are depicted in Figure 92.



Figure 93. Typical pseudocapacitance voltage profile consistent with high frequency, constant current cycling.



From J. Kim, K. Zhu, Y. Yan, C. L. Perkins and A. J. Frank, "Microstructure and pseudocapacitive properties of electrodes constructed of oriented NiO-TiO<sub>2</sub> nanotube arrays," *Nano Letters*, vol. 10, pp. 4099–4104, Sep. 2010.

Pseudocapacitance to the extreme of that depicted in Figure 92 was observed in only four out of the 32 individual capacitors tested (Ti\_022715 side B, Ti\_031515 side A, Ti\_061015\_AM, and Ti\_071415\_PM in Appendix C). In each case, a smaller 25 mm<sup>2</sup> Grafoil electrode was used and the presence of excess moisture within the capacitor was observed outside the Grafoil contact area. As can be intuitively derived, a reversal in trend between Region II and Region III capacitances was noted in these particular capacitors. Accordingly, the numerical integration of  $V^2/R$  data was the optimum method for calculating energy density. The argument could be made that fitting a linear interpolation to the  $\ln(V/V_o)$  data in these cases may not be wholly appropriate. However, as was pointed out in the earlier discussion of pseudocapacitance, such an estimate may point toward the distinct non-Faradaic capacitance proposed by Conway and Gileadi [54], but was not analyzed within the scope of this study.

In some of the remaining 28 capacitors, a very subtle relic of pseudocapacitance was faintly apparent such as in the case of the capacitor charge/discharge cycles presented in Figure 94. In fact, in most cases there was no trouble in linearly interpolating

three distinct regions of capacitance on  $\ln(V/V_0)$  plots, and was only obvious after plotting each discharge on the same plot such as in Figure 95. Again, the subtle cases of pseudocapacitance seemed to occur when excess moisture existed outside the contact area of the Grafoil electrode of any size.

Figure 94. NTSDM capacitor discharge cycles with subtle behavior proposed to be a relic of pseudocapacitance.

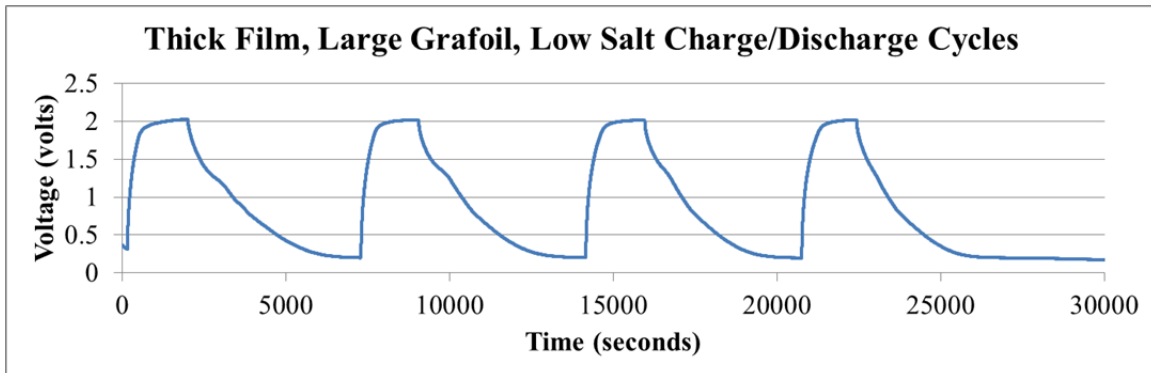
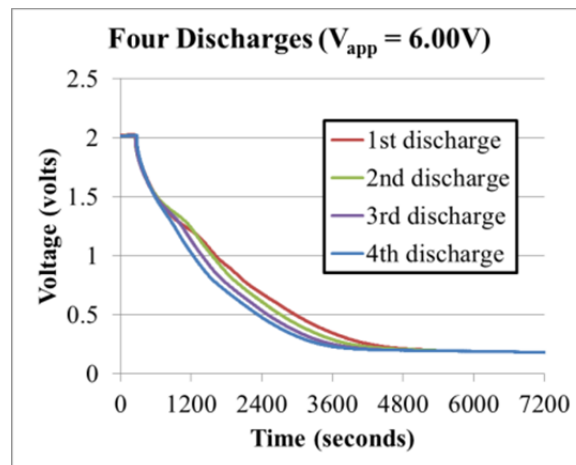


Figure 95. Same four discharges from Figure 94 overlaid on the same plot.



The onset or occurrence of pseudocapacitance must assume that a chemical reaction is taking place which may impact the capacitor's long term performance [88], [92]. The cases in this study which observed pseudocapacitance seemed to occur intermittently within select discharge cycles of the same assembled capacitor and due to

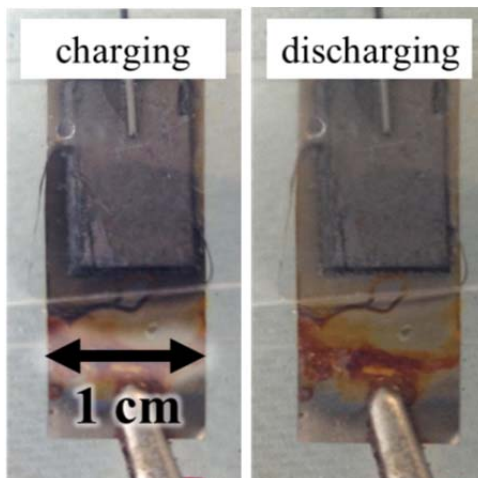
the voltage range over which the “humps” appear (1.0 to 1.3 volts) are believed to be associated with the breakdown of water.

The supposition that pseudocapacitance improves the NTSDM ability to store energy brings up a question. Why would the breakdown of water yield more energy storage? It takes energy to break down water, and gaining useful energy from hydrogen and oxygen assumes the existence of a recombination process. Therefore, the pseudocapacitance claim is based on the assumption that during charge at voltages much higher than the maximum operating, some hydrogen and oxygen are evolved, but recombine below 1.3 volts. The recombination effects the release of energy in both Faradaic and non-Faradaic form. Of course, evolved gases cannot recombine above 1.3 volts, because there is no thermodynamic driving force.

Energy storage processes like those in a battery rely on the travel of electrons and ions to the same electrode but by different paths. The net current traveling “through” the electrode is zero, so conclusive evidence of pseudocapacitance must conceive of a means by which hydrogen ions traverse through the water and meet their missing electrons to become  $\text{H}_2\text{O}$ . Within this scope of this research, the pseudocapacitive theory is put forward as an untested explanation of the non-capacitive like discharge profiles in certain NTSDM capacitors.

One final observation, noted during a few particular NTSDM capacitor tests, lends itself to the existence of a pseudocapacitance effect. Where excess salt water existed within the capacitor assembly, an electrolyte color change was noted during the charge portion of each capacitor cycle. While being charged, the excess NTSDM electrolyte was observed changing from clear to dark gray, and then slowly becoming clear again on discharge. Figure 96 is an attempt to pictorially capture this effect on one particular capacitor (Ti\_042415\_PM in Appendix B). While the specific cause of the color change and the associated chemical reaction are neither proposed nor explained within the scope of this research, the occurrence is mentioned and documented as colloquial proof of the existence of pseudocapacitance.

Figure 96. Depiction of the color change within the electrolyte observed during charge cycles.



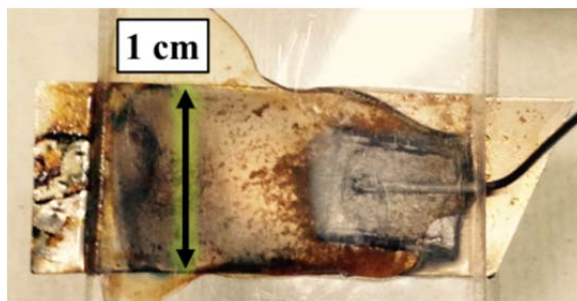
Should future studies attempt to completely avoid the onset of any pseudocapacitance effect during NTSDM capacitor discharge, it is proposed that additional care should be placed in removing excess electrolyte from the capacitor prior to testing. Furthermore, increased attention should be placed on controlling the level of moisture within the NTSDM capacitor containment so as to prevent the accumulation of water within the capacitor assembly. However, improving this aspect of the capacitor test protocol has implications beyond the mitigation or prevention of pseudocapacitance.

### **3. Noisy Charge or Discharge**

Another unexpected or undesired phenomena that was observed during capacitor testing was noise in the recorded charge/discharge signal and is believed to be closely linked to the onset of a corrosion reaction within the NTSDM in the presence of excessive salt water. In one particular case (Ti\_022715\_side\_B in Appendix C), the presence of corrosion byproducts was discovered to have formed between the alligator clip and the titanium foil. After assembling the capacitor, the excess electrolyte was not removed from the NTSDM assembly. Also, for the first time, the level of moisture was maintained by draping the box with a wet paper towel. However, the protocol overshot the desired humidity level within the containment and significant condensation formed on the interior walls of the containment as well as within the capacitor assembly. Aside from

the potential dilution of the electrolyte, it also caused water to accumulate and make contact with the Grafoil. The result is pictured in Figure 97. This condition was, of course, determined to be unacceptable and was in fact the first appearance of severe pseudocapacitance.

Figure 97. Depiction of the excessive accumulation of moisture and the presence of corrosion products (alligator clip has been removed).



The next experimental protocol was altered by incorporating a Grafoil “buffer between the alligator clip and the non-anodized portion of the titanium foil and is pictured in Figure 98. Eight charge/discharge cycles were completed on this particular capacitor (Ti\_031515\_side\_A in Appendix C). Because moisture content was closely monitored, the first four cycles had a smooth, saw-tooth appearance. However, the last four cycles were completed after an overnight discharge during which time the experiment was not monitored and the moisture again accumulated within the capacitor. The resulting plots contained noise and pseudocapacitance-like behavior on only the last four cycles and further confirmed a correlation between the excess moisture and pseudocapacitance.

Figure 98. NTSDM capacitor with Grafoil “buffer” and no excess moisture prior to experiment (left) and after an overnight discharge (right).

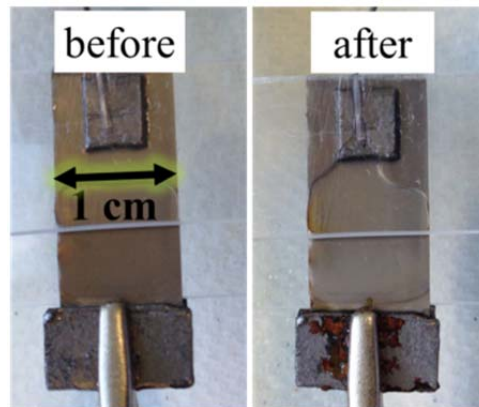
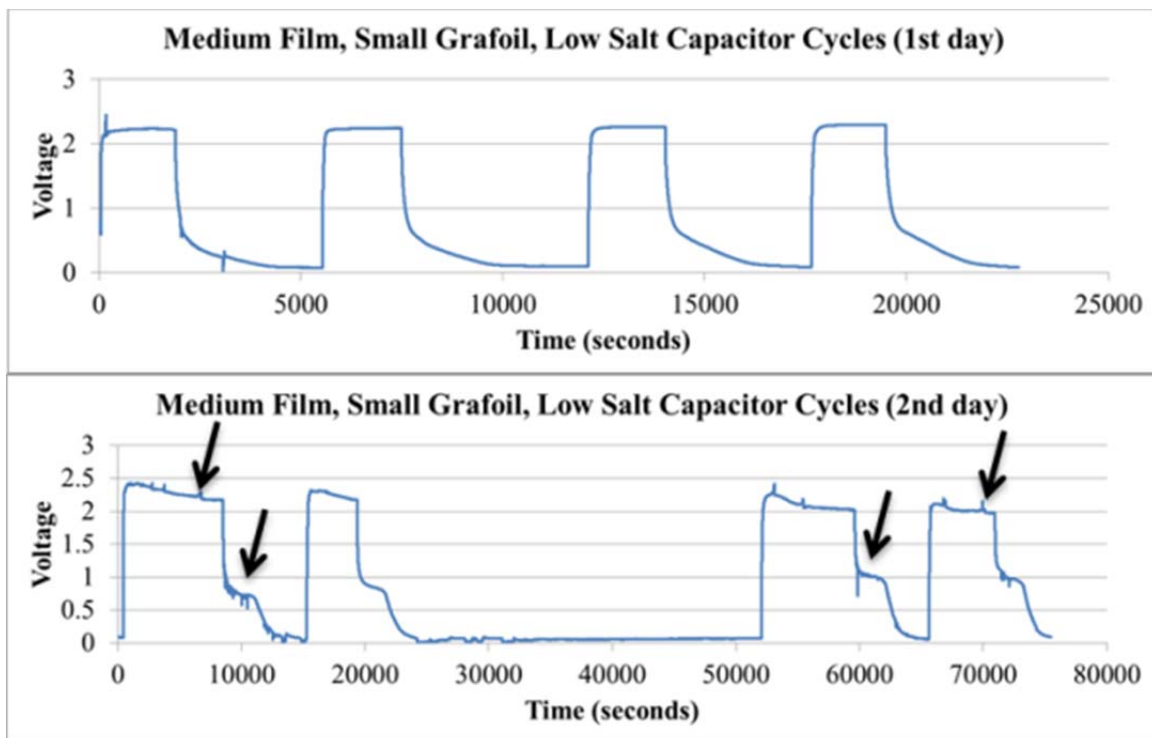


Figure 99. Last four charge/discharge cycles with noise (denoted by arrows) after accumulation of moisture within the capacitor and the appearance of rust on the Grafoil “buffer.”



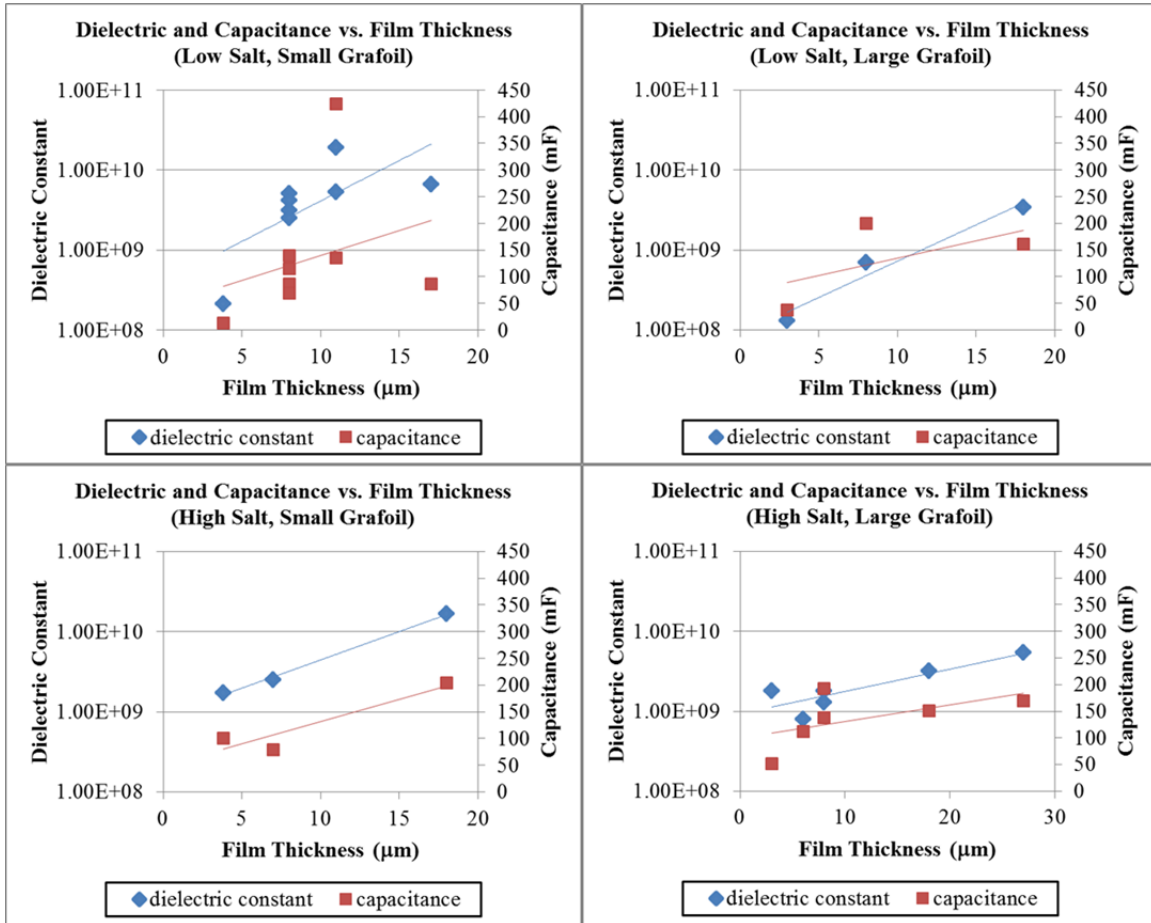
## **C. NTSDM CAPACITOR ANALYSIS**

The remaining capacitor analysis within this chapter is the ultimate correlation between NTSDM design characteristics and well-behaved capacitor performance. Namely, capacitance and energy density are the foci of analysis and discussion.

### **1. Capacitance and Dielectric Constant Analysis**

In general, measured capacitance tended to increase with film thickness. Figure 100 is all plotted values of capacitance and dielectric constants vs. film thickness according to specific NTSDM parameters and clearly depicts this common trend. Increasing capacitance with dielectric thickness is not the expected trend according to the mathematical relationship defined by Equation (2). If the mathematical relationship applies to NTSDM capacitors, this points to a significant increase in the relative permittivity of a magnitude much greater than the reduction caused by increasing thickness. That is, capacitance increases as a function of the higher dielectric constant more than it is reduced by the thicker dielectric. This supposition is qualitatively supported by comparing the relative slopes of each linear fits in Figure 100.

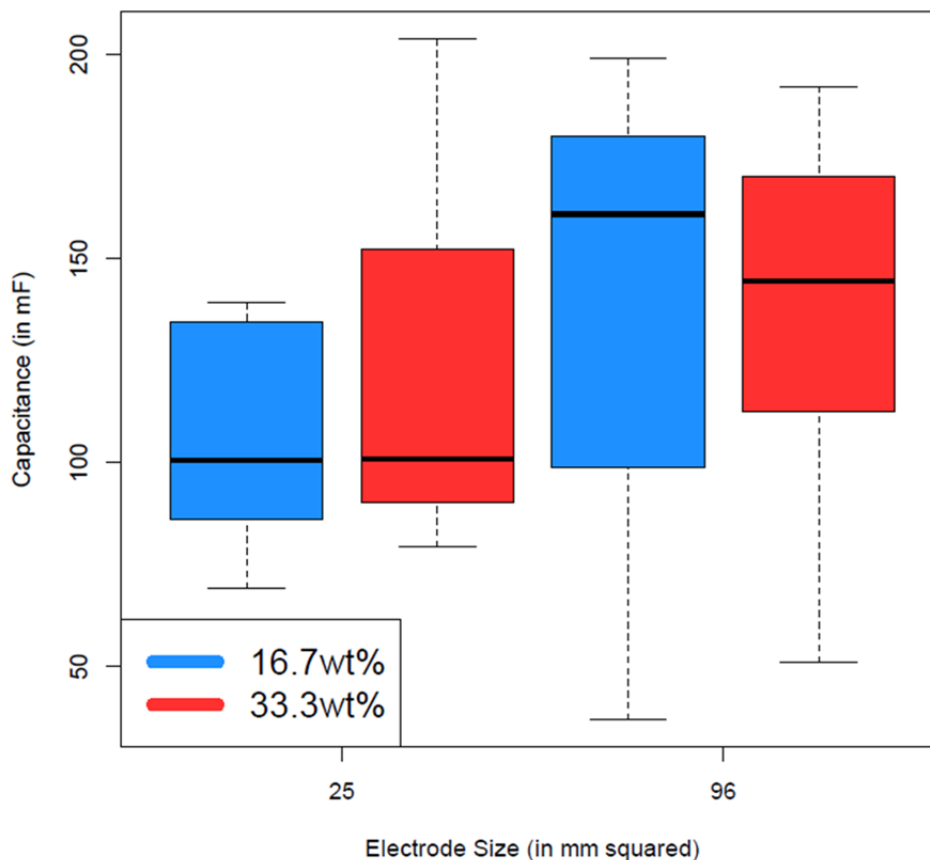
Figure 100. Dielectric constant and capacitance vs. film thickness for varying salt concentrations and electrode surface areas.



By inspection, Figure 100 suggests that electrode size and salt concentration do not strongly influence capacitance. However, the same data presented alternatively as a box and whisker plot in Figure 101, indicates that larger electrode surface areas result in higher values of capacitance. A correlation between salt concentration and capacitance is not readily apparent but may be inconclusive without recording more data points.



Figure 101. Box and whisker plot of capacitance vs. electrode size.



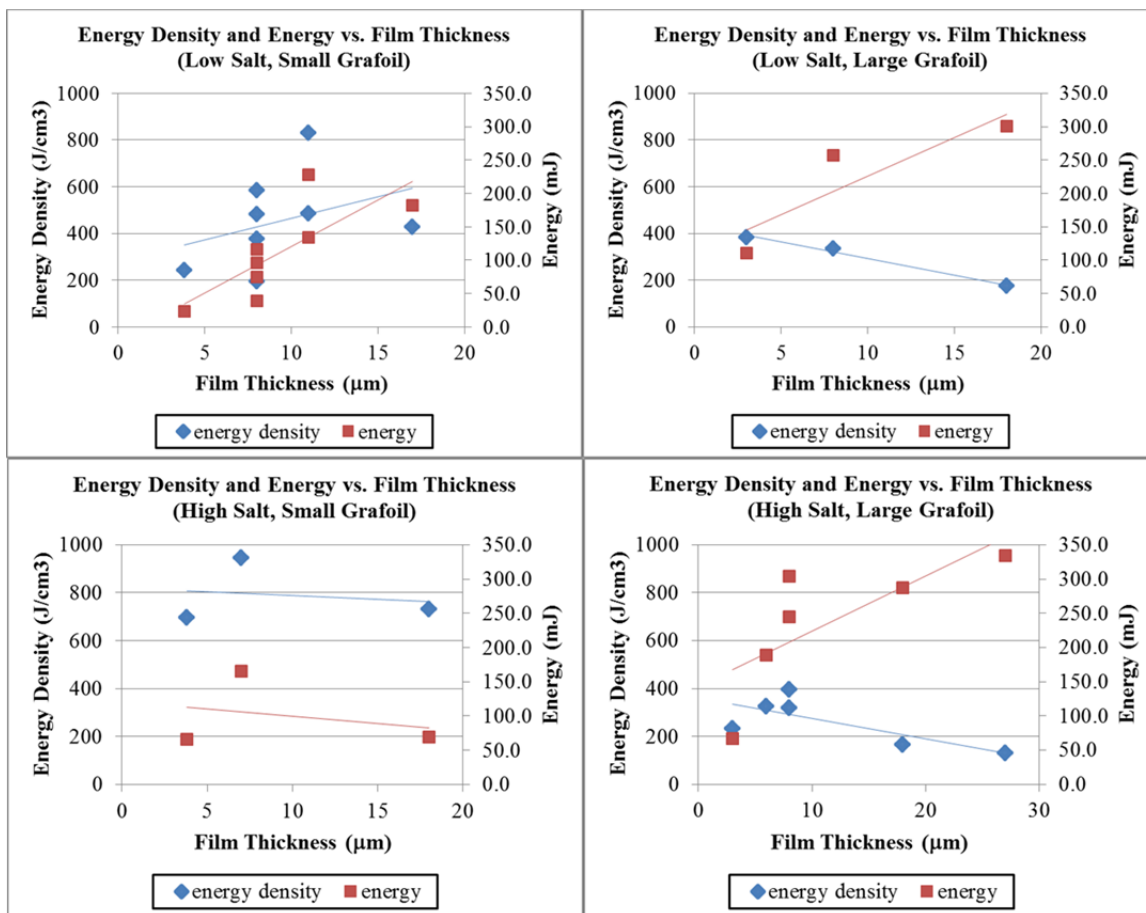
In summary, the highest recorded capacitances approached 200 mF while the highest recorded dielectric constants approached or exceed  $10^{10}$ . Recorded data indicated that thicker films certainly resulted in higher calculated values for capacitance as did larger electrode surface areas. These trends are also significant within the context of the correlation of energy storage and density in the next section.

## 2. Energy and Energy Density Analysis

Because calculated capacitance values, based on Equation (10), increase with dielectric thickness, then perhaps it is intuitive that so should the calculated energy stored. The energy released in each discharge, as reported within this discussion, was based on the numerical integration of discharging voltages in accordance with Equation (12). While the two are related, the two calculations are not mathematically dependent on

one another. Nonetheless, the average energy released in capacitor discharges was found to increase with film thickness and is evident in the plotted data in Figure 102.

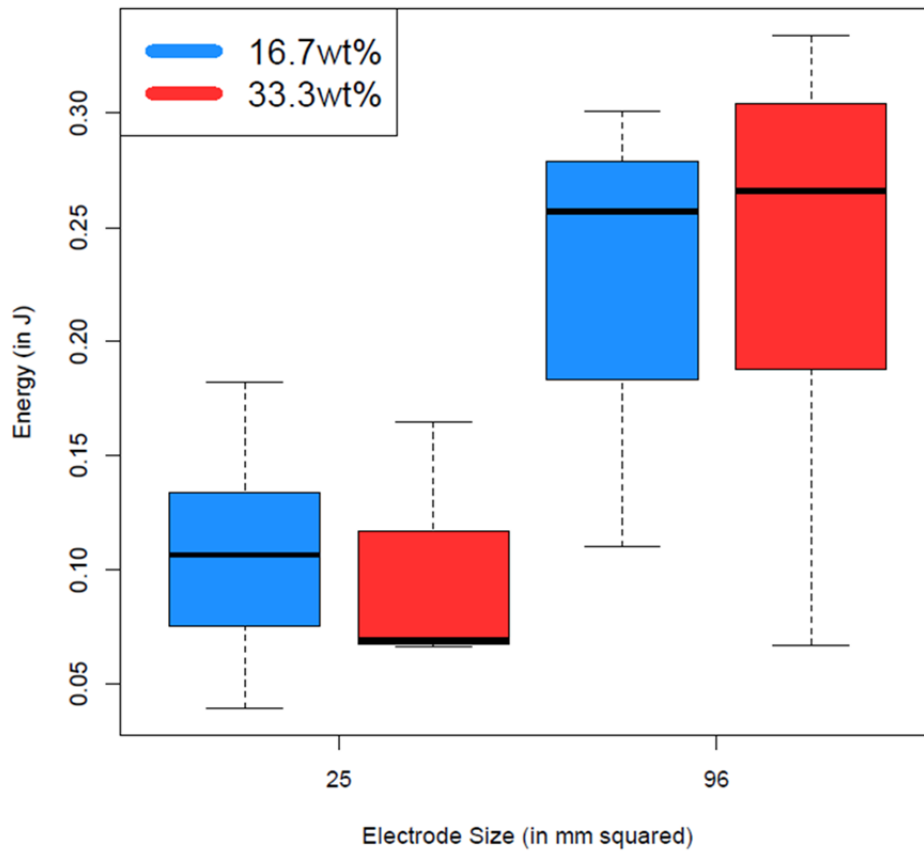
Figure 102. NTSDM capacitor energy and energy density vs. film thickness for varying salt concentrations and electrode surface areas.



From Figure 102 it is apparent that energy and energy density trends were not consistent across all capacitor designs. In fact, in the case of large Grafoil electrodes, energy density decreased with increasing film thickness. Hence, gains in energy stored due to increased capacitance were overcome by the increasing dielectric volume. In other words, increasing dielectric volume more dominantly affected the calculation of energy density over the increasing capacitance. The trend lines of opposite slope in the large Grafoil plots of Figure 102 very obviously demonstrate this phenomenon.

The average energy released on discharge across all capacitor designs was found to significantly increase with the larger electrode sizes. Figure 103 is an alternate presentation of the same data and obviously demonstrates this trend. In the case of the small electrode surface area capacitors, the highest recorded energy densities (up to  $831 \text{ J/cm}^3$ ) corresponded to some of the lowest quantities of energy stored in the entire study. This may indicate an artificial inflation of the energy density in the small Grafoil capacitors. In fact, results from the small surface area electrode were the only data to indicate the trend of increasing energy density with film thickness.

Figure 103. Box and whisker plot of energy vs. electrode size.



There is a possibility that the  $25 \text{ mm}^2$  Grafoil electrode placed atop the  $2.5 \text{ cm}^2$  anodized substrate achieves some polarization of the electrolyte contained in the anodic film outside of the Grafoil contact area. For this reason, it is proposed that the larger

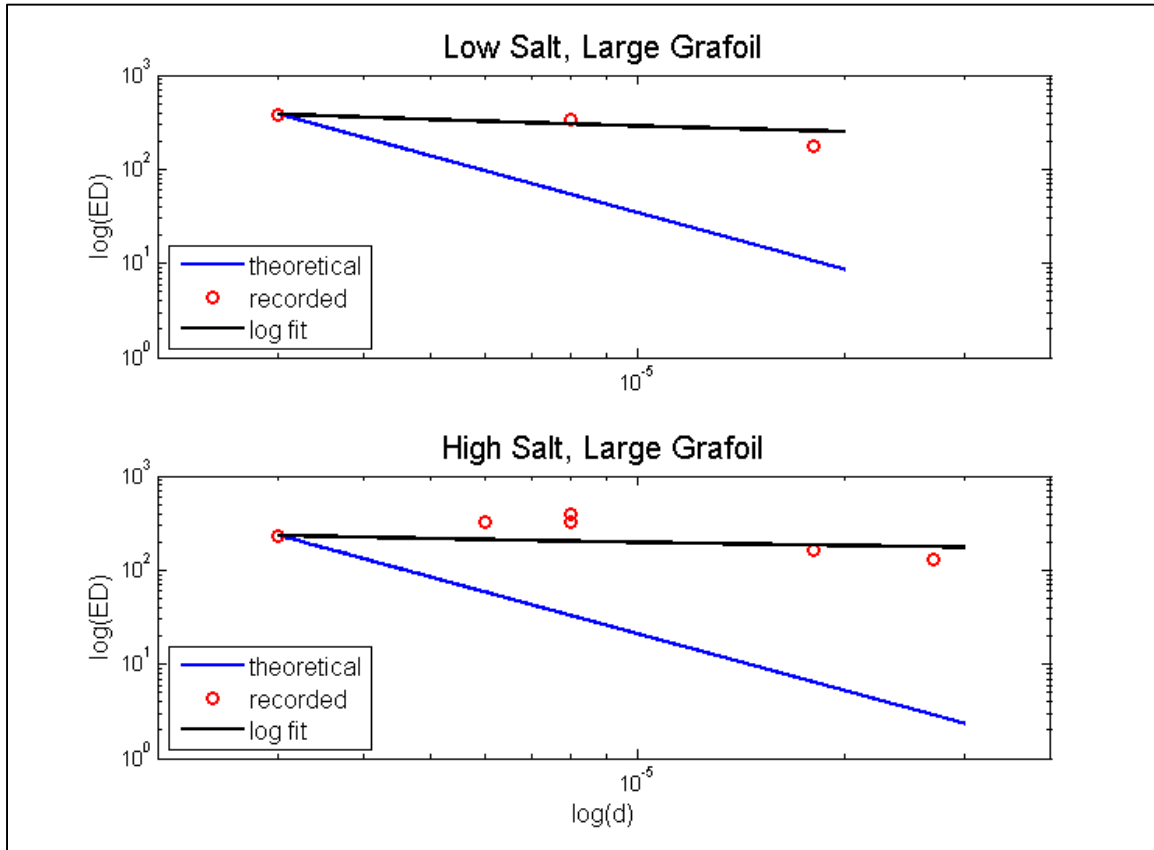
Grafoil electrode results presented more reliable and accurate measures of energy and energy density. The highest NTSDM capacitor energy density with a 6.0 volt charging voltage and large Grafoil electrode was found to be 396 J/cm<sup>3</sup>. However, as outlined in a previous section, 8.0 volt charging voltages repeatedly demonstrated energy densities greater than 400 J/cm<sup>3</sup> for similar capacitor designs.

The last correlation to consider is the apparent change in energy density due to a change in dielectric constant with increasing film thickness. The large Grafoil capacitors will be the only ones considered for the purpose of this discussion. Consider combining Equation (2) and Equation (10) in order to arrive at an expression that relates energy density as a function of dielectric thickness ( $d$ ) where dielectric volume is the electrode surface area multiplied by the dielectric thickness. The resulting relationship is expressed in Equation (16).

$$ED = \frac{1}{2} \epsilon_o \epsilon_r \left( \frac{V}{d} \right)^2 \quad (16)$$

By supposing the dielectric constant for the capacitors with 3  $\mu$ m films remained constant, the energy density according to Equation (16) was plotted logarithmically along with the actual recorded energy densities for both low and high salt capacitors. As is apparent in Figure 104, the slope of the theoretical calculation has a -2.0 slope as expected from Equation (16). However, the log fit of the actual low salt data has a -0.43 slope. Similarly, the high salt log fit data has a -0.36 slope. This suggests that NTSDM capacitor energy density is not a function of inverse thickness squared but rather inverse thickness raised to the 0.40 power. Again, this relationship assumes dielectric constant does not change for varying dielectric thickness which is not necessarily true.

Figure 104. Comparison of recorded and theoretical energy density vs. dielectric thickness.

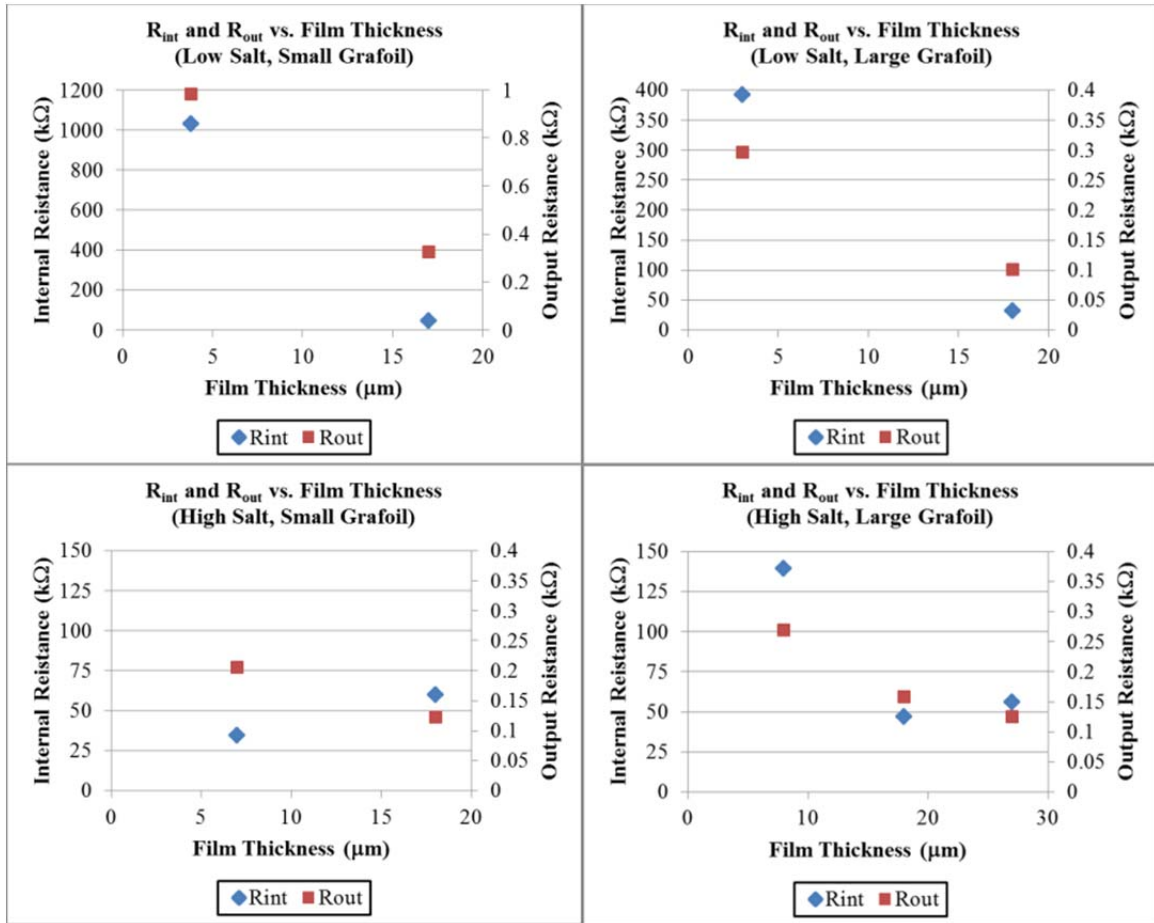


### 3. Leakage Resistance Analysis

NTSDM capacitors, like all other types of capacitors, were evaluated on their ability to hold a charge with no source or load applied. Figure 105 is a graphical comparison of the trend for  $R_{int}$  and  $R_{out}$  for varying NTSDM thicknesses and clearly demonstrates a correlation between dielectric thickness and leakage resistance. The data indicated thicker film capacitors, those with the highest capacitances, also had the lowest output and internal resistances. This is a desirable trend for output resistance, because optimum capacitor performance depends on the intended load receiving the bulk of stored energy. The higher the output resistance, the less energy is delivered to the load. Conversely, lower internal resistance is not a desired property, because the fully charged capacitor will discharge more rapidly even with no load applied.

For both cases, higher resistances were recorded with lower electrolyte salt concentrations and smaller the electrode surface areas. In terms of seeking an optimum capacitor design, this may indicate NTSDM with medium thickness achieve a balance between diminished output resistance and higher internal resistance. Truly, the desired performance characteristics will depend on the intended application.

Figure 105. NTSDM capacitor leakage resistances (internal and output) vs. film thickness for varying salt concentrations and electrode surface areas.



A fundamental understanding of the voltage divider circuit depicted in Figure 74 points to a relationship between the load resistor and apparent capacitance of the NTSDM device. That is, the larger the load resistor, the smaller the apparent capacitance. A larger load resistor relative to the measured output resistance will result in a larger fraction of

the internal energy drop within the capacitor. Thus, in the case of the large grafoil capacitors, the higher energy densities calculated for shorter film capacitors may be attributed to the changing output resistance specific to each NTSDM. This conclusion should be further investigated in future research.

#### **D. OTHER NTSDM DESIGNS CONSIDERED**

As alluded to in the previous chapter, deviations from the standard NTSDM capacitor assembly were considered during the course of this research. One capacitor test regimen used an alternate electrolytic salt, boric acid, while another test regimen replaced the Grafoil positive electrode with a nickel foil electrode. Both protocol deviations dramatically degraded their respective performances from that expected from the standard NaCl and Grafoil electrode assembly. The following sections will briefly review the results of those experiments as well as their relevance to the present work.

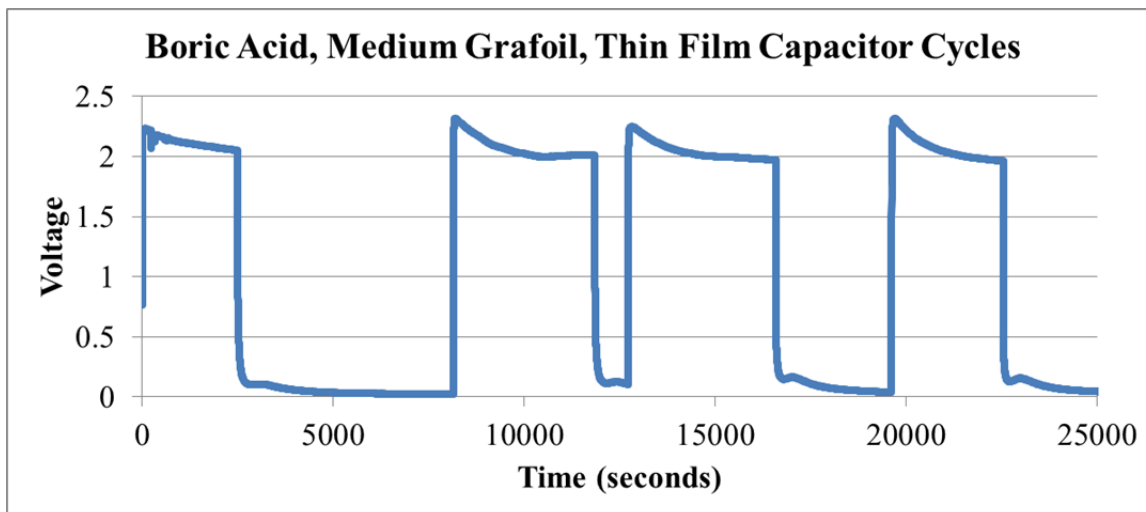
##### **1. Electrolyte Selection**

The primary reason for selecting NaCl as the NTSDM electrolytic salt was for its low cost and ready availability. A secondary incentive was the relatively high solubility of NaCl in water at 357 g/L [99] ensuring a good potential for strong dipole formation. Perhaps one drawback to using NaCl is due to the risk posed by the preferential nature of chlorides to dissolve active-passive metal oxides [100]. The standard protocol actually used two different qualities of NaCl during capacitor experimentation. Appendix C lists which capacitors used non-iodized table salt and which use commercially pure sodium chloride. The results of capacitor analyses between the two did not yield distinguishable differences in performance.

In an effort to legitimize the SDM hypothesis and broadly test the NTSDM model, the research considered boric acid as an alternate salt and was selected due to its use in previous SDM research at NPS [1]. Therefore, an NTSDM capacitor was assembled using a short film capacitor with 3.3 wt% of boric acid (approximately 70% of the solubility limit) as the operative electrolyte. The capacitor was tested over four charge/discharge cycles with an immediate indication of poor performance. As is obvious

in Figure 106, the resulting plot of voltage appears more like a step function than the desired smooth saw-tooth curve expected of a well-performing capacitor.

Figure 106. Boric acid NTSDM capacitor charge/discharge cycles.



Interestingly, the maximum voltage on charge is most obviously 2.2 to 2.3 volts. This does not necessarily help to resolve the basis for the maximum operating voltage of the NTSDM capacitor, but is another indication that it is a function of the  $\text{TiO}_2$  matrix rather than the breakdown of water. Due to the poor performance of the boric acid NTSDM capacitor, capacitor or energy were not calculated.

## 2. Positive Electrode Selection

Initially, Grafoil was selected as a convenient and inexpensive material for the positive electrode. As was discovered in previous research [2], the Grafoil electrode was demonstrated to be an effective capacitor electrode. After selecting NaCl as the primary NTSDM electrolyte, the decision was made to continue using Grafoil due to the high nobility of carbon in the galvanic series for saltwater [101]. Within the laboratory, there is no apparent disadvantage to using Grafoil to test NTSDM capacitor prototypes, but it may not be suited for a practical, commercial design.



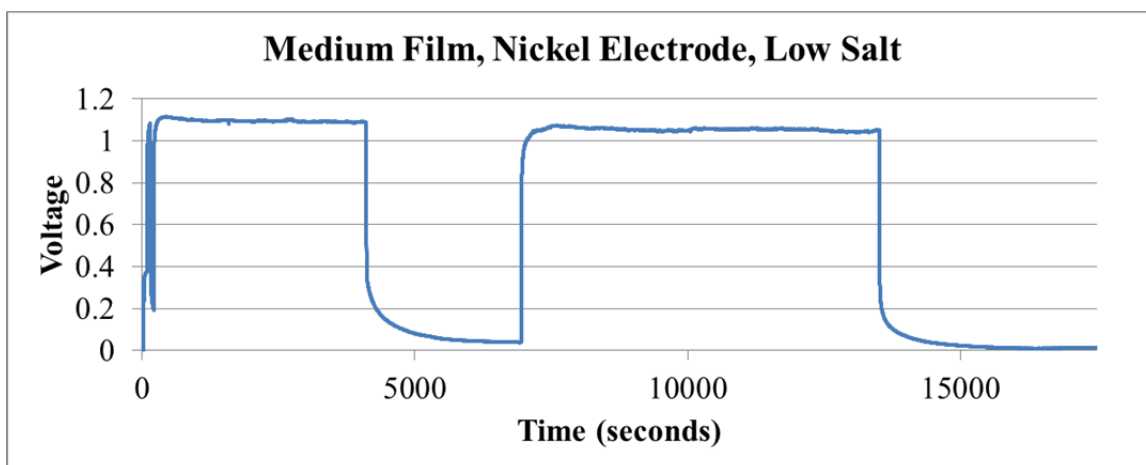
Accordingly, 0.05 mm thick nickel foil was selected as an alternate positive electrode also due to its relatively high nobility in the galvanic series for saltwater. The remaining NTSDM experimental parameters consisted of an 8  $\mu\text{m}$   $\text{TiO}_2$  anodic film filled with a 16.7 wt% saltwater electrolyte. The assembled capacitor is pictured in Figure 107.

Figure 107. Nickel electrode NTSDM capacitor prototype.



The ultimate performance of the nickel electrode capacitor prototype resulted in some of the lowest recorded values of capacitance and energy density at 44.6 mF and 3.3 J/cm<sup>3</sup>, respectively. Although the measured performance characteristics were unremarkable relative to other NTSDM capacitors, the maximum operating voltage changed significantly. Even though the capacitor was charged with 6.0 volts, it only reached 1.1 volts which indicated some type of dependence on the positive electrode material selection. Figure 108 clearly shows the maximum voltage on charge as well as the rapid discharges expected for a low capacitance value. On charge, it was believed that the nickel foil was undergoing some type of unwanted anodization as evidenced by the electrolyte color change also pictured in Figure 107. The poor performance of this capacitor did not warrant revisiting this design alteration.

Figure 108. Charge/discharge cycles for NTSDM with nickel electrode.



## E. SUMMARY

The regimen of capacitor testing yielded excellent performing dielectrics with dielectric constants up to five orders of magnitude better than  $\text{BaTiO}_3$ . Furthermore, NTSDMs were successfully employed in the creation of capacitors with unprecedented energy density. Undeniably, NTSDMs based on aqueous solutions of sodium chloride were employed to create capacitors with energy densities above  $400 \text{ J/cm}^3$ , more than ten times better than the energy density of the best commercial supercapacitors [3]. Throughout the course of study, parameters such as nanotube length and concentration of salt in the aqueous solution were found to have a profound, but predictable impact on NTSDM performance. Even more remarkable, it suggests these capacitors with improvement could rival the best lithium ion battery energy density.

### 1. Capacitance and Energy Density

Of initial significance, the results of the variation in applied voltage led to the conclusion that 6.0 volts was the optimum charge potential for subsequent NTSDM capacitor analysis. However, the maximum energy densities recorded in this research occurred with 8.0 volts applied, while the peak capacitances occurred with 6.0 volts applied. Regarding optimum capacitor design, the majority of “good” capacitors were found to have larger sized Grafoil electrodes and/or higher electrolyte concentrations and nearly half had capacitance values greater than 150 mF. Highlighted in Table 14, the

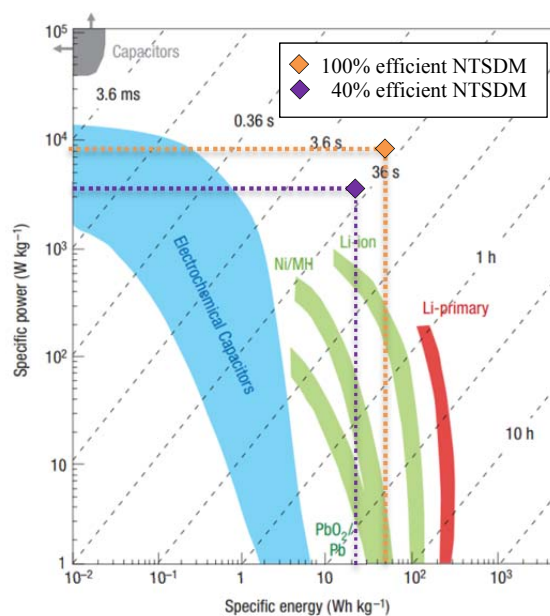
NTSDM capacitor performance metrics indicate nearly double the energy density from previous work at NPS [2]. What is more, specific capacitance is over seven times improved from the same study.

Table 14. Comparison of energy densities and specific energies between “best” ceramic capacitor technologies and NTSDM results.

<b>Dielectric Material</b>	<b>F/g</b>	<b>F/cm<sup>3</sup></b>	<b>J/g</b>	<b>J/cm<sup>3</sup></b>	<b>Ref.</b>
barium titanate nanocubes	--	--	--	5	[31]
barium strontium titanate nanowires	--	--	--	15	[32]
lead lanthanum zirconate titanate	--	--	--	22	[33]
Polymer	--	--	--	27	[34]
titanium nanotubes with NaNO <sub>3</sub> electrolyte	34	114	70	230	[2]
NTSDM with NaCl electrolyte	259	127	211	429	this research

The specific energy in units used in the Ragone plot of Figure 1, is approximately 58 Wh/kg. Supposing this energy is capable of being delivered in a rapid 30-second discharge, the corresponding specific power is slightly greater than 7,000 W/kg. This data point overlaid on the aforementioned Ragone plot provides a compelling argument for the promise of this technology, as is apparent in Figure 109. The assumption that the NTSDM capacitor can discharge all energy stored in 30 seconds or less is an idealized scenario. A more conservative assumption is to suppose that 40% of the stored energy, 23 Wh/kg, can be delivered in the same amount of time. In this case, the estimated specific power is slightly greater than 2,800 W/kg. Again, plotted Figure 109, this more realistic data point is still startlingly comparable proven LIB energy densities.

Figure 109. Best recorded NTSDM specific energy and theoretical specific power overlaid on a Ragone plot of various capacitor and LIB technologies.



After P. Simon and Y. Gogotsi, "Materials for electrochemical capacitors," *Nature Materials*, vol. 7, pp. 845–854, 2008.

## 2. Operating Voltage Limitations

As was proposed in earlier NPS research [1], the root cause of an operating voltage limitation should be considered inherent to each SDM, in this case, the  $\text{TiO}_2$  nanotube matrix with electrolyte. A select few capacitors exhibited behavior between 1.0 and 1.3 volts on discharge which seem connected to the breakdown of water. However, NTSDM capacitors repeatedly reached a maximum operating voltage above 2.0 volts certainly beyond that expected for the breakdown of water. Additionally, the capacitor which utilized boric acid instead of sodium chloride also experienced an operating limit just above 2.0 volts. By replacing the Grafoil electrode with nickel foil, the operating voltage was effectively cut in half to 1.1 volts. This may imply that the Grafoil electrode in some way influences the operating voltage limit, but is not a supportable claim with little data in this research to back it up.

THIS PAGE INTENTIONALLY LEFT BLANK

## **VI. SUMMARY OF FINDINGS**

This research thoroughly characterized and evaluated a new type of dielectric based on the SDM hypothesis. The study separately focused on two aspects of NSTDM capacitor technology. The first focus was on the creation of complex nanostructured oxide matrices. Procedures from existing work [2] were successfully modified to create simple and repeatable anodization techniques that produced suitable oxide films for use in an NTSDM capacitor. The second focus was to identify and manipulate controllable variables to optimize the performance of an NTSDM capacitor. In this regard, NTSDM capacitors reliably achieved energy densities greater than 10 times those previously reported for electrostatic capacitors and commercially available supercapacitors [3].

### **A. TUNGSTEN ANODIZATION RESULTS**

The intent of this portion of research was to develop a tungsten based structure useful as a dielectric material for NTSDM based capacitors. Specifically, the aim was to develop a simple anodization protocol for creating a densely packed hollow nanotube array on the tungsten foil similar to that generated on titanium (discussed in the next chapter). However, none of the protocols employed led to the formation of an array of hollow tungsten trioxide nanotubes. In all cases, the surface morphology consisted of a thin  $\text{WO}_3$  layer with nanoscale, irregularly oriented pores rather than the desired linearly organized nanotubes normal to the surface. The range of variables selected during the course of experimentation significantly impacted the uniformity and quality of this layer.

The resulting oxide films and degraded tungsten substrates were determined to be unsuitable for further capacitor experimentation. The success of the NTSDM model requires a uniform oxide film covering the entire metal substrate with no breaks in the oxide matrix integrity. Anodized tungsten specimens with nanofeatures were successfully produced using select combinations of voltage, time and electrolyte concentration. Ultimately, the resulting anodic oxide films were determined to be incompatible with their intended use as dielectric materials.

## **B. TITANIUM ANODIZATION RESULTS**

Again, the first aim of this research was to achieve the creation of a complex nanostructured oxide matrix for incorporation into an NTSDM capacitor. This study successfully developed and evaluated a standardized procedure for growing nanotube films of a predictable length and quality using titanium foil.

It is proposed that the low fluoride (0.25 wt%  $\text{NH}_4\text{F}$ , 2.75 wt% DIW), 40 volt, 4 hour anodization technique with a pre-anodization metal polish surface preparation produces the most well-formed nanotubes. In all cases, that particular recipe produced an anodic film with “clean” open tube top morphology and never exhibited problems with film delamination, and was an important consideration in selecting the optimum recipe for producing  $\text{TiO}_2$  nanotubes for NTSDM capacitors.

Thicker films require greater than 50 volts anodic potential in concert with higher fluoride concentrations, though complete anodization is a problem with thinner foil substrates. Surprisingly, this research discovered that increasing fluoride and water concentration without increasing voltage will actually shrink nanotube length. At higher fluoride concentrations, grass-like tube tops formed as a result of the more rigorous dissolution at all voltages. In case of medium film thicknesses, SEM analysis confirmed metal polishing the titanium foil substrate prior to anodization reduced the overall film thickness. Reusing the high fluoride electrolytes resulted in films 50% shorter than the electrolyte first use.

## **C. NTSDM CAPACITOR RESULTS**

This study successfully created 17 unique anodized titanium substrates that were found suitable for NTSDM capacitor analysis in all but two cases. The entire regimen of capacitor experimentation included 153 individual charge/discharge cycles over a 6-month period and yielded excellent performing dielectrics with dielectric constants up to five orders of magnitude better than  $\text{BaTiO}_3$ .

Of initial significance, the results of the variation in applied voltage led to the conclusion that 6.0 volts was the optimum charge potential for subsequent NTSDM capacitor analysis. However, the maximum energy densities recorded in this research

occurred with 8.0 volts applied, while the peak capacitances occurred with 6.0 volts applied. Regarding optimum capacitor designs, the majority of “good” capacitors were found to have larger sized Grafoil electrodes with measured capacitances greater than 150 mF.

NTSDMs were successfully employed in the creation of capacitors with unprecedented energy density. Undeniably, NTSDMs based on aqueous solutions of sodium chloride were employed to create capacitors with energy densities above  $400 \text{ J/cm}^3$ , more than ten times better than the energy density of the best commercial supercapacitors. Throughout the course of study, parameters such as nanotube length and concentration of salt in the aqueous solution were found to have a profound, but predictable impact on NTSDM performance. Even more remarkable, it suggests these capacitors with improvement could rival the best lithium ion battery energy density.



THIS PAGE INTENTIONALLY LEFT BLANK

## VII. RECOMMENDED FUTURE WORK

Continuation of this program with a focus on improving energy density suggests three main parameters to explore. First, can the ultimate operating voltage be increased by the use of a solvent with a higher breakdown voltage than water? This is important as total energy is proportional to voltage squared. Indeed, modern supercapacitors utilize organic solvents rather than water, which can operate effectively up to 5 volts. Second, does the identity of the metal impact the energy density? For example, is the ultimate effective voltage for the titanium based systems, approximately 2.1 volts, higher for other metals? Third, does the shape of the tubes, for example the diameter, impact the energy density?

Another issue of significance is the method of measuring capacitance and dielectric constant. The method employed here, determination of the RC time constant by discharge through a 10 k $\Omega$  resistor, actually returns very conservative values of capacitance. Indeed, 10 k $\Omega$  is a large fraction of the measured internal resistances, thus a significant fraction of the power was lost “inside” the capacitor. For a more realistic determination of the *effective* power density of these devices, discharges designed to release 90% of the charge within 10 seconds should be employed. Such analysis will be more relevant in assessing NTSDM capacitor value in systems such as laser weapons and rail guns and will clearly be based on a much smaller load resistance.

Many opportunities to continue this research also point in other directions. One aspect demanding additional consideration is identification of an alternate transition metal oxide besides TiO<sub>2</sub>. Subsequent work may revisit anodization of tungsten to refine the protocol until an oxide film suitable for incorporation as an NTSDM. An alternate route may involve the development of a simple aluminum anodization technique, though nanostructured tubes made of alumina would likely dissolve with the incorporation of chloride based electrolyte.

Notwithstanding the selection of an alternate metal substrate, there is potential for improving the TiO<sub>2</sub> anodization process to include post-anodization film alteration.

Namely, this study did not consider the potential impact of the grass-like tube morphology versus the seemingly well-performing capacitors with open tube tops. The proposed NTSDM model relies on the ability for all tubes to be filled with an electrolyte, so the grassing might interfere with this characteristic. Also, the use of thicker titanium substrates for thicker films anodization protocols should be considered. This may help to avoid the delamination problem by providing better structural support. An alternative to using thicker foil substrates is to insulate one side of the anode so the film only grows on one side.

Regarding the NTSDM electrolyte, consideration should be placed on finding an alternate, less volatile, electrolytic salt. Because the SDM hypothesis assumes higher salt concentrations create more dipoles, those with high solubility limits should primarily be considered while avoiding halide series ions. Because this study proposes the pseudocapacitance phenomenon is related to the breakdown of water, future work may necessarily incorporate non-aqueous electrolytes to eliminate pseudocapacitance. Conversely, there is potential for future studies to more closely study the onset of pseudocapacitance perhaps using it as an advantage in energy storage.

If low frequency charge/discharge cycling protocols are continued as a means to interpolate RC time constants, then expanding the experimental regimen to include 8.0 volt charge protocols may be beneficial for a number of reasons. First, the potential for higher energy densities exists with higher maximum operating voltages as well as higher values for capacitance. Second, for the purpose of experiment expediency, the required charge cycles are much shorter at higher voltages. Lastly, higher voltages achieving higher capacitances may help to prove the NTSDM hypothesis by showing stronger dipoles are formed under a stronger field.

An alternative to measuring capacitance should be considered. Specifically, energy dispersive impedance spectroscopy is commonly used in characterizing dielectric materials or validating capacitor performance. Incorporating a high frequency constant current charge/discharge cycling will allow for direct comparison to results found in related literature.

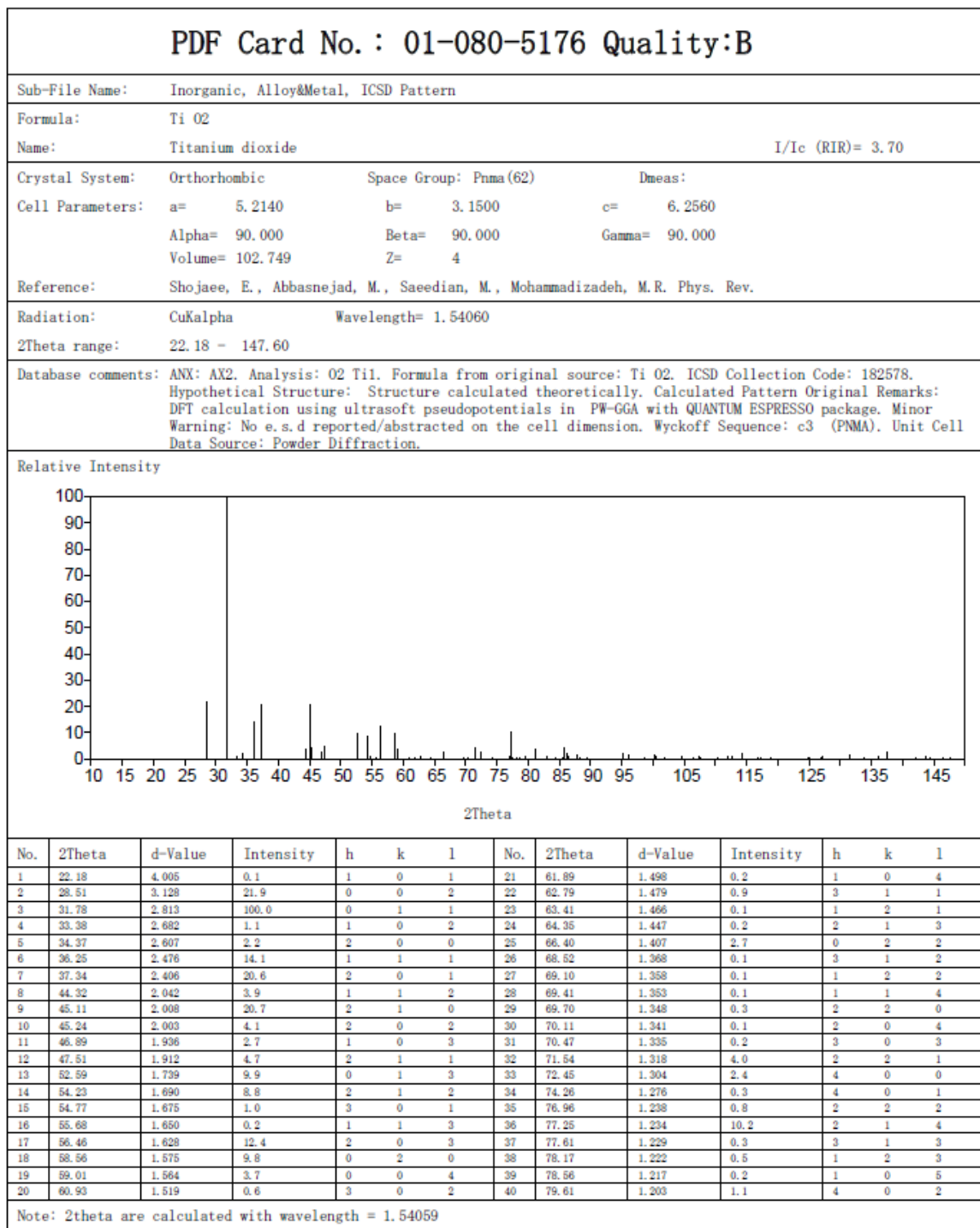
Based on the trends discovered during NTSDM characterization, future work should center around 8  $\mu\text{m}$  capacitors with high electrolyte concentrations and progressively larger positive electrode surface areas. This study uncovered evidence that anodized substrates may achieve some polarization of the electrolyte contained in the anodic film outside of the electrode contact area. For this reason, it is suggested that every effort should be made to maximize the contacted surface area in each NTSDM capacitor. Similarly, the best recipe for producing 8  $\mu\text{m}$  films should be used to anodize progressively larger pieces of titanium foil.

Finally, commercial production of an NTSDM capacitor should be a desired end state for this research. While results demonstrated compelling capacitances and spectacularly high energy densities for larger Grafoil electrodes, the actual commercial assembly for an NTSDM capacitor will likely rely on an easily repeatable and transportable assembly. Such a design would need to overcome the moisture control and sensitivity issues encountered during prototype testing in this work.

THIS PAGE INTENTIONALLY LEFT BLANK

## APPENDIX A

Figure 110. XRD powder diffraction pattern card (page 1 of 2).



2015-Jul-23 11:41:01 Page-1/2

Figure 111. XRD powder diffraction pattern card (page 2 of 2).

PDF Card No. : 01-080-5176 Quality:B													
No.	2Theta	d-Value	Intensity	h	k	l	No.	2Theta	d-Value	Intensity	h	k	l
41	81.28	1.183	3.8	4	1	1	101	142.19	0.814	0.3	4	0	6
42	82.97	1.163	0.8	0	1	5	102	143.62	0.811	1.2	4	3	1
43	84.35	1.147	0.3	3	2	1	103	144.33	0.809	0.6	6	1	2
44	85.49	1.135	0.2	1	1	5	104	146.56	0.804	0.3	0	3	5
45	85.75	1.132	4.5	2	2	3	105	147.60	0.802	0.4	6	0	3
46	86.14	1.128	2.0	2	0	5							
47	86.52	1.124	1.2	4	1	2							
48	87.91	1.110	1.5	0	2	4							
49	88.36	1.105	0.5	4	0	3							
50	89.57	1.093	0.2	3	2	2							
51	89.86	1.091	0.1	3	1	4							
52	90.41	1.085	0.1	1	2	4							
53	93.00	1.062	0.1	2	1	5							
54	95.22	1.043	2.0	4	1	3							
55	96.12	1.036	1.6	0	3	1							
56	96.99	1.029	0.1	5	0	1							
57	97.77	1.022	0.1	1	0	6							
58	97.94	1.021	0.1	2	2	4							
59	98.29	1.018	0.1	3	2	3							
60	98.65	1.016	0.2	1	3	1							
61	100.19	1.004	1.5	4	2	0							
62	100.58	1.001	0.9	4	0	4							
63	101.96	0.992	0.2	4	2	1							
64	102.27	0.989	0.1	5	0	2							
65	103.96	0.978	0.1	5	1	1							
66	104.54	0.974	0.9	2	3	0							
67	104.76	0.972	0.1	1	1	6							
68	105.44	0.968	0.1	2	0	6							
69	106.34	0.962	0.3	1	2	5							
70	107.34	0.956	0.9	4	2	2							
71	107.65	0.954	0.5	4	1	4							
72	109.40	0.944	0.1	5	1	2							
73	110.44	0.938	0.7	0	3	3							
74	110.88	0.935	0.1	3	2	4							
75	111.36	0.933	0.1	5	0	3							
76	111.86	0.930	0.8	2	3	2							
77	112.69	0.925	1.2	2	1	6							
78	114.27	0.917	1.8	2	2	5							
79	116.73	0.905	0.4	4	2	3							
80	117.16	0.903	0.4	4	0	5							
81	118.93	0.894	0.2	5	1	3							
82	119.97	0.890	0.1	3	3	1							
83	121.59	0.882	0.1	2	3	3							
84	121.97	0.881	0.1	1	0	7							
85	124.75	0.869	0.4	0	2	6							
86	125.17	0.868	0.7	4	1	5							
87	127.00	0.861	0.5	5	2	1							
88	127.25	0.860	1.0	1	3	4							
89	127.85	0.858	0.1	1	2	6							
90	129.00	0.853	0.1	3	2	5							
91	130.47	0.848	0.1	1	1	7							
92	131.45	0.845	1.4	2	0	7							
93	133.71	0.838	0.7	5	2	2							
94	133.85	0.837	0.7	6	0	2							
95	136.17	0.830	1.0	6	1	1							
96	137.40	0.827	2.4	2	3	4							
97	137.91	0.825	0.1	3	3	3							
98	138.12	0.825	0.1	2	2	6							
99	140.79	0.818	0.1	4	3	0							
100	141.26	0.817	0.1	2	1	7							
Note: 2theta are calculated with wavelength = 1.54059													

## APPENDIX B

Table 15. Table of results for all anodization experiments.

specimen designator	Substrate Material	Anodization Voltage (V)	Anodization Time (hours)	Ethylene Glycol Solution	Electrolyte use 1st or 2nd	Surface Preparation	Film Thickness (μm)
Ti_012815	titanium foil (0.05 mm)	40	2	0.25 wt% NH <sub>4</sub> F 2.75wt% DIW	1st	ethyl alcohol rinse	6
Ti_022715	titanium foil (0.05 mm)	40	4	0.25 wt% NH <sub>4</sub> F 2.75wt% DIW	1st	metal polish & ethyl alcohol rinse	9
Ti_031515	titanium foil (0.05 mm)	40	4	0.25 wt% NH <sub>4</sub> F 2.75wt% DIW	1st	ethyl alcohol rinse	11
Ti_040815	titanium foil (0.05 mm)	40	4	0.25 wt% NH <sub>4</sub> F 2.75wt% DIW	1st	metal polish & ethyl alcohol rinse	8
Ti_042415 AM	titanium foil (0.05 mm)	40	4	0.25 wt% NH <sub>4</sub> F 2.75wt% DIW	1st	metal polish & ethyl alcohol rinse	8
Ti_042415 PM	titanium foil (0.05 mm)	40	4	0.25 wt% NH <sub>4</sub> F 2.75wt% DIW	2nd	metal polish & ethyl alcohol rinse	8
Ti_052115 AM	titanium foil (0.05 mm)	40	1	0.25 wt% NH <sub>4</sub> F 2.75wt% DIW	1st	metal polish & ethyl alcohol rinse	3
Ti_052115 PM	titanium foil (0.05 mm)	40	1	0.25 wt% NH <sub>4</sub> F 2.75wt% DIW	2nd	metal polish & ethyl alcohol rinse	3.8
Ti_061015 AM	titanium foil (0.05 mm)	60 (first 15min) 40 (remainder)	4	0.6 wt% NH <sub>4</sub> F 3.5wt% DIW	1st	metal polish & ethyl alcohol rinse	13 - 18
Ti_061015 PM	titanium foil (0.05 mm)	50	4	0.6 wt% NH <sub>4</sub> F 3.5wt% DIW	2nd	metal polish & ethyl alcohol rinse	18
Ti_061215	titanium foil (0.05 mm)	50 (first 2 hrs) 40 (remainder)	4	0.6 wt% NH <sub>4</sub> F 3.5wt% DIW	1st	ethyl alcohol rinse	26 - 39
Ti_071415 AM	titanium foil (0.05 mm)	40	4	0.6 wt% NH <sub>4</sub> F 3.5wt% DIW	1st	ethyl alcohol rinse	6
Ti_071415 PM	titanium foil (0.05 mm)	45	4	0.6 wt% NH <sub>4</sub> F 3.5wt% DIW	2nd	ethyl alcohol rinse	7
Ti_071515 AM	titanium foil (0.05 mm)	50	4	0.6 wt% NH <sub>4</sub> F 3.5wt% DIW	1st	ethyl alcohol rinse	27
Ti_071515 PM	titanium foil (0.05 mm)	50	4	0.6 wt% NH <sub>4</sub> F 3.5wt% DIW	2nd	ethyl alcohol rinse	18
Ti_072215	titanium foil (0.05 mm)	50	4	0.6 wt% NH <sub>4</sub> F 3.5wt% DIW	1st	ethyl alcohol rinse	27
Ti_073215	titanium foil (0.05 mm)	50	4	0.6 wt% NH <sub>4</sub> F 3.5wt% DIW	2nd	ethyl alcohol rinse	17



THIS PAGE INTENTIONALLY LEFT BLANK

## APPENDIX C

Table 16. Table of results from NTSDM capacitor experiments (page 1 of 2).

specimen designator	Film Thickness ( $\mu\text{m}$ )	Capacitor Electrolyte	Concent ration (wt%)	Grafoil Electrode Size ( $\text{mm}^2$ )	Applied Voltage (V)	Peak Charge Voltage (V)	No. of Cycles	Average Energy Density ( $\text{J cm}^{-3}$ )	Highest Energy Density ( $\text{J cm}^{-3}$ )	Average Energy Dispersed (Joules)	Average % Energy Region II	Average Capacitance Region II (mF)	Average dielectric constant	Internal Resistance (k $\Omega$ )	Output Resistance (k $\Omega$ )
Ti_012815	6	boric acid	3.33	46	6	2.01	4	14.7	14.9	0.004	29.7%	3.7	5.41E+07	not measured	
Ti_022715 side A	9	pure sodium chloride	16.7	48	6	2.29	5	615	692	0.266	89.7%	160.5	3.40E+09	not measured	
Ti_022715 side B	9	pure sodium chloride	16.7	48	6	2.08	4	793	829	0.343	71.6%	170.0	3.60E+09		
Ti_031515 side A	11	table salt (NaCl)	16.7	25	6	2.29	8	831	1018	0.229	79.7%	423.3	1.91E+10	not measured	
Ti_031515 side B	11	table salt (NaCl)	16.7	25	6	2.30	8	486	789	0.134	59.9%	134.3	5.35E+09		
Ti_040815 side A	8	table salt (NaCl)	16.7	25	6	2.30	8	376	492	0.075	80.1%	69.1	2.50E+09	not measured	
	8	table salt (NaCl)	16.7	25	6	2.17	2	583	583	0.117	91.2%	114.4	4.14E+09		
Ti_040815 side B	8	table salt (NaCl)	16.7	25	6	2.15	2	193	197	0.039	51.5%	139.1	5.03E+09		
	8	table salt (NaCl)	16.7	75 (nickel foil)	6	1.10	2	3.5	5.1	0.002	64.8%	44.6	5.38E+08	not measured	
Ti_042415 AM - side A	8	pure sodium chloride	16.7	25	6	2.34	8	482	646	0.096	64.5%	86.7	3.14E+09		
	8	pure sodium chloride	16.7	96	6	2.11	8	334	439	0.257	76.8%	199.0	6.94E+08		
	8	pure sodium chloride	16.7	96	2	1.62	3	107	116	0.082	83.1%	67.3	6.33E+08		
	8	pure sodium chloride	16.7	96	2.5	1.77	2	169	178	0.130	82.8%	79.8	7.52E+08		
	8	pure sodium chloride	33.3	96	2	1.61	3	162	168	0.124	82.8%	112.7	1.06E+09	not measured	
Ti_042415 AM - side B	8	pure sodium chloride	33.3	96	4	2.00	4	371	381	0.285	96.1%	160.4	1.51E+09		
	8	pure sodium chloride	33.3	96	6	2.13	6	396	509	0.304	88.7%	192.2	1.81E+09		
	8	pure sodium chloride	33.3	96	8	2.15	4	429	469	0.329	81.9%	153.8	1.45E+09		
	8	pure sodium chloride	33.3	96	10	2.19	5	295	307	0.227	83.2%	130.1	1.22E+09		
	8	pure sodium chloride	33.3	96	4	2.11	6	420	530	0.323	94.7%	165.9	1.56E+04		

Table 17.

Table of results from NTSDM capacitor experiments (page 2 of 2).

specimen designator	Film Thickness ( $\mu\text{m}$ )	Capacitor Electrolyte	Concent ration (wt%)	Grafoil Electrode Size ( $\text{mm}^2$ )	Applied Voltage (V)	Peak Charge Voltage (V)	No. of Cycles	Average Energy Density ( $\text{J}/\text{cm}^3$ )	Highest Energy Density ( $\text{J}/\text{cm}^3$ )	Average Energy Dispersed (Joules)	Average % Energy Region II	Average Region II Capacitance (mF)	Average dielectric constant	Internal Resistance (k $\Omega$ )	Output Resistance (k $\Omega$ )
Ti_042415 PM	8	pure sodium chloride	33.3	96	4	1.96	3	267	274	0.205	89.6%	115.4	1.09E+09	not measured	
	8	pure sodium chloride	33.3	96	6	2.02	4	319	367	0.245	90.4%	138.3	1.30E+09	139.3	0.270
Ti_052115 AM	3	pure sodium chloride	33.3	96	6	2.19	4	233	247	0.067	78.8%	51.1	1.80E+09	not measured	
	3	pure sodium chloride	16.7	96	6	2.07	5	383	471	0.110	43.0%	36.9	1.30E+08	391.6	0.296
Ti_052115 PM	3.8	pure sodium chloride	33.3	25	6	1.98	5	697	1051	0.066	58.1%	100.9	1.73E+09	not measured	
	3.8	pure sodium chloride	16.7	25	6	2.02	5	243	286	0.023	77.0%	12.4	2.13E+08	1030.5	0.985
Ti_061015 AM	18	pure sodium chloride	33.3	25	6	2.09	5	730	745	0.069	92.1%	203.8	1.66E+10	60.0	0.122
Ti_061015 PM	18	pure sodium chloride	33.3	96	6	2.02	5	166	175	0.287	93.1%	150.7	3.19E+09	46.7	0.158
Ti_061215	39	specimen unsuitable for capacitor experimentation-----													
Ti_071415 AM	6	pure sodium chloride	33.3	96	6	2.12	3	327	338	0.188	89.3%	112.3	7.93E+08	not measured	
Ti_071415 PM	7	pure sodium chloride	33.3	25	6	2.05	6	944	1019	0.165	96.4%	79.3	2.51E+09	34.6	0.206
Ti_071515 AM	27	pure sodium chloride	33.3	96	6	2.08	5	129	148	0.334	90.4%	170.1	5.41E+09	55.9	0.125
Ti_071515 PM	18	pure sodium chloride	16.7	96	6	2.03	5	174	193	0.301	97.0%	160.9	3.41E+09	31.9	0.101
Ti_072215	27	specimen unsuitable for capacitor experimentation-----													
Ti_073215	17	pure sodium chloride	16.7	25	6	2.25	5	429	492	0.182	97.3%	86.1	6.61E+09	43.8	0.324

## LIST OF REFERENCES

- [1] S. Fromille, "Novel concept for high dielectric constant composite electrolyte dielectrics," M.S. thesis, Dept. Mech. Eng., Naval Postgraduate School, Monterey, CA, 2013.
- [2] F. Quintero and J. Phillips, "Tube-super dielectric materials: electrostatic capacitors with energy density greater than 200 Jcm<sup>-3</sup>," unpublished.
- [3] Maxwell Technologies, Inc. (2015). Maxwell Technologies ultracapacitors product comparison matrix. San Diego, CA. [Online]. Available: [http://www.maxwell.com/images/documents/Product\\_Comparison\\_Matrix\\_3000489\\_2.pdf](http://www.maxwell.com/images/documents/Product_Comparison_Matrix_3000489_2.pdf).
- [4] G. Arlt and D. Hennings, "Dielectric properties of fine-grained barium titanate ceramics," *J. Appl. Phys.*, vol. 58, pp. 1619–1625, Apr. 1985.
- [5] S. Roundy, P. K. Wright, and J. M. Rabaey, *Energy Scavenging for Wireless Sensor Networks: With Special Focus on Vibrations*. Boston: Kluwer Academic Publishers, 2004.
- [6] F. J. Q. Cortes and J. Phillips, "Novel materials with effective super dielectric constants for energy storage," *J Electron Mater*, vol. 44, pp. 1367–1376, Jan. 2015.
- [7] S. Fromille and J. Phillips, "Super Dielectric Materials," *Materials*, vol. 7, pp. 8197–8212, Dec. 2014.
- [8] T. B. Atwater, P. J. Cygan and F. C. Leung, "Man portable power needs of the 21st century: I. Applications for the dismounted soldier. II. Enhanced capabilities through the use of hybrid power sources," *J. Power Sources*, vol. 91, pp. 27–36, Nov. 2000.
- [9] J. Harper. (2014, Dec. 11). Navy authorized to use new laser weapon for self-defense on USS Ponce. [Online]. Available: <http://www.stripes.com/news/us/navy-authorized-to-use-new-laser-weapon-for-self-defense-on-uss-ponce-1.318735>.
- [10] K. Osborn. (2015, Apr. 24). Navy will test its electromagnetic rail gun aboard DDG 1000. [Online]. Available: <http://www.military.com/daily-news/2015/04/14/navy-will-test-its-electromagnetic-rail-gun-aboard-ddg-1000.html>.

- [11] H. Lessig. (2015, Jun. 10). Carrier Gerald R. Ford's electromagnetic catapult begins testing. [Online]. Available: <http://www.military.com/daily-news/2015/06/10/carrier-gerald-r-fords-electromagnetic-catapult-begins-testing.html>.
- [12] M. R. Doyle, D. J. Samuel, T. Conway, and R. R. Klimowski, "Electromagnetic aircraft launch system-EMALS," *Magnetics, IEEE Transactions On*, vol. 31, pp. 528–533, Jan. 1995.
- [13] I. McNab and F. Beach, "Naval railguns," *Magnetics, IEEE Transactions On*, vol. 43, pp. 463–468, Jan. 2007.
- [14] The Department of the Navy's energy goals. (n.d.). Department of the Navy. [Online]. Available: [http://www.navy.mil/features/Navy\\_EnergySecurity.pdf](http://www.navy.mil/features/Navy_EnergySecurity.pdf). Accessed Sep. 8, 2015.
- [15] N. Doerry and J. Amy, "Functional decomposition of a medium voltage DC integrated power system," presented at ASNE Shipbuilding in Support of the Global War on Terrorism Symposium, Biloxi, MS, Apr. 2008.
- [16] L. J. Petersen, D. J. Hoffman, J. P. Borraccini, and S. B. Swindler, "Next-generation power and energy: Maybe not so next generation," *Nav. Eng. J.*, vol. 122, pp. 59–74, Feb. 2011.
- [17] J. Caley, "private communication," Aug. 2015.
- [18] I. J. Cohen, D. Wetz, C. Storm, and J. Heinzl, "Impact of a hybrid energy storage module on power quality of a fossil fuel generator," in *ANSE Electric Machines Technology Symposium*, Villanova University, Philadelphia, PA, May 2014.
- [19] L. Lu, X. Han, J. Li, J. Hua, and M. Ouyang, "A review on the key issues for lithium-ion battery management in electric vehicles," *J. Power Sources*, vol. 226, pp. 272–288, Mar. 2013.
- [20] I. J. Cohen, J. P. Kelley, D. Wetz, and J. Heinzl, "Evaluation of a hybrid energy storage module for pulsed power applications," *Plasma Science, IEEE Transactions On*, vol. 42, pp. 2948–2955, Jan. 2014.
- [21] C. Cavas. (2014, Dec. 12). A closer look at the "Modified LCS". [Online]. Available: <http://intercepts.defensenews.com/2014/12/a-closer-look-at-the-modified-lcs/>.
- [22] M. Gunzinger and C. Dougherty, (2013, Feb. 12) Changing the game: The promise of directed-energy weapons. Center for Strategic and Budgetary Assessments. Washington, DC. Available: <https://info.aiaa.org/tac/pc/DESPC/Shared%20Documents/Forms/AllItems.aspx>.

- [23] J. Skillings. (2012, February 27). Airborne laser hits the off switch. [Online]. Available: <http://www.cnet.com/news/airborne-laser-hits-the-off-switch/>.
- [24] Littoral Combat Ship class – LCS. (n.d.). Department of the Navy. [Online]. Available: <http://www.public.navy.mil/surfor/pages/LittoralCombatShips.aspx#.Vb-yYflVhBd>
- [25] A. J. Bard and L. R. Faulkner, *Electrochemical Methods: Fundamentals and Applications*. Hoboken, NJ: John Wiley & Sons, 2001.
- [26] M. Brain and C. Bryant. (2007, Sep. 17). “How capacitors work.” [Online]. Available: <http://electronics.howstuffworks.com/capacitor.htm>.
- [27] M. Jayalakshmi and K. Balasubramanian, “Simple capacitors to supercapacitors-an overview,” *Int.J.Electrochem.Sci*, vol. 3, pp. 1196–1217, Sep. 2008.
- [28] C. Dunn, R. Bolon, A. Alwan, and A. Stirling, “A scanning electron microscope study of etched aluminum foil for electrolytic capacitors,” *J. Electrochem. Soc.*, vol. 118, pp. 381–390, Sep. 1971.
- [29] S. Wada, H. Yasuno, T. Hoshina, S. Nam, H. Kakemoto, and T. Tsurumi, “Preparation of nm-sized barium titanate fine particles and their powder dielectric properties,” *Japanese Journal of Applied Physics*, vol. 42, pp. 6188, Sep. 2003.
- [30] A. R. Von Hippel, *Dielectric Materials and Applications*. Artech House on Demand, 1954.
- [31] S. S. Parizi, A. Mellinger, and G. Caruntu, “Ferroelectric barium titanate nanocubes as capacitive building blocks for energy storage applications,” *ACS Applied Materials & Interfaces*, vol. 6, pp. 17506–17517, Oct. 2014.
- [32] H. Tang and H. A. Sodano, “Ultra high energy density nanocomposite capacitors with fast discharge using Ba<sub>0.2</sub>Sr<sub>0.8</sub>TiO<sub>3</sub> nanowires,” *Nano Letters*, vol. 13, pp. 1373–1379, Mar. 2013.
- [33] S. Tong, B. Ma, M. Narayanan, S. Liu, and R. Koritala, U. Balachandran and D. Shi, “Lead lanthanum zirconate titanate ceramic thin films for energy storage,” *ACS Applied Materials & Interfaces*, vol. 5, pp. 1474–1480, Feb. 2013.
- [34] O. L. Smith, Y. Kim, M. Kathaperumal, M. R. Gadinski, M. Pan, Q. Wang, and J. W. Perry, “Enhanced permittivity and energy density in neat poly (vinylidene fluoride-trifluoroethylene-chlorotrifluoroethylene) terpolymer films through control of morphology,” *ACS Applied Materials & Interfaces*, vol. 6, pp. 9584–9589, Jun. 2014.

- [35] R. Kötzt and M. Carlen, "Principles and applications of electrochemical capacitors," *Electrochim. Acta*, vol. 45, pp. 2483–2498, Jul. 2000.
- [36] A. Burke, "Ultracapacitors: Why, how, and where is the technology," *J. Power Sources*, vol. 91, pp. 37–50, Aug. 2000.
- [37] H. Lee, N. Byamba-Ochir, W. Shim, M. Balathanigaimani, and H. Moon, "High-performance super capacitors based on activated anthracite with controlled porosity," *J. Power Sources*, vol. 275, pp. 668–674, Nov. 2014.
- [38] Z. Sui, Y. Meng, P. Xiao, Z. Zhao, Z. Wei, and B. Han, "Nitrogen-doped graphene aerogels as efficient supercapacitor electrodes and gas adsorbents," *ACS Applied Materials & Interfaces*, vol. 7, pp. 1431–1438, Dec. 2014.
- [39] W. Zhang, H. Lin, H. Kong, H. Lu, Z. Yang, and T. Liu, "High energy density PbO<sub>2</sub>/activated carbon asymmetric electrochemical capacitor based on lead dioxide electrode with three-dimensional porous titanium substrate," *Int. J. Hydrogen Energy*, vol. 39, pp. 17153–17161, Sep. 2014.
- [40] D. Wei, M. R. Scherer, C. Bower, P. Andrew, T. Ryhänen, and U. Steiner, "A nanostructured electrochromic supercapacitor," *Nano Letters*, vol. 12, pp. 1857–1862, Mar. 2012.
- [41] D. Ghosh and C. K. Das, "Hydrothermal growth of hierarchical Ni<sub>3</sub>S<sub>2</sub> and Co<sub>3</sub>S<sub>4</sub> on a reduced graphene oxide hydrogel Ni foam: a high-energy-density aqueous asymmetric supercapacitor," *ACS Applied Materials & Interfaces*, vol. 7, pp. 1122–1131, Jan. 2015.
- [42] B. You, J. Jiang and S. Fan, "Three-dimensional hierarchically porous all-carbon foams for supercapacitor," *ACS Applied Materials & Interfaces*, vol. 6, pp. 15302–15308, Aug. 2014.
- [43] M. Ghidui, M. R. Lukatskaya, M. Zhao, Y. Gogotsi, and M. W. Barsoum, "Conductive two-dimensional titanium carbide clay with high volumetric capacitance," *Nature*, Aug. 2014.
- [44] S. Murali, N. Quarles, L. L. Zhang, J. R. Potts, Z. Tan, Y. Lu, Y. Zhu, and R. S. Ruoff, "Volumetric capacitance of compressed activated microwave-expanded graphite oxide (a-MEGO) electrodes," *Nano Energy*, vol. 2, pp. 764–768, Feb. 2013.
- [45] A. Boisset, J. Jacquemin, and M. Anouti, "Physical properties of a new deep eutectic solvent based on lithium bis [(trifluoromethyl) sulfonyl] imide and n-methylacetamide as superionic suitable electrolyte for lithium ion batteries and electric double layer capacitors," *Electrochim. Acta*, vol. 102, pp. 120–126, Apr. 2013.

- [46] M. Bai, L. Bian, Y. Song, and X. Liu, "Electrochemical codeposition of vanadium oxide and polypyrrole for high-performance supercapacitor with high working voltage," *ACS Applied Materials & Interfaces*, vol. 6, pp. 12656–12664, Jul. 2014.
- [47] C. Liu, Z. Yu, D. Neff, A. Zhamu, and B. Z. Jang, "Graphene-based supercapacitor with an ultrahigh energy density," *Nano Letters*, vol. 10, pp. 4863–4868, Nov. 2010.
- [48] Y. Qiu, G. Li, Y. Hou, Z. Pan, H. Li, W. Li, M. Liu, F. Ye, X. Yang, and Y. Zhang, "Vertically aligned carbon nanotubes on carbon nanofibers: a hierarchical three-dimensional carbon nanostructure for high-energy flexible supercapacitors," *Chemistry of Materials*, vol. 27, pp. 1194–1200, Jan. 2015.
- [49] Y. Xu, Z. Lin, X. Zhong, X. Huang, N. O. Weiss, Y. Huang, and X. Duan, "Holey graphene frameworks for highly efficient capacitive energy storage," *Nature Communications*, vol. 5, Aug. 2014.
- [50] B. E. Conway, "Transition from 'supercapacitor' to 'battery' behavior in electrochemical energy storage," *J. Electrochem. Soc.*, vol. 138, pp. 1539–1548, Jun. 1991.
- [51] Low voltage electrolytic capacitor, by H. I. Becker (1957, Jul. 23). Patent Number US2800616A [Online]. Available: <https://www.google.com/patents/US2800616>.
- [52] Double layer capacitors with polymeric electrolyte, by J. C. Currie, L. F. DiFranco and P. D. Bennett (1988, Mar. 8). Patent Number US4730239 [Online]. Available: <https://www.google.com/patents/US4730239>.
- [53] B. Conway, V. Birss, and J. Wojtowicz, "The role and utilization of pseudocapacitance for energy storage by supercapacitors," *J. Power Sources*, vol. 66, pp. 1–14, Apr. 1998.
- [54] B. Conway and E. Gileadi, "Kinetic theory of pseudo-capacitance and electrode reactions at appreciable surface coverage," *Transactions of the Faraday Society*, vol. 58, pp. 2493–2509, Mar. 1962.
- [55] R. Ulrich, L. Schaper, D. Nelms, and M. Leftwich, "Comparison of paraelectric and ferroelectric materials for applications as dielectrics in thin film integrated capacitors," *International Journal of Microcircuits and Electronic Packaging*, vol. 23, pp. 172–181, Apr. 2000.
- [56] J. C. Anderson, *Dielectrics*. New York: Reinhold Publishing Corporation, 1964, pp. 49–54.



- [57] C. W. Lai, "Photocatalysis and photoelectrochemical properties of tungsten trioxide nanostructured films," *Scientific World Journal*, vol. 2014, pp. 843587, Mar. 2014.
- [58] Y. Nah, A. Ghicov, D. Kim, and P. Schmuki, "Enhanced electrochromic properties of self-organized nanoporous WO<sub>3</sub>," *Electrochemistry Communications*, vol. 10, pp. 1777–1780, Sep. 2008.
- [59] M. Schneider, K. Kremmer, S. Weidmann, and W. Fürbeth, "Interplay between parameter variation and oxide structure of a modified PAA process," *Surf. Interface Anal.*, vol. 45, pp. 1503–1509, Mar. 2013.
- [60] A. M. Abd-Elnaiem and A. Gaber, "Parametric study on the anodization of pure aluminum thin film used in fabricating nano-pores template," *Int.J.Electrochem.Sci*, vol. 8, pp. 9741–9751, Jul. 2013.
- [61] S. Ho, C. Su, C. Cheng, S. Kathirvel, C. Li, and W. Li, "Preparation, characterization, and application of titanium nano-tube array in dye-sensitized solar cells," *Nanoscale Research Letters*, vol. 7, pp. 1–9, Dec. 2012.
- [62] M. Yang, N. K. Shrestha, and P. Schmuki, "Thick porous tungsten trioxide films by anodization of tungsten in fluoride containing phosphoric acid electrolyte," *Electrochemistry Communications*, vol. 11, pp. 1908–1911, Aug. 2009.
- [63] E. A. Kneer, C. Raghunath, S. Raghavan, and J. S. Jeon, "Electrochemistry of chemical vapor deposited tungsten films with relevance to chemical mechanical polishing," *J. Electrochem. Soc.*, vol. 143, pp. 4095–4100, Sep. 1996.
- [64] R. S. Lillard, G. S. Kanner, and D. P. Butt, "The nature of oxide films on tungsten in acidic and alkaline solutions," *J. Electrochem. Soc.*, vol. 145, pp. 2718–2725, Apr. 1998.
- [65] N. De Tacconi, C. Chenthamarakshan, G. Yogeewaran, A. Watcharenwong, R. De Zoysa, N. Basit, and K. Rajeshwar, "Nanoporous TiO<sub>2</sub> and WO<sub>3</sub> films by anodization of titanium and tungsten substrates: influence of process variables on morphology and photoelectrochemical response," *The Journal of Physical Chemistry B*, vol. 110, pp. 25347–25355, Oct. 2006.
- [66] N. Mukherjee, M. Paulose, O. K. Varghese, G. Mor, and C. A. Grimes, "Fabrication of nanoporous tungsten oxide by galvanostatic anodization," *J. Mater. Res.*, vol. 18, pp. 2296–2299, Jul. 2003.
- [67] L. Iglesias-Rubianes, P. Skeldon, G. Thompson, K. Shimizu, and H. Habazaki, "Influence of current density in anodizing of an Al–W alloy," *Corros. Sci.*, vol. 43, pp. 2217–2227, Jul. 2001.

- [68] H. Tsuchiya and P. Schmuki, "Self-organized high aspect ratio porous hafnium oxide prepared by electrochemical anodization," *Electrochemistry Communications*, vol. 7, pp. 49–52, Dec. 2004.
- [69] H. Tsuchiya, J. M. Macak, I. Sieber, L. Taveira, A. Ghicov, K. Sirotina, and P. Schmuki, "Self-organized porous WO<sub>3</sub> formed in NaF electrolytes," *Electrochemistry Communications*, vol. 7, pp. 295–298, Feb. 2005.
- [70] J. Schultze, M. Lohrengel and D. Ross, "Nucleation and growth of anodic oxide films," *Electrochim. Acta*, vol. 28, pp. 973–984, Feb. 1983.
- [71] H. Tsuchiya and P. Schmuki, "Thick self-organized porous zirconium oxide formed in H<sub>2</sub>SO<sub>4</sub>/NH<sub>4</sub>F electrolytes," *Electrochemistry Communications*, vol. 6, pp. 1131–1134, Sep. 2004.
- [72] H. Zheng, A. Z. Sadek, K. Latham, and K. Kalantar-Zadeh, "Nanoporous WO<sub>3</sub> from anodized RF sputtered tungsten thin films," *Electrochemistry Communications*, vol. 11, pp. 768–771, Feb. 2009.
- [73] S. Iijima, "Helical microtubules of graphitic carbon," *Nature*, vol. 354, pp. 56–58, Nov. 1991.
- [74] C. N. R. Rao and M. Nath, "Inorganic nanotubes," *Dalton Transactions*, pp. 1–24, Mar. 2003.
- [75] Y. Feldman, E. Wasserman, D. J. Srolovitz, and R. Tenne, "High-rate, gas-phase growth of MoS<sub>2</sub> nested inorganic fullerenes and nanotubes," *Science*, vol. 267, pp. 222–225, Jan. 1995.
- [76] R. Tenne, L. Margulis, M. e. a. Genut, and G. Hodes, "Polyhedral and cylindrical structures of tungsten disulphide," *Nature*, vol. 360, pp. 444–446, Dec. 1992.
- [77] Y. Xia, P. Yang, Y. Sun, Y. Wu, B. Mayers, B. Gates, Y. Yin, F. Kim, and H. Yan, "One-dimensional nanostructures: synthesis, characterization, and applications," *Adv Mater*, vol. 15, pp. 353–389, Mar. 2003.
- [78] H. Nakamura and Y. Matsui, "Silica gel nanotubes obtained by the sol-gel method," *J. Am. Chem. Soc.*, vol. 117, pp. 2651–2652, Mar. 1995.
- [79] P. Hoyer, "Formation of a titanium dioxide nanotube array," *Langmuir*, vol. 12, pp. 1411–1413, Mar. 1996.
- [80] M. Remškar, "Inorganic nanotubes," *Adv Mater*, vol. 16, pp. 1497–1504, Dec. 2004.
- [81] J. L. G. Fierro, *Metal Oxides: Chemistry and Applications*. Boca Raton, FL: CRC Press, 2006, pp. 2–25.

- [82] D. V. Bavykin, J. M. Friedrich, and F. C. Walsh, "Protonated titanates and TiO<sub>2</sub> nanostructured materials: synthesis, properties, and applications," *Adv Mater*, vol. 18, pp. 2807–2824, Oct. 2006.
- [83] P. Schmuki and S. Virtanen, *Electrochemistry at the Nanoscale*. New York: Springer Science & Business Media, 2009, pp v-1.
- [84] P. Roy, S. Berger, and P. Schmuki. "TiO<sub>2</sub> nanotubes: synthesis and applications," *Angewandte Chemie International Edition* 50(13), pp. 2904–2939. Mar. 2011.
- [85] H. Xu, G. Vanamu, Z. Nie, H. Konishi, R. Yeredla, J. Phillips, and Y. Wang, "Photocatalytic oxidation of a volatile organic component of acetaldehyde using titanium oxide nanotubes," *Journal of Nanomaterials*, vol. 2006, pp. 23–23, Jan. 2006.
- [86] U. Diebold, "The surface science of titanium dioxide," *Surface Science Reports*, vol. 48, pp. 53–229, Jan. 2003.
- [87] J. Huang, K. Zhang, and Y. Lai, "Fabrication, modification, and emerging applications of TiO<sub>2</sub> nanotube arrays by electrochemical synthesis: a review," *International Journal of Photoenergy*, vol. 2013, Jul. 2013.
- [88] K. Zhu, Q. Wang, J. Kim, A. A. Pesaran, and A. J. Frank, "Pseudocapacitive lithium-ion storage in oriented anatase TiO<sub>2</sub> nanotube arrays," *The Journal of Physical Chemistry C*, vol. 116, pp. 11895–11899, May 2012.
- [89] S. Kaneco, Y. Chen, P. Westerhoff, and J. C. Crittenden, "Fabrication of uniform size titanium oxide nanotubes: impact of current density and solution conditions," *Scr. Mater.*, vol. 56, pp. 373–376, Dec. 2006.
- [90] J. Kim, K. Zhu, Y. Yan, C. L. Perkins and A. J. Frank, "Microstructure and pseudocapacitive properties of electrodes constructed of oriented NiO-TiO<sub>2</sub> nanotube arrays," *Nano Letters*, vol. 10, pp. 4099–4104, Sep. 2010.
- [91] H. Fang, M. Liu, D. Wang, T. Sun, D. Guan, F. Li, J. Zhou, T. Sham, and H. Cheng, "Comparison of the rate capability of nanostructured amorphous and anatase TiO<sub>2</sub> for lithium insertion using anodic TiO<sub>2</sub> nanotube arrays," *Nanotechnology*, vol. 20, pp. 225701, May 2009.
- [92] M. Salari, K. Konstantinov, and H. K. Liu, "Enhancement of the capacitance in TiO<sub>2</sub> nanotubes through controlled introduction of oxygen vacancies," *Journal of Materials Chemistry*, vol. 21, pp. 5128–5133, Feb. 2011.
- [93] M. Paulose, H. E. Prakasham, O. K. Varghese, L. Peng, K. C. Popat, G. K. Mor, T. A. Desai, and C. A. Grimes, "TiO<sub>2</sub> nanotube arrays of 1000  $\mu\text{m}$  length by anodization of titanium foil: phenol red diffusion," *The Journal of Physical Chemistry C*, vol. 111, pp. 14992–14997, Sep. 2007.

- [94] H. E. Prakasam, K. Shankar, M. Paulose, O. K. Varghese, and C. A. Grimes, "A new benchmark for TiO<sub>2</sub> nanotube array growth by anodization," *The Journal of Physical Chemistry C*, vol. 111, pp. 7235–7241, Apr. 2007.
- [95] P. Roy, D. Kim, K. Lee, E. Spiecker, and P. Schmuki, "TiO<sub>2</sub> nanotubes and their application in dye-sensitized solar cells," *Nanoscale*, vol. 2, pp. 45–59, Dec. 2009.
- [96] A. Valota, D. LeClere, P. Skeldon, M. Curioni, T. Hashimoto, S. Berger, J. Kunze, P. Schmuki, and G. Thompson, "Influence of water content on nanotubular anodic titania formed in fluoride/glycerol electrolytes," *Electrochim. Acta*, vol. 54, pp. 4321–4327, Mar. 2009.
- [97] M. Qin, E. Kuo, K. Whittle, S. Middleburgh, M. Robinson, N. Marks, and G. Lumpkin, "Density and structural effects in the radiation tolerance of TiO<sub>2</sub> polymorphs," *Journal of Physics: Condensed Matter*, vol. 25, pp. 355402, Aug. 2013.
- [98] E. Shojaei, M. Abbasnejad, M. Saeedian, and M. Mohammadizadeh, "First-principles study of lattice dynamics of TiO<sub>2</sub> in Brookite and Cotunnite structures," *Physical Review B*, vol. 83, pp. 174302, May 2011.
- [99] E. Rogers, I. Stovall, L. Jones, R. Chabay, E. Kean, and S. Smith, (2000). Fundamentals of chemistry. [Online]. Available: <https://www.chem.wisc.edu/deptfiles/genchem/ssutorial/FunChem.htm>.
- [100] D. A. Jones, "Pitting and crevice corrosion," in *Principles and Prevention of Corrosion*, 2nd ed., B. Stenquist, R. Kernan and P. Daly, Eds. Prentice Hall, 1996, pp. 199–231.
- [101] D. A. Jones, "Galvanic and concentration cell corrosion," in *Principles and Prevention of Corrosion*, 2nd ed., B. Stenquist, R. Kernan and P. Daly, Eds. Upper Saddle River, NJ: Prentice Hall, 1996, pp. 170.

THIS PAGE INTENTIONALLY LEFT BLANK

## **INITIAL DISTRIBUTION LIST**

1. Defense Technical Information Center  
Ft. Belvoir, Virginia
2. Dudley Knox Library  
Naval Postgraduate School  
Monterey, California